Development of Nanoparticle Catalysts for Plasmonic Photoelectrochemical Reduction of Carbon Dioxide

By

Tatiana I. M. Morin Caamano

Thesis submitted to the University of Ottawa

in partial fulfillment of the requirements for the

degree of Master of Applied Science in Chemical Engineering

Department of Chemical and Biological Engineering

Faculty of Engineering

University of Ottawa

Dedicated to my beloved family and friends.
To my parents, Gabriela and Pierre, for pushing me and allowing me to reach for more.
To my grandparents, Enrique and Lourdes for driving me to school when I was younger, and to Jeanette, who taught me that hard work and kindness goes far.
To my partner, Kevin, for his endless support, love and for cooking me dinner after late nights at the lab.
To our cat Tenzin, for her much needed snuggles and for getting me up in the morning.
And to my sister, Paola and all my friends who supported me through laughs and listened to me talk about my lab work.

Table of Contents

List of Figures

List of Tables

Legend

ACN	Acetonitrile
ADN	Adiponitrile
BO	Bond order
CA	Chronoamperometry
CCUS	Carbon capture, utilization and storage
CO_2ER	CO_2 Electrochemical Reduction
Cu-M	Copper-metal
CV	Cyclic voltammetry
DFT	Density Functional Theory
DMF	Dimethylformamide
DOS	Density of State
ECSA	Electrochemical surface area
EELS	Electron energy loss spectroscopy
ER	Electrochemical reduction
FE	Faradaic Efficiency
FE	Field emission
FTIR	Fourier-transform infrared spectroscopy
FWHM	Full width at half maximum
GC	Gas chromatography
GDL	Gas diffusion layer
GGA	General gradient approximation
HER	Hydrogen evolution reaction
HPLC	High-performance liquid chromatography
IL	Ionic liquid
IPCC	Intergovernmental Panel on Climate Change
LSPR	Localized surface plasmon resonance
NAC	Net atomic charges
NP	Nanoparticle
PAW	Projector augmented wave
PBE	Perdew-Burke-Ernzerhof functional
PBS	Phosphate saline solution
PM-IRRAS	Polarization modulation infrared reflection absorption spectroscopy
SBN	Sebaconitrile
STP	Standard temperature and pressure

$TBAPF_6$	Tetrabutylammonium hexafluorophosphate
TEM	Transmission electron microscopy
UPD	Under potential deposition
VASP	Vienna Ab-initio Simulation Package
XPS	X-ray photoelectron spectroscopy
XRD	X-ray powder diffraction

Symbols

E	Full cell applied potential
E^o	Standard potential
D	Crystallite sizes
E^*	Thermodynamic minimum potential
$E_{1/2}$	Half wave potential
E_{ads}	Adsorption energy
E_{pa}	Anodic peak potential
E_{pc}	Cathodic peak potential
F	Faraday constant
η	Overpotential
i	Current
i_{ECSA}	Current normalized by ECSA
i_{geo}	Current normalized by geometrical surface area
j	Current density
n	Number of electrons
Q	Charge consumption
T	Temperature
T_{auto}	Auto ignition temperature
T_b	Boiling point temperature
T_f	Flash point temperature
T_m	Melting point temperature
y	weight percentage
ΔG	Gibbs free energy
ε	Dielectric constant
η	Dynamic viscosity

Abstract

The threat of the ongoing climate crisis requires the complete reduction of carbon emissions in the next two to three decades. Carbon dioxide electrochemical reduction (CO_2ER) poses a promising pathway to be able to maintain our current energy infrastructures in a carbon neutral fashion, by allowing the production of fuels and chemicals, such as CO, methanol and ethylene, with the use of carbon capture technologies and green energy. Thus far, Cu is the only metal that has demonstrated the ability to form hydrocarbon products. However, Cu is hindered by low selectivity. Improvements have been observed by coupling Cu with noble metals, such as Ag and Au. However, despite significant advancements, the technology has yet to achieve sufficient performance in activity, stability and selectivity for commercial viability. As such, this work pursued to further advance the activity of CO_2ER through the use of plasmonic Cu-based catalysts and the study of novel dinitrile-based electrolytes.

It has recently been identified that CO_2ER can benefit from direct plasmonic effects induced by light illumination. In essence, certain light wavelengths can induce collective oscillations of the free electrons in the metallic particles, leading to an enhancement of their electrocatalytic performance. As such, the first project of this work involved the development and testing of plasmonic Cu-Ag bimetallic catalysts for the application of CO_2ER. Cu, Ag, as well as Cu-Ag bimetallic particles with variable morphologies were able to be synthesized through a facile one-pot sodium borohydride chemical reduction method. The synthesized catalyst performance was also compared to commercial catalysts. The synthesized particles were found to be active catalysts for CO_2ER, with improved electro-catalytic activities exhibited by $Cu_{85}Ag_{15}$, $Cu_{60}Ag_{40}$ and Cu syntheses in respective order. All nanoparticles demonstrated increases in the catalytic activity ranging between 15-26% under white light illumination, attributed to plasmonic promotion. The

best plasmonic promotion of 26% was observed in the CuAg commercial alloy. Meanwhile, the best promotion of the synthesized bimetallic particles was of 18% found in the $Cu_{60}Ag_{40}$ catalyst. Additionally, improved electrochemical and plasmonic stability was observed with the use of the Cu-Ag bimetallic synthesized structures compared to monometallic Cu.

In addition, most studies pertaining CO_2ER involve aqueous electrolytes due to their low cost and low toxicity. However, these systems are hindered by mass transfer limitations due to the low solubility of CO_2 in water. Organic-based electrolytes have been subjects of research as they possess higher CO_2 solubilities to water. As dinitriles pose a novelty in the role of CO_2ER, dinitrile-based electrolytes were studied and tested for the application. It was hypothesized that due to the decreased polarity in dinitrile solvents, CO_2 concentrations in the electrolyte would increase leading to improved catalytic activity. The testing was conducted by evaluating and comparing acetonitrile (ACN), adiponitrile (ADN) and sebaconitrile (SBN) solvent-based electrolytes. Increased CO_2 solubility was observed in the dinitriles with 582 mM and 503 mM of dissolved CO_2 in ADN and SBN respectively, compared to 270 mM in ACN. Results were corroborated through DFT modelling, indicating preference of CO_2 absorbance to nitrile groups on the molecules. However, despite increases in CO_2 concentration, the electrochemical activity decreased from ACN > ADN > SBN. The trend in activity was observed to be inversely proportional to the viscosity of the dinitrile solvents, which affected the ionic conductivity.

Based on these developments, the present thesis opens a new perspective for the use of Cu-based nanoparticles for direct plasmonic enhancement with the use of a broad-range wavelength white light. Furthermore, the work also sheds light on the properties and resulting electrocatalytic activities of the use of dinitrile organic electrolytes for CO_2ER. The presented findings provide significant groundwork for further developments in the realm of CO_2ER.

Résumé

La crise climatique en cours représente une menace qui requiert la réduction totale des émissions de dioxyde de carbone dans les prochains vingt à trente ans. La réduction électrochimique du dioxyde de carbone (CO_2ER) ouvre une voie prometteuse pour maintenir nos infrastructures énergétiques actuelles d'une manière neutre en émissions de carbone. Ceci est réalisé par la production de carburants et produits chimiques, tel que le CO, le méthanol et l'éthylène, avec l'usage des technologies de captage du carbone et des sources d'énergie verte. À ce jour, le Cu est le seul métal qui a démontré la capacité de former des produits d'hydrocarbures. Cependant, le Cu est contraint par sa faible sélectivité. Des améliorations ont été démontrées par l'utilisation du Cu avec des métaux nobles comme l'Ag et l'Au. Toutefois, malgré ces progrès, la technologie n'a pas encore atteint la performance suffisante dans son activité, sa stabilité et sa sélectivité pour permettre sa viabilité commerciale. Ainsi, ce travail a été poursuivi pour avancer l'activité de la CO_2ER avec l'utilisation de catalyseurs plasmoniques à base de Cu et avec l'étude de nouveaux électrolytes à base de dinitriles.

Récemment, il a été identifié que la CO_2ER peut bénéficier des effets plasmoniques induit par illumination d'une lumière directement sur le matériau catalytique. En résumé, certaines longueurs d'ondes lumineuses peuvent causer des oscillations collectives des électrons libres dans les particules métalliques. Cela conduit à une amélioration de leur performance électro-catalytique. Ainsi, le premier projet était concentré sur le développement et les tests de catalyseurs plasmoniques bimétalliques faits de Cu-Ag pour l'application de la CO_2ER. Des particules de Cu, Ag et Cu-Ag avec morphologies variables ont été synthétisées à travers une méthode de réduction chimique facile utilisant du borohydrure de sodium. Les performances des matériaux synthétisés ont été comparées aux particules commerciales. Les particules synthétisées se sont révélées des

catalyseurs actifs pour la CO_2ER, grâce à des activités améliorées exposées par le $Cu_{85}Ag_{15}$, $Cu_{60}Ag_{40}$ et Cu synthétisés, dans cet ordre. Toutes les nanoparticules ont démontrées une augmentation des activités de 15-26% sous un éclairage de lumière blanche, attribuée à la promotion plasmonique. La meilleure augmentation de 26% a été observée par les particules commerciales d'alliage du CuAg. En même temps, une augmentation du 18% par les particules de $Cu_{60}Ag_{40}$ a été la meilleure promotion des particules bimétalliques synthétisées. Additionnellement, une amélioration de la stabilité électrochimique et plasmonique a été observée avec l'utilisation des structures bimétalliques du Cu-Ag par rapport au Cu seul.

De plus, la plupart des études de la CO_2ER impliquent des électrolytes aqueux en raison de leur coût et faible toxicité. Toutefois, ils sont entravés par des limitations du transfert de masse, en raison de la faible solubilité du CO_2 dans l'eau. Les électrolytes à base organique ont été sujets de recherche comme ils possèdent de hautes solubilités du CO_2 dans l'eau. Comme les dinitriles posent une nouveauté dans le rôle de la CO_2ER, des électrolytes à base de dinitriles ont été analysés et testés pour l'application. L'hypothèse émises était que les niveaux de CO_2 dans les électrolytes augmenteraient en raison d'une polarité réduite dans les solvants dinitriles. Ainsi, avec plus de CO_2 dans l'électrolyte, l'activité catalytique augmenterait. L'analyse a été faite en évaluant et en comparant des électrolytes à base d'acétonitrile (ACN), d'adiponitrile (ADN) et de sébaconitrile (SBN). Une augmentation de la solubilité du CO_2 dans les dinitriles a été observée avec 582 mM et 503 mM de CO_2 dissous dans l'ADN et le SBN respectivement, relativement à 270 mM dans l'ACN. Les résultats ont été corroborés par modélisation de la théorie fonctionnelle de la densité (DFT), qui a indiqué une préférence d'absorbance du CO_2 aux groupes nitriles sur les molécules. En dépit des augmentations de solubilité de CO_2, l'activité électrochimique a diminué à partir de

ACN > ADN > SBN. L’évolution de l’activité a été observé comme inversement proportionnel à la viscosité des solvants dinitriles, qui a affecté la conductivité ionique.

Sur la base de ces développements, la thèse présente ouvre une nouvelle perspective sur l’utilisation de nanoparticules à base de Cu pour l’amélioration du CO_2ER par effets plasmoniques directs avec l’illumination d’une lumière blanche à large spectre. De plus, ce travail éclaire aussi les propriétés et les activités électrochimiques résultantes de l’utilisation des électrolytes organiques à base de dinitriles pour la CO_2ER. Les constatations présentées offrent un travail préparatoire important pour des développements supplémentaires dans le domaine de la CO_2ER.

Statement of Contributions of Collaborators

I hereby declare that I am the first author of all chapters written in this thesis.

Chapters 1 and 4 were written solely by me, with editorial comments provided by Dr. Elena Baranova and Dr. Arnaud Weck.

Chapter 2 is a manuscript draft for publication in a peer-reviewed academic journal. Dr. Mohamed S. E. Houache (National Research Council Canada, NRC) provided the CuO commercial nanoparticle physicochemical characterizations. Dr. Martin Couillard (NRC) conducted the TEM characterizations of the other nanoparticles. Dr. Matthew Turnbull (NRC) conducted the XPS characterizations. The nanoparticle syntheses, all electrochemical measurements, and XRD characterizations were performed by me. Data analysis was performed by me with assistance of Dr. Elena A. Baranova, Dr. Arnaud Weck, and Dr. Abu-Lebdeh (NRC). The manuscript was solely written by me, with editorial comments provided by Dr. Elena Baranova and Dr. Arnaud Weck. All co-authors provided input and reviewed the manuscript.

Chapter 3 is a manuscript submitted for publication in a peer-reviewed academic journal. Dr. Mohamed S. E. Houache provided the CuO commercial nanoparticles physicochemical characterizations. Dr. Mario G. Sandoval conducted the DFT modelling and contributed the data analysis for that portion. Dr. Martin Couillard assisted with the TEM characterizations of the other nanoparticles. The evaluated electrolyte conductivity property measurements were conducted by me. FTIR measurements were conducted by me. All electrochemical measurements, as well as XRD measurements were also performed by me. Data analysis was performed by me with assistance of Dr. Mohamed S. E. Houache, Dr. Abu-Lebdeh Dr. Elena A. Baranova, and Dr. Arnaud Weck. The manuscript was solely written by me, with editorial comments provided by Dr. Elena Baranova and Dr. Abu-Lebdeh. All co-authors provided input and reviewed the manuscript.

Acknowledgements

I would like to thank my thesis supervisors, Dr. Elena Baranova and Dr. Arnaud Weck for providing me with the opportunity to pursue research in an amazing area of electrochemistry and physics. Their support and high expectations pushed me to learn and tackle challenges independently, as well as grow into a new role.

I would also like to thank Dr. Yaser Abu-Lebdeh for allowing me to explore a novel topic and opened his doors for me at the National Research Council of Canada (NRC).

I want to acknowledge Dr. Mohamed Houache for his indispensable assistance and advice when I needed them the most.

Also of acknowledgement are Dr. Pierre Berini and Dr. Zohreh Hirbodvash for providing me with important insights into plasmonics.

I also want to thank my colleagues, Emily, Frédéric, Najmeh and Ju for sharing their incredible knowledge with me and for their unconditional support.

I also would like to acknowledge the great students of the Chemical and Biological Engineering Graduate Student Association (CBEGSA) for fostering the student community through amazing events.

Also, I would like to thank the Chemical and Biological Engineering Department, as well as my committee members for their time and consideration of their review of my thesis.

Finally, thank you to the Materials for Clean Fuels Challenge Program at the National Research Council of Canada and the University of Ottawa for funding of the project.

Chapter 1. Introduction

1.1. Purpose of CO_2 Reutilization

Climate change, caused by anthropogenic carbon dioxide (CO_2) emissions, is currently the greatest growing threat to the environment and its ecosystems[1,2]. As human interactions are part of these systems, human habitat, resources, health, and security are also at risk[1,2]. The average global temperature has already reached an approximate 1.1 ^{o}C of warming since pre-industrial levels[3]. The resulting effects have already been observed and felt worldwide with unprecedented floods, droughts, weather patterns and melting ice sheets, to name a few[1,2]. The Intergovernmental Panel on Climate Change (IPCC) has reported that the world is on track to reach a 1.5 ^{o}C average warming above pre-industrial levels by 2035[1,2]. However, maintaining effects relatively close to the 1.5 ^{o}C figure requires carbon emissions to be completely reduced within the next 3 decades[3]. It has been identified that to achieve this while also maintaining current energy infrastructures, we will require the use of carbon capture, utilization and storage (CCUS) to be widely implemented[4].

The CO_2 electrochemical reduction (CO_2ER) reaction is a promising pathway to convert CO_2 into fuels and chemicals[5,6]. The process can be coupled with renewable energy sources and carbon capture technologies to become a net zero emission technology[6]. As a result, it has become a promising candidate for development in the rising green economy. However, despite significant advancements in research of the technology in the past 20 years, the production of multicarbon hydrocarbon products (C_{2+}) still exhibits performance challenges in selectivity, stability as well as activity[5].

1.2. Fundamentals of CO_2 Electrochemical Reduction

Typical catalytic conversions utilize heat (thermal energy) to facilitate reactions. In electrochemical reactions, the source of energy is that of electrical energy, where two half-cell redox reactions are driven to complete the electrical circuit. In a CO_2ER aqueous electrolytic cell, the two reactions involve that of CO_2 reduction at the cathode, as well as the water oxidation reaction occurring at the anode. At the anode, the water oxidation reaction occurs by pulling electrons from the water molecules provided by the aqueous electrolyte, generating H^+ ions and oxygen (O_2) as a result. The electrons are then driven through the electrical circuit, while the ions are transported through the conductive electrolyte. These components are then delivered to the cathode, where the reduction reaction takes place, and utilize the electrons and the H^+ ions to drive the reduction of CO_2. A schematic of a CO_2ER aqueous electrochemical cell is shown in Figure 1.1.

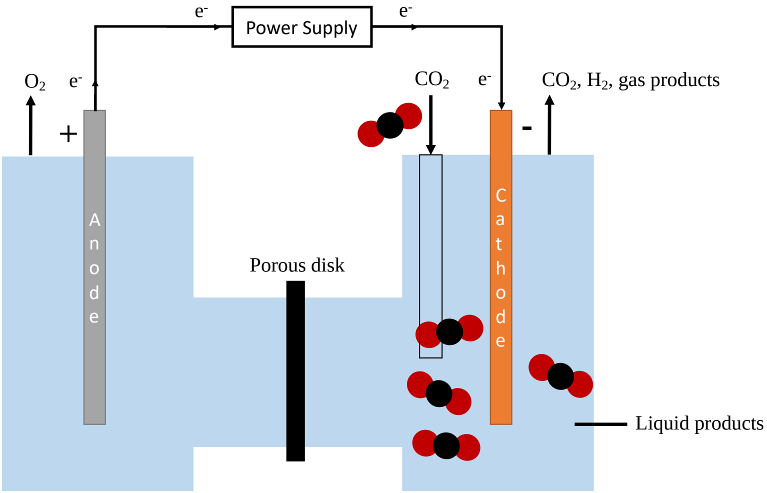

Figure 1.1: Schematic of a CO_2 electrochemical reduction H-cell.

At the anode, the catalyst typically consists of platinum (Pt) to drive the water oxidation reaction. For cathodic catalytic materials, transition metals have been under study to understand the products that can potentially be generated. From the studied catalysts, several cathodic reactions have been documented, as outlined in Table 1.1. It can be observed from the reactions that attractive high value and high demand products such as ethylene, ethanol and n-propanol can be generated. However, the issue has been engineering highly selective catalysts which produce elevated product rates with sufficiently low energy and long enough periods of time for the technology to be economically and commercially viable.

Table 1.1: Anodic and cathodic half-cell reactions in aqueous electrolyte for CO₂ER.

Anodic Reaction	**E^0 vs NHE (V)**
$2H_2O \rightarrow O_2 + 4H^+ + 4e^-$	+ 0.81
Cathodic Reactions	**E^0 vs NHE (V)**
$CO_2 + 2H^+ + 2e^- \rightarrow HCOOH$	-0.61
$CO_2 + 2H^+ + 2e^- \rightarrow CO + H_2O$	-0.53
$2CO_2 + 2H^+ + 2e^- \rightarrow H_2C_2O_4$	-0.913
$2CO_2 + 2e^- \rightarrow C_2O_4{}^{2-}$	-1.003
$CO_2 + 4H^+ + 4e^- \rightarrow HCHO + H_2O$	-0.48
$CO_2 + 6H^+ + 6e^- \rightarrow CH_3OH + H_2O$	-0.38
$CO_2 + 8H^+ + 8e^- \rightarrow CH_4OH + 2H_2O$	-0.24
$2CO_2 + 12H^+ + 12e^- \rightarrow C_2H_4 + 4H_2O$	-0.349
$2CO_2 + 12H^+ + 12e^- \rightarrow C_2H_5OH + 3H_2O$	-0.329
$2CO_2 + 14H^+ + 14e^- \rightarrow C_2H_6 + 4H_2O$	-0.27
$3CO_2 + 18H^+ + 18e^- \rightarrow C_3H_7OH + 5H_2O$	-0.31
$2H^+ + 2e^- \rightarrow H_2$	-0.42

Along with the reactions in Table 1.1, the standard potentials (E^o) of the half-cell reactions in both the anode and cathode are also reported. These indicate the potentials required to undergo the reaction at standard temperature and pressure (STP) conditions, as well as 1 M concentrations. The half-cell potentials cannot be directly measured, instead the cell potential (E^o_{cell}) is measured. The cell potential equates to the difference between the cathodic half-cell potential (E^o_c) and the anodic half-cell potential (E^o_a), shown in Equation 1-1.

$$E^o_{cell} = E^o_c - E^o_a \qquad \text{Equation 1-1}$$

Notably, the actual required potential of the cell to achieve the electrochemical reactions is typically greater than that of the minimum potential required due to resistances. This difference can be defined as the overpotential (η), shown in Equation 1-2, through which the efficiency of the cell can be evaluated.

$$\eta = E - E_{cell}^{o} \qquad \text{Equation 1-2}$$

Another important component for the evaluation of electrochemical systems is that of the current (i), defined by Faraday's law

$$i = nF\frac{dN}{dt} \qquad \text{Equation 1-3}$$

which relates to the rate of the movement of electrons at the interface. As this is correlated to the reaction rate at the interface, the current indicates the activity of the reaction. This value is typically normalized per the electrode area to define the current density measurement (j). Two types of areas can be utilized that of the geometrical area or by evaluating the active electrochemical surface area (ECSA) of the catalyst. Of the two, the latter is typically utilized for nanoparticle catalysts, as the active surface area is increased by the overall roughness of catalytic area. In terms of product selectivity, the Faradaic efficiency (FE) is a factor that quantifies the efficiency of the electron transfer to a given electrochemical reaction. The FE is calculated by,

$$FE = \frac{nFm}{j} \qquad \text{Equation 1-4}$$

where n is the number of electrons transferred in the reaction, F is the Faraday constant, m is the molar production rate, and j is the total current density.

1.3. Current State of Cu-Based Electrocatalysis for CO_2ER

The established groundwork of CO_2ER has been attributed to the work of Hori *et al.*[7–10] in the mid to late 1980's. Their earliest work was the first to evaluate the overall product distribution of different metallic catalysts for the reduction of CO_2, identifying Cu as a unique catalyst for the formation of hydrocarbon products. Later works, went on to further study the effects of electrolyte anions and cell potential on the overall hydrocarbon product distributions on Cu electrodes. Overall, earlier works in the area focused on metallic plates or sheets. However, focus has shifted towards nanostructured catalysts, as they provide better activity due to a higher relative surface area and also provide the ability to tune their morphology[11].

Transition metals have been widely studied as electrochemical catalysts for CO_2ER[12]. The main products that have been able to be observed have been those of carbon monoxide (CO), formate, hydrocarbons and alcohols, as well as hydrogen due to the hydrogen evolution reaction (HER) depending on the catalyst material[12]. Copper (Cu) has been of particular focus in research as it is the only known catalyst with the ability to produce C_{2+} products. However, Cu is mainly hindered by poor selectivity and stability[6]. Insights into improvements of the material selectivity have found that single crystal facets form preferential products. Cu (111) has shown improved selectivity towards methane, while those of Cu (100) and Cu (200) have shown preferential formation of ethylene[12,13]. Improved performance has also generally been observed through the use of Cu-oxides[11]. However, the topic is debated for whether the effects are due to the increased roughness of the oxidized nanostructure or due to the role of oxygen in the reaction[11].

It has also been identified that the preferential selectivity of products can be attributed to the binding strength of intermediates on the metal[6]. Generally, metallic catalysts have been categorized into four main groups depending on their most selective products[11,12]. Those that are selective towards CO are Zn, Ga, Pd, Ag and Au. Those that are selective towards formate include In, Sn, Hg and Pb. Then there are those that are selective towards the competing HER reaction, which are Ti, Fe, Ni and Pt. Prominently Cu does not fit into these conventional groups and stands alone, as it uniquely is able to form hydrocarbon and alcohol products. It has been determined that the selectivity preferences of the metals are able to be related to their H- and O-binding abilities of the intermediates[6]. Cu has been identified to possess moderate affinities to both components[6], thus allowing sufficient stabilization of the *CO intermediate to allow C-C coupling or protonation for the formation of *OCCO or the protonation into *COH or *CHO, leading to its unique products. Meanwhile, hydrogen selective metals possess stronger H-binding abilities relative to Cu[6]. Formate selective metals, tend to have weaker H-binding abilities but stronger O affinities thus stabilizing the *CO intermediate more strongly than Cu and proceeding to form the *COOH or *OCHO intermediates[6]. Finally, CO selective metals also demonstrate weaker H affinity, but also weaker O-binding, leading to the formation of the *CO intermediate but due to its weak stability on the surface it is released before it can react to form other intermediates[6].

1.3.1 Cu-M bimetallic catalysis

Ongoing efforts to improve the selectivity of Cu have led to the use of Cu-metal (Cu-M) bimetallic catalysts, where coupling the metal with other materials of different intermediate binding strengths has shown to improve the selectivity[11,14]. Use of bimetallic particles has also shown to enhance the stability and the activity of the catalysts[11]. Both alloys and bifunctional composites have been found to have their own advantages.

M = H_2 Selective Metals

Coupling of Cu with H_2 selective metals, has generally shown that increased C_{2+} product selectivity cannot be achieved in these systems[11]. Increasing M loading in this type of Cu-M relationships usually decreases C_{2+} products[11]. This effect has been attributed to hindering of C-C coupling of *CO due to increased H_2 adsorbed at the surface and/or due to the lack of neighbouring Cu, reducing the chances of *CO interactions for the dimerization to occur[11]. Increases in CO selectivity has been observed to occur in Cu-Pd systems[6,11]. This has been attributed to weakening of *CO adsorption due to the electronic effects of Cu-Pb[6]. In the notable work of Ma *et al.*[15] the effects of ordered and disordered alloying, as well as bi-phase Cu-Pd nanoparticles for CO_2ER, resulted in findings of the ordered alloy displaying CO selectivity (>80% FE). Notably, a C_2H_4 selectivity (FE >60%) was also observed in the bi-phase Cu-Pd systems. These effects have been attributed to the neighbouring Cu sites allowed to undergo C-C coupling, while the absorbed hydrogen in the Pd may have allowed hydrogeneration of the *CO intermediates[6].

M = Formate Selective Metals

The integration of Cu with formate selective metals has observed CO production along with HER suppression, or enhancement of formate selectivity[11]. However, suppression of C_{2+} product formation has generally been the case[6,11]. In allowing for CO synergistic effects, it has been found that surface interfaces of Cu-M of this type are required[11]. The surface interfaces were found to facilitate *COOH formation, which play the role in the production of CO through the intermediate, as well as the allowance of *OCHO intermediate which exhibits strong binding, leading to the suppression of adsorbed H[6,11]. In several Cu-Sn and Cu-In systems FE >90% for the production of CO have been able to be achieved[6,11].

M = CO Selective Metals

The combination of Cu with CO selective metals, such as Ag, Au, Zn, has not only shown enhancement of CO selectivity and activity of the reaction, but also has displayed enhancement of C_{2+} products in certain cases[6,11,16]. In terms of CO selectivity, increasing the secondary metal loading shows increased CO production, which is expected[11]. However, it has been found that optimal Cu-M compositions of this type show improved CO production to the pure CO selective metals. This has shown that synergetic effects are likely at play[11]. These suspected effects could be due to adsorbed *CO on Cu surfaces repulsing adsorbed *CO on the neighbouring metals due to dipole interactions, enhancing CO production in this way[11]. Another theory is attributed to the formation of *COOH intermediates on the Cu, which the neighbouring metal utilizes for the formation of CO[11]. Meanwhile, the synergistic effects for enhancing C_{2+} products has been mainly associated to CO spillover[11]. This is explained by the weaker binding of *CO on the secondary metals providing additional CO to be supplied to the neighbouring Cu, thus allowing increased coverage of *CO and in turn enhance C-C coupling occurrences[11]. The work of Wang *et al.*[17] tested Ag/Cu bimetallic nanoparticles, where smaller Ag particles decorated larger Cu particles, the 6% Ag loading catalyst resulted in a FE of ethylene of 42% at a -1.1 V vs RHE potential with a 30 h stability. This was compared to the ethylene FE of Ag, Cu and AgCu alloy, which were of 0, 19.5 and 26.8% respectively[17]. Chang *et al.*[18] tested tunable Ag@Cu core-shell nanoparticles by influencing the Cu shell formation via the synthesis heating time. Their results observed optimal CO production (FE 82%) in Ag@Cu with 7 minutes of heating time, and optimal ethylene (FE 28.6%) with 20 minutes of heating time both at -1.06 V vs RHE[18]. In terms of alcohol production, Morales-Guio *et al.*[19] evaluated a bi-phase Au/Cu system of gold nanoparticles deposited on a copper foil, where the catalyst was determined to be more selective towards alcohol products over methanol by a factor of 100 and alcohol production was observed at potentials 265 mV more positive to monometallic Cu. For Cu-Ag systems, in the works of Lv *et al.*[20], as well as Zhang *et al.*[21] their results have yielded alcohol productions reaching FE >63%.

Despite significant advancements in development, tuning, and understanding of different bimetallic systems and mechanisms in CO_2ER, sufficiently high enough efficiencies of C_{2+} products has still not been achieved. However, the path of Cu-M with CO selective metals has shown the most promise for the development of improved catalytic promotion of increased value products. Of these, Cu-Ag and Cu-Au systems have shown significant advancements. As economics are a large part of commercial viability, Cu-Ag systems were selected to developed and studied in Chapter 2 of this work. In order to further increase the activity of the system, plasmonic effects were also exploited to further advance the performance of the system.

1.4. Plasmonic Enhanced CO_2ER

The combination of photochemical and electrochemical effects has been explored to exploit light energy to further advance the CO_2ER reaction[22–24]. Traditionally, this has been done by coupling electrocatalysts with semiconductors[23]. The former conducting the reaction, while the latter allow the harvesting of light energy and transforms it to induce charge carriers, which can then be transferred to the metallic catalyst to further advance the reaction[25].

More recently, it has been identified that metals which exhibit localized surface plasmon resonance (LSPR) in their nanostructures can instead directly harvest and convert light energy. This is done through light irradiation using wavelengths with similar frequencies to that of the nanoparticle electron cloud, which result in the collective oscillation of the electrons of the particles[26]. This then allows the formation of enhanced electromagnetic fields, the generation of hot-charge carriers, and/or photothermal effects which can help to further drive catalytic reactions[25–27]. Au, Ag and Cu have particularly been regarded as promising plasmonic catalysts as they possess strong LSPR effects in the visible region of light[25]. Of these, Au and Ag are the most popular due to their higher stability compared to Cu, as it is easily oxidized[25].

1.4.1. Fundamentals of Plasmonic Catalysis

The shiny look of metals is due to vibration of valence electrons when illumined with light energy. These vibrations lead to the incident light being reflected, giving metals this physical property. This effect is essentially what leads to the LSPR effect, where metallic particles that are smaller than the wavelength of incident light experience a collective oscillation of their electrons at the frequency of the light[28], as depicted by Figure 1.2a. Wavelengths of light in the UV and visible range between 10-750 nm, and thus metallic nanoparticles have shown to possess plasmonic properties in this range of light[28]. The LSPR peak inducing wavelength depends on the size and morphology of the nanoparticles[28,29]. This is because the morphology and size provide physical limits or extensions to the way that the electrons are able to resonate[29]. Size typically dictates the wavelength which excites the plasmonic response, where a larger particle typically leads to a greater LSPR wavelength required for the particle to match its frequency[29]. Morphology also has evidence of this type of effect where ellipsoids generally lead to greater LSPR wavelengths due to their larger length size, but in some cases two resonant peaks are observed, where the other seems to be indicative of a smaller size that of their smaller width with smaller LSPR wavelengths[29]. Notably, the material is also important for plasmonic effects. Metals with the strongest LSPR responses are those of Cu, Ag and Au, due to the same reason as to why they are good conductors, that of their increased free mobility of electrons in the metal[28]. As a result, their nanoparticle electron clouds move more freely, providing an enhanced plasmonic response to other metals.

In the realm of catalysis, performance enhancement induced by plasmonic effects are mainly due to LSPR decay mechanisms. As plasmonic effects are excited states, the added induced energy requires to be transferred in order for the particles to return to an unexcited state. As mentioned previously, the three main effects that occur from induced LSPR response, result in enhancement of electromagnetic fields, generation of hot-carriers, and/or photothermal effects[25–27]. The enhanced electromagnetic effects are attributed directly from the collective oscillation of electrons, thus providing an enhanced electric field[25,29]. The resulting electric field can be utilized to advance the activity of neighbouring photocatalysts, such as semiconductors[27]. Meanwhile, the latter two effects are due to LSPR decay mechanisms, which can lead to the direct enhanced performance of catalytic reactions on the metal[28,29]. Hot carriers are defined as hot holes or electrons, which are driven by high kinetic energies due to strong electric fields. Due to the enhancement of electric fields during LSPR, it is theorized that hot carriers are formed in this state, as depicted by Figure 1.2b and thus can either be transferred or injected into an adjacent source, such as directly into an adsorbed intermediate, a semiconductor, or into a non-plasmonic metal[28,29]. In cases where hot electrons are not transferred, the carriers then decay into a thermalized state, leading to thermal energy being dissipated into the environment[29,30]. This latter mechanism is what is attributed to photothermal effects, as seen in Figure 1.2c.

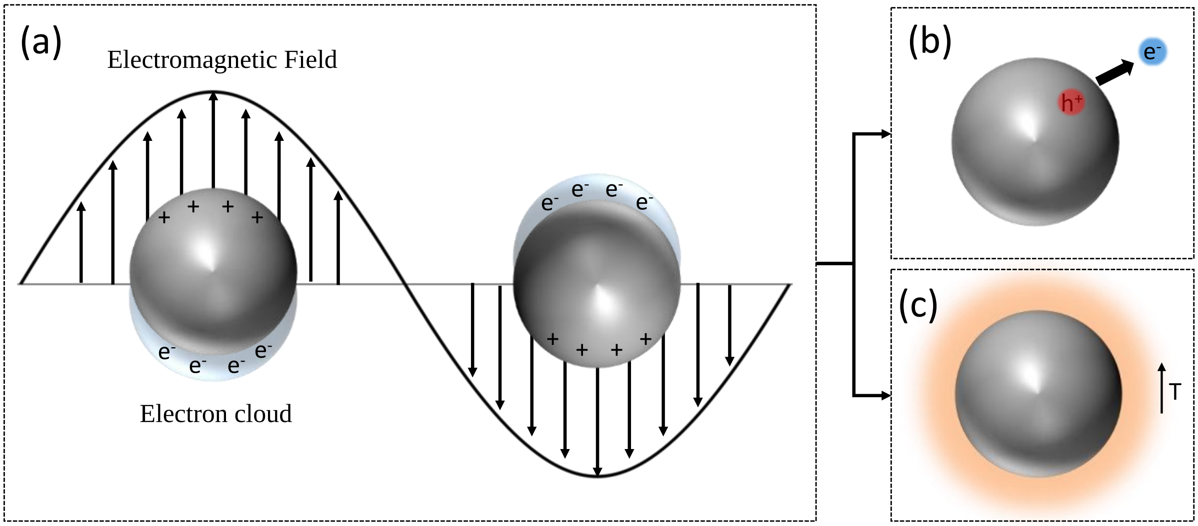

Figure 1.2: Diagrams depicting (a) the LSPR effect on a nanoparticle, (b) the generation of hot carriers in the nanoparticle, and (c) generation of photothermal effects leading to the increase of local temperature on the nanoparticle.

1.4.2. Plasmonic Effects in Electrocatalysis and CO_2ER

Due to the capacity that LSPR possess to generate hot carriers and to increase the local temperature through photothermal effects, the promise of coupling metallic electrocatalysis with plasmonic effects has been identified[31,32]. Through the combined use of plasmonic electrocatalysis, the catalytic activity can be increased by achieving higher current densities and can also reduce the energy requirement through lowering the required onset potential or overpotential[31]. Additionally, product selectivity has also been shown to be influenced by plasmonic enhancement[31,32], which is theorized to be an effect of direct hot carrier injection into the adsorbed intermediates. Overall, efforts have been made in the development of plasmonic-induced electrocatalysis in direct and indirect forms. The former consisting of pure plasmonic metallic nanoparticles, while the latter involving plasmonic nanoparticles embedded in or in combination with semiconductors or non-plasmonic metallic catalysts[31]. These approaches have been utilized to further advance different electrocatalytic reactions such as glycerol oxidation, water splitting, CO_2ER, among others. In the work of Rasmussen *et al.*[33], direct plasmonic enhancement of glycerol oxidation was observed on an unsupported Ag-Au porous catalyst structure. Their results yielded an 100% increase in current and power outputs with a 400-425 nm light wavelength, where the LSPR peak was observed[33]. For water splitting, advancements have focused on integrated semiconductor-metal catalysts for plasmonic photo-electrochemical reduction[34,35]. Overall, research in the area has moved towards fabrication of ordered nanostructured semiconductor structures decorated with plasmonic metallic nanoparticles[34,35]. These architectures have shown to enhance the light absorption capabilities of the semiconductors[34,35]. Elegant structures have been fabricated by groups like Wu *et al.*[36] who fabricated ZnO rods coated with Au at the tip to form match-like structures, reporting an energy-to-hydrogen conversion efficiency 16 times higher than an undecorated ZnO nanorod array. Notably, the area of direct plasmonic assisted electrochemical reactions is still relatively untapped, and thus there is an opportunity to further explore this area to further advance these reactions.

CO_2ER has also been identified as a candidate to benefit from plasmonic catalysis[25,37,38]. This is due to its use of the metal catalysts that exhibit LSPR effects. Previous work in plasmonic CO_2ER has focused on noble metals and the use of lasers of particular light wavelengths to induce the plasmonic response. In the work of Creel *et al.*[39] observations of product selectivity changes were observed with the induced plasmonic response in a Ag thin film catalyst under different potentials. Notably, methanol production was observed at more negative potentials only under light irradiation, a product that was not detected prior on Ag[39]. Additionally, HER suppression was evident under the evaluated potential range with light exposure[39]. Other work in the area has focused on coupling plasmonic catalysts with non-plasmonic metals or semiconductors to advance the CO_2ER through a plasmonic photoelectrochemical approach, rather than direct excitation of the reaction catalyst[40]. Despite the lack of work on plasmonic Cu catalysis, significant groundwork has been now laid out by an extensive review of the topic by Xin *et al.*[25] outlining the most recent advancements. The work notes the lack of work on plasmonic Cu nanoparticles without the use of semiconductors for the application of CO_2ER[25]. Thus, to further advance the continuing work in this area, exploration into Cu and Cu-based catalysts without the use of semiconductors is required. Additionally, the use of broad ranges of light sources have also not been studied for the generation of LSPR, which would assimilate better conditions expected to that of solar light utilization.

1.5. Electrolyte Advancements in CO_2ER

The role of electrolytes have been studied for the application of CO_2ER, including aqueous, organic and ionic liquids[41,42]. Of these, aqueous electrolytes containing inorganic salts have been the most widely used for CO_2ER due to their low cost, low toxicity, and high abundance. However, water possesses low CO_2 solubility of only approximately 34 mM at standard temperature and pressure (STP) conditions[41]. The low exhibited availability of the reagent in the solution leads to mass transfer limitations. As a result, alternative electrolytes have also been explored to overcome this limitation.

1.5.1. Aqueous

In aqueous-based electrolytes, studies into the role of pH, salt concentration, cations, and anions has been conducted to understand their influence in the electrochemical performance of the reaction[41,42]. These parameters have shown to play a role in the selectivity, as well as activity of the reaction. In terms of pH, effects on product selectivity for the CO_2ER on copper electrodes has been observed. It was demonstrated by Hori *et al.*[43] that CH_4 evolution is proton dependent, while ethylene evolution is proton independent. This has been attributed to the formation pathways of the two products[44]. This result has indicated that the selectivity can be shifted towards ethylene in basic solutions, as CH_4 evolution is suppressed with lower proton concentrations[41,45] . Although the effects of pH on the reaction is known, this parameter is harder to control at a local level.

To improve local pH levels, the electrolytic buffer effect has been studied. Increasing electrolyte concentrations does not only decrease conductivity resistances for the reaction but are also known to increase the electrolytic buffer. This latter effect has been shown to have an impact on the local pH at the cathode surface, as it impacts the degree at which the electrolyte is able to supress pH changes at this level. It has been demonstrated that with lower electrolyte concentrations, the local pH increases, and as a result CH_4 and H_2 reactions are suppressed, while ethylene is promoted[41,45].

In terms of the cation it is known that by increasing the cation size, the activity increases as a result of the increased adsorption on the electrode[41,46]. For the application of CO_2ER, an influence on the selectivity has also been observed[41]. Some of these effects have been attributed to tendencies towards intermediate stabilizations on smaller cations[41]. In a study by Singh *et al.*[46] it was found that increases in the cation size, decrease the pK_a of the hydrated cation. This effect in turn decreases local pH[46]. As pH also plays a role in CO_2 solubility, the increase in selectivity towards CO_2 reduction products was explained by an increase in the local CO_2 concentration[46].

Finally, the role of anions has also been explored. Overall, the use of bicarbonate anions is the most popular because of its role as a buffering agent, which leads to increases in the local CO_2 concentrations via the local pH[42,46]. Another largely reported electrolyte is the phosphate buffered saline solution (PBS), which has generally shown increased selectivity to H_2 and CH_4 products. This selectivity has been attributed to phosphate anions having the ability to serve as proton donors[41]. The role of supporting anions has also been studied mainly in the form of halide anions[41,42]. It has been generally observed that the adsorbed anions help to stabilize the *CO intermediate, favoring CO and C_{2+} products[42]. Additionally, due to the adsorbance of the anions, morphology changes of the catalysts have also been reported[42,46].

1.5.2. Ionic Liquids

Ionic liquids (ILs) can be used as electrolytes without the use of water, as they are able to conduct electricity. ILs also possess the advantage of high CO_2 absorption[47], even being studied as potential solvents for CO_2 capture[48]. These types of electrolytes also reduce the energy of formation of the $\mathrm{CO_2}^{-\cdot}$ anion radical by stabilizing it, thus lowering the energy required to undergo CO_2ER[41,47]. In absence of water, no protons (H^+) are available to undergo the reactions in Table 1.1. Therefore, the reaction pathway mainly follows that of the $\mathrm{CO_2}^{-\cdot}$ anion radical, shown in Equation 1-5. From the $\mathrm{CO_2}^{-\cdot}$ anion radical, oxalic acid can be formed from the dimerization of two of the radicals [41,42]. Alternatively, $\mathrm{CO_2}^{-\cdot}$ and CO_2 can undergo disproportion to form CO and CO_3^{2-} [41,42]. A third reaction in the presence of water also can occur, via the protonation of $\mathrm{CO_2}^{-\cdot}$

to form formate[41]. However, in addition to the product formations of CO and formate, it has been documented that further reduction of these products with water can form glyoxylic acid, glycolic acid and tartaric acid[42].

$$CO_2 + e^- \rightarrow CO_2^{-\cdot} \qquad \text{Equation 1-5}$$

In terms of product selectivity, high CO selective systems were obtained in IL systems with water utilizing Ag or Au as catalyst[41,47]. In the work of Zhou *et al.*[49] FE >99% CO selectivity was achieved using a BMImCl electrolyte with 20 wt% H_2O on a silver electrode. High selectivity of formic acid (FE 87%) has also been observed on copper utilizing a [EMIm]BF_6 and water mixture with 8% v/v of water[50]. However, despite the advantages of IL, the selectivity towards C_{2+} products has not been able to be demonstrated significantly with the use of these electrolytes alone.

1.5.3. Organic Electrolytes

Aprotic organic electrolytes, such as methanol, acetonitrile (ACN) and dimethylformamide (DMF), have been previously evaluated for CO_2ER as they possess higher CO_2 solubility to aqueous solutions[41,42]. These electrolytes also have the added ability to suppress the competing HER due to lack of available protons. As a result of the lack of H^+ protons, the CO_2 electrochemical reduction follows the pathway of the formation of the $CO_2^{-\cdot}$ anion radical, shown in Equation 1-5. Notably, the reaction possesses a standard half-cell potential of -1.85 V vs NHE, thus requiring greater applied potentials than those in aqueous electrolyte conditions seen in Table 1.1.

Particularly focusing on nitrile solvents, acetonitrile has been the only previously studied aprotic organic solvent for CO_2ER electrolytes. The CO_2 solubility in ACN is approximately eight times higher than in water[41]. It has also been widely used in electrochemistry due to its high dielectric constant, wide potential window and its stability[51]. In the work of Figueiredo *et al.*[51]

ACN solvent electrolytes with different supporting electrolyte salts and small water contents for catalyzed CO_2ER were studied. Using Cu, Ag, Pt, Pd and Au it was largely observed that the main products of bicarbonates, carbonates and CO were influenced by the small presence of water, as they were formed at potentials corresponding to those of water oxidation, or reaction mechanisms accounting protons[51]. Lead (Pb) was the only material on which oxalate formation was observed[51]. Also utilizing Cu as a catalyst, Díaz-Duque *et al.*[52] studied water and acetonitrile mixtures. Their work found that the presence of water demonstrated a significant increase in the activity, finding optimal current densities with a 0.25 mole fraction of water. Notably, work in organic electrolytes utilizing Cu as a catalyst has been scarce[51]. More studies under dry solvent conditions are also required to further evaluate the performance of CO_2ER under this type of environment. Further insights into alternative organic solvents to those aforementioned are also lacking. Liquid dinitrile solvents, such as adiponitrile, have a higher boiling and flash point to acetonitrile and have been presented as a promising route of solvent to further evaluate electrochemical reactions[53].

1.6. Objectives and Structure

The objective of the work herein involves the development of efficient plasmon-assisted electrocatalytic systems for CO_2ER for the production of value-added products. As few studies have been conducted into the integration of plasmonic CO_2ER using Cu-based nanocatalysts, this work attempts to shed light into the plasmonic responses on catalytic activity and stability of Cu-based materials. The use of a white light system was utilized to achieve this to bring insights into the utilization of broad-range light systems for initiating plasmonic responses in catalysis, bringing the research closer to the use of solar light. In addition, exploration into alternative organic dinitrile solvent based electrolytes was conducted on the effect of CO_2ER performance. These objectives were explored through:

i. The development of Cu, Ag and Cu-Ag bimetallic nanoparticle catalysts through a simple wet electrochemical reduction synthesis for the application of plasmonic CO_2ER.

ii. Using the synthesized catalysts developed in (i), characterize, and utilize photo-electrochemical testing techniques to further understand the result of the syntheses process as well as evaluate the reaction performance on activity, stability, and plasmonic response of the catalysts.

iii. Evaluate the properties of dinitrile-based electrolytes involving salt solubility, conductivity, and CO_2 solubility.

iv. Using the electrolytes in (iii), evaluate the effects on electrochemical performance of Cu-based catalysts.

In Chapter 2, the development of Cu, Ag and Cu-based bimetallic nanoparticle catalysts through a one-pot sodium borohydride chemical reduction is explored. The effect on metal loading variations in the Cu-Ag bimetallic nanoparticles on the CO_2ER activity, plasmonic response and stability are evaluated through cyclic voltammetry (CV) and light off/light on chronoamperometry (CA) testing. Chapter 3 explores the study of the electrolyte properties including acetonitrile (ACN), adiponitrile (ADN) and sebaconitrile (SBN) solvent electrolytes with the use of tetrabutylammonium hexafluorophosphate ($TBAPF_6$) salt. The effect of solvent type on the conductivity is evaluated with different salt concentrations, and at different temperatures. Additionally, the CO_2 solubility was explored through a quantified FTIR methodology. The effect on CO_2ER activity is explored through CV and CA tests. Finally, Chapter 4 outlines the conclusions along with recommendations for future pathways to explore in the topic.

References

[1] IPCC, "Climate change: a threat to human wellbeing and health of the planet. Taking action now can secure our future.," **2022**, accessed on August 2, 2022, https://www.ipcc.ch/2022/02/28/pr-wgii-ar6/.

[2] IPCC, Climate Change 2022: Impacts, Adaptation, and Vulnerability. Contribution of Working Group II to the Sixth Assessment Report of the Intergovernmental Panel on Climate Change, **2022**.

[3] J. Marotzke, S. Milinski, C. D. Jones, *Weather* **2022**, *77*, 147.

[4] IEA, About CCUS, Paris **2021**, https://www.iea.org/reports/about-ccus.

[5] A. Somoza-Tornos, O. J. Guerra, A. M. Crow, W. A. Smith, B. M. Hodge, *iScience* **2021**, *24*, 102813.

[6] A. Vasileff, C. Xu, Y. Jiao, Y. Zheng, S. Z. Qiao, *Chem* **2018**, *4*, 1809.

[7] Y. Hori, A. Murata, R. Takahashi, *J. Chem. Soc. Faraday Trans. 1 Phys. Chem. Condens. Phases* **1989**, *85*, 2309.

[8] Y. Hori, K. Kikuchi, S. Suzuki, *Chem. Lett.* **1985**, *14*, 1695.

[9] Y. Hori, K. Kikuchi, A. Murata, S. Suzuki, *Chem. Lett.* **1986**, *15*, 897.

[10] Y. Hori, A. Murata, R. Takahashi, S. Suzuki, *J. Chem. Soc. Chem. Commun.* **1988**, 17.

[11] S. Nitopi, E. Bertheussen, S. B. Scott, X. Liu, A. K. Engstfeld, S. Horch, B. Seger, I. E. L. Stephens, K. Chan, C. Hahn, J. K. Nørskov, T. F. Jaramillo, I. Chorkendorff, *Chem. Rev.* **2019**, *119*, 7610.

[12] M. K. Birhanu, M. C. Tsai, A. W. Kahsay, C. T. Chen, T. S. Zeleke, K. B. Ibrahim, C. J. Huang, W. N. Su, B. J. Hwang, *Adv. Mater. Interfaces* **2018**, *5*, 1.

[13] C. Zhu, Z. Zhang, L. Zhong, C. S. Hsu, X. Xu, Y. Li, S. Zhao, S. Chen, J. Yu, S. Chen, M.

Wu, P. Gao, S. Li, H. M. Chen, K. Liu, L. Zhang, *Chem* **2021**, *7*, 406.

[14] J. Zhao, S. Xue, J. Barber, Y. Zhou, J. Meng, X. Ke, *J. Mater. Chem. A* **2020**, *8*, 4700.

[15] S. Ma, M. Sadakiyo, M. Heim, R. Luo, R. T. Haasch, J. I. Gold, M. Yamauchi, P. J. A. Kenis, *J. Am. Chem. Soc.* **2017**, *139*, 47.

[16] X. Li, J. Masa, Z. Sun, "Recent Advances in Electrode Materials for Electrochemical CO2Reduction," *ACS Symposium Series*, American Chemical Society **2020**, Vol. 1364, p. 49.

[17] J. Wang, Z. Li, C. Dong, Y. Feng, J. Yang, H. Liu, X. Du, *ACS Appl. Mater. Interfaces* **2019**, *11*, 2763.

[18] Z. Chang, S. Huo, W. Zhang, J. Fang, H. Wang, *J. Phys. Chem. C* **2017**, *121*, 11368.

[19] C. G. Morales-Guio, E. R. Cave, S. A. Nitopi, J. T. Feaster, L. Wang, K. P. Kuhl, A. Jackson, N. C. Johnson, D. N. Abram, T. Hatsukade, C. Hahn, T. F. Jaramillo, *Nat. Catal.* **2018**, *1*, 764.

[20] X. Lv, L. Shang, S. Zhou, S. Li, Y. Wang, Z. Wang, T. K. Sham, C. Peng, G. Zheng, *Adv. Energy Mater.* **2020**, *10*, 1.

[21] S. Zhang, S. Zhao, D. Qu, X. Liu, Y. Wu, Y. Chen, W. Huang, *Small* **2021**, *17*, 1.

[22] X. Chang, T. Wang, P. Yang, G. Zhang, J. Gong, *Adv. Mater.* **2019**, *31*, 1.

[23] N. Zhang, R. Long, C. Gao, Y. Xiong, *Sci. China Mater.* **2018**, *61*, 771.

[24] D. Li, K. Yang, J. Lian, J. Yan, S. Liu, *Adv. Energy Mater.* **2022**, *12*.

[25] Y. Xin, K. Yu, L. Zhang, Y. Yang, H. Yuan, H. Li, L. Wang, J. Zeng, *Adv. Mater.* **2021**, *33*, 1.

[26] K. Sytwu, M. Vadai, J. A. Dionne, *Adv. Phys. X* **2019**, *4*.

[27] A. Gellé, A. Moores, *Curr. Opin. Green Sustain. Chem.* **2019**, *15*, 60.

[28] J. M. P. Martirez, J. L. Bao, E. A. Carter, **2021**.

[29] P. H. C. Camargo, E. Cortés, *Plasmonic Catalysis*, **2021**.

[30] L. V. Besteiro, P. Yu, Z. Wang, A. W. Holleitner, G. V. Hartland, G. P. Wiederrecht, A. O. Govorov, *Nano Today* **2019**, *27,* 120.

[31] J. Zhao, S. Xue, R. Ji, B. Li, J. Li, *Chem. Soc. Rev.* **2021**, *50*, 12070.

[32] C. H. Choi, K. Chung, T. T. H. Nguyen, D. H. Kim, *ACS Energy Lett.* **2018**, *3*, 1415.

[33] M. Rasmussen, A. Serov, K. Artyushkova, D. Chen, T. C. Rose, P. Atanassov, J. M. Harris, S. D. Minteer, *ChemElectroChem* **2019**, *6*, 241.

[34] J. B. Lee, S. Choi, J. Kim, Y. S. Nam, *Nano Today* **2017**, *16*, 61.

[35] F. X. Xiao, B. Liu, *Adv. Mater. Interfaces* **2018**, *5*, 1.

[36] M. Wu, W. J. Chen, Y. H. Shen, F. Z. Huang, C. H. Li, S. K. Li, *ACS Appl. Mater. Interfaces* **2014**, *6*, 15052.

[37] S. Yu, A. J. Wilson, G. Kumari, X. Zhang, P. K. Jain, *ACS Energy Lett.* **2017**, *2*, 2058.

[38] S. Li, P. Miao, Y. Zhang, J. Wu, B. Zhang, Y. Du, X. Han, J. Sun, P. Xu, *Adv. Mater.* **2021**, *33*, 1.

[39] E. B. Creel, E. R. Corson, J. Eichhorn, R. Kostecki, J. J. Urban, B. D. McCloskey, *ACS Energy Lett.* **2019**, *4*, 1098.

[40] J. S. Duchene, G. Tagliabue, A. J. Welch, W. H. Cheng, H. A. Atwater, *Nano Lett.* **2018**, *18*, 2545.

[41] M. Moura de Salles Pupo, R. Kortlever, *ChemPhysChem* **2019**, *20*, 2926.

[42] M. König, J. Vaes, E. Klemm, D. Pant, *iScience* **2019**, *19*, 135.

[43] Y. Hori, R. Takahashi, Y. Yoshinami, A. Murata, *J. Phys. Chem. B* **1997**, *101*, 7075.

[44] M. Gattrell, N. Gupta, A. Co, *J. Electroanal. Chem.* **2006**, *594*, 1.

[45] A. S. Varela, M. Kroschel, T. Reier, P. Strasser, *Catal. Today* **2016**, *260*, 8.

[46] M. R. Singh, Y. Kwon, Y. Lum, J. W. Ager, A. T. Bell, *J. Am. Chem. Soc.* **2016**, *138*, 13006.

[47] D. Faggion, W. D. G. Gonçalves, J. Dupont, *Front. Chem.* **2019**, *7*, 1.

[48] J. F. Brennecke, B. E. Gurkan, *J. Phys. Chem. Lett.* **2010**, *1*, 3459.

[49] F. Zhou, S. Liu, B. Yang, P. Wang, A. S. Alshammari, Y. Deng, *Electrochem. commun.* **2014**, *46*, 103.

[50] T. N. Huan, P. Simon, G. Rousse, I. Génois, V. Artero, M. Fontecave, *Chem. Sci.* **2016**, *8*, 742.

[51] M. C. Figueiredo, I. Ledezma-Yanez, M. T. M. Koper, *ACS Catal.* **2016**, *6*, 2382.

[52] Á. Díaz-Duque, A. P. Sandoval-Rojas, A. F. Molina-Osorio, J. M. Feliu, M. F. Suárez-Herrera, *Electrochem. commun.* **2015**, *61*, 74.

[53] G. T. Cheek, *ECS Meet. Abstr.* **2014**, *MA2014-01*, 836.

Chapter 2. Plasmon-enhanced CO_2 Valorization on Copper-Based Electrocatalysts

Tatiana Morin Caamano[a], *Mohamed S. E. Houache*[b], *Martin Couillard*[b], *Matthew Turnbull*[b], *Arnaud Weck*[c], *Yaser Abu-Lebdeh*[b] *Elena A. Baranova*[a]

[a] Department of Chemical and Biological Engineering, Center for Catalysis Research and Innovation (CCRI), University of Ottawa, Ottawa, Ontario K1N 6N5, Canada

[b] Energy, Mining and Environment Research Centre, National Research Council of Canada, Ottawa, Ontario K1A 0R6, Canada

[c] Department of Mechanical Engineering, Center for Research in Photonics, University of Ottawa, Ontario K1N 7N5, Canada

Chapter as prepared manuscript for publication.

Supplementary Information for this chapter is found in Appendix A.

Abstract

CO_2 electrochemical reduction is a promising technology to recycle CO_2 into fuels and chemicals. Copper has been in the forefront of research advances, as it is the only known metal to produce hydrocarbon products but is hindered by its poor selectivity. Use of Cu-based bimetallic particles have shown to improve selectivity, as well as stability of the catalysts. However, further advancements in the activity are also still needed to reach commercial viability. Through the use of light via photocatalysts, increases in activity has been observed. New research into photocatalysts has involved the use of plasmonic effects induced by localized surface plasmon resonance (LSPR) that occurs in metallic nanostructures of Ag, Au, Al and Cu. Previous work has focused on exciting the plasmonic response through laser and light at particular wavelengths of the exhibited LSPR of the catalysts. In this work, exploration into the use of a broad visible-range light source for the exploitation of the plasmonic effect in Cu, Ag and Cu-Ag bimetallic nanoparticle catalysts was conducted. Active metallic catalysts for the reaction were synthesized through a one pot chemical reduction and compared to commercial nanoparticles. Through TEM, EELS, XRD and XPS characterization, variation of Cu loading in the bimetallic particles demonstrated turning of their morphologies. A core-shell structure was found for the $Cu_{75}Ag_{25}$ synthesized particles. Through CV and chopped-light CA electrochemical tests, the synthesized Cu, $Cu_{60}Ag_{40}$ and $Cu_{85}Ag_{15}$ nano catalysts demonstrated superior CO_2ER performance to commercial Cu, CuO, and CuAg catalysts. Additionally, 15 to 26% promotion in activity with response to light, which was attributed to plasmonic effects, was observed for the first time with the use of a broad visible wavelength range cold halogen lamp as the source of light.

Graphical Abstract

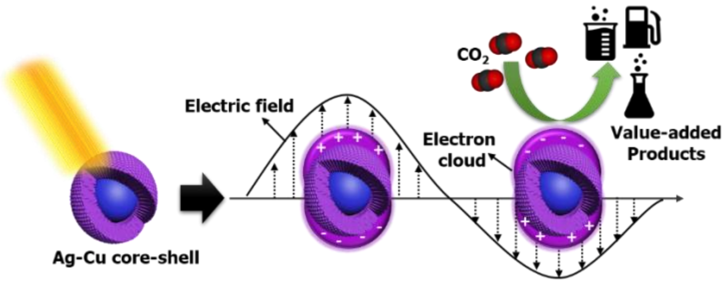

2.1. Introduction

The continuing accumulation of atmospheric carbon dioxide (CO_2) has become a crucial issue due to the threat that the current climate crisis poses on the environment, human health and security due to increasing intensity of natural disasters[1,2]. An estimated 70 - 80% of greenhouse gas emissions are sourced from the energy, transportation, and chemical industries[3,4]. As a result, the reduction of emissions from these sectors is crucial to substantially mitigate the cumulating effects of climate change. Therefore, moving towards alternative sustainable sources for the production of fuels and chemicals is a critical necessity.

The electrochemical reduction (ER) of CO_2 is a promising process that is able to convert CO_2 into higher value products[5–7]. Coupled with carbon capture and renewable energy resources, the technology can be implemented as a net-zero carbon emission process[8]. A large portion of catalysis research for the application has focused on copper (Cu), as it has been identified as an important metal catalyst by its unique ability to produce hydrocarbon products[6,8–10]. However, Cu possesses low selectivity and stability hindering commercial viability[6,7,9]. Previous work for improving CO_2ER catalysis performance has shown that coupling of copper with CO selective noble metals such as silver (Ag) and gold (Au), can improve selectivity towards value-added products, and aid in stability by reducing oxidation of the copper[6,7]. Despite the findings, these catalysts have yet to achieve the performance levels required for commercialization.

Efforts to also enhance the reaction performance has been through the activity of the CO_2ER reaction. Some of these advancements have involved the use of light, leading to photo-electrochemical approaches. However, traditional photo-electrocatalysts have involved coupling metallic catalysts with costly semiconductors[11,12]. More recently, it has been identified that CO_2 electroreduction can utilize plasmonic catalysis via localized surface plasmon resonance

(LSPR)[13]. Through LSPR, light irradiation directly excites the electrons in the metallic nanostructures enhancing the electromagnetic field, generating hot carriers and/or inducing local photothermal effects on the metals[13]. Ag and Au are the most popular plasmonic metals due to their strong LSPR effects that include the visible range of light[13–15]. However, recent advances in plasmonic catalysis for CO_2ER have included coupling these metals with Cu, which also possesses a LSPR effect in the visible light range[13,14]. This combined approach reduces the cost of the catalysts, allows the production of hydrocarbon products and, as previously mentioned, also has the added benefit of improving stability and selectivity of the Cu material for CO_2ER.

Previous work on plasmonic catalysis for CO_2ER has focused on the use of lasers or irradiation with a particular wavelength of light[14,16]. This work explores the use of a broad visible-range white light to incite the plasmonic response on copper, silver as well as copper-silver bimetallic nanoparticle catalysts for CO_2ER. In this way, approaching the use of plasmonic response with broader sources or light, such as the sun. The nanoparticle catalysts were synthesized using a one-pot wet chemical reduction in water using sodium borohydride as a reducing agent. The metal loading effects on $Cu_{100-x}Ag_x$ (x= 0, 50, 60, 75, 85, 100 at. %) particles are studied. Electrochemical tests involving cyclic voltammetry (CV) plots with light off and on, as well as chopped-light chronoamperometry (CA) measurements were utilized to evaluate the plasmonic photo-electrocatalytic performance.

2.2. Experimental Section

2.2.1. Chemicals

Material Synthesis

Copper nanoparticles were synthesized through chemical reduction in water using sodium borohydride as reducing agent[17,18]. Prior to the synthesis, all glassware was washed in aqua regia overnight. All water used in the synthesis consisted of ultrapure deionized water (18 MΩ), and all stirring conducted utilized magnetic stirring. First, $CuSO_4 \cdot 5H_2O$ (>98%, Fisher Scientific, USA) was dissolved in ultrapure deionized water (18 MΩ) to create a 50 mL solution of 0.02 M by stirring at room for about 20 minutes. Polyethylene glycol 6000 (PEG 6000, for synthesis, Sigma, USA) was also dissolved in water and stirred for about 10 minutes to form 100 mL of 0.02 M solution. The PEG solution was then added to the $CuSO_4 \cdot 5H_2O$ solution with continued stirring. An L-ascorbic acid (99%, Sigma, USA) and sodium hydroxide (NaOH, >98%) solution in water was then made by first dissolving the L-ascorbic acid salts to form 50 mL of a 0.04 M solution and adding a dropwise 0.5 M solution of NaOH until the pH of the solution reached 10. The solution was then stirred for an additional 10 minutes before adding to the master solution. After 10 minutes of further stirring the master solution, a sodium borohydride ($NaBH_4$, ≥98%, ACROS, Belgium) solution consisting of 30 mL of 0.068 M concentration was then added to reduce the precursor salts. The final solution was then stirred for 10 minutes. The suspension was then centrifuged at 6000 rpm for 6 minutes and the separated particles were washed with ultrapure deionized water 4 times. The particles were then freeze-dried to remove the remaining water overnight. The copper-silver bimetallic nanoparticles were synthesized similarly, with the addition of dissolving silver nitrate salts ($AgNO_3$, >99.9%, Alfa Aesar, USA) along with $CuSO_4 \cdot 5H_2O$ salts in the first step. All subsequent steps were then followed as previous. The silver nanoparticles utilized the substitution of dissolving 50 mL of 0.05 M silver nitrate salts instead of $CuSO_4 \cdot 5H_2O$ salts in the first step. However, the addition of L-ascorbic acid and sodium hydroxide solution was omitted. To adjust for the volume, the added PEG 6000 was instead of 150 mL of 0.033 M. In addition, the sodium borohydride concentration was of 35 mL of 0.15 M. All other steps were maintained.

Commercial Nanoparticles

Copper nanopowder (Cu commercial, 25 nm particle size TEM) was purchased from Sigma-Aldrich. CuO nanopowder (CuO commercial, 40 nm TEM) was purchased from US Research Nanomaterials, Inc. Silver-copper alloy nanopowder (CuAg commercial, <100 nm TEM, ~97.5% Ag and ~2.5% Cu) was purchased from Sigma-Aldritch, Silver nanopowder (Ag commercial, <100 nm TEM) was also purchased from Sigma-Aldritch.

2.2.2. Physiochemical Characterization

X-ray powder diffraction (XRD) was used to analyze the composition and crystalline structure of the nanoparticles. XRD samples were prepared by placing catalyst nanopowder on a Si crystal zero diffraction plate (MTI Corporation, USA). The XRD studies were conducted with a Rigaku Ultima IV PXRD under copper K radiation (λ = 1.5418 Å) set to 40kV/44mA. The scanning 2θ range was of 20 to 80 degrees with a step of 0.1 degrees. The Transmission electron microscopy (TEM) micrographs were obtained using JEOL JEM 2100F Field Emission (FE) transmission electron microscope operating at 200 kV. Electron energy loss spectroscopy (EELS) measurements for these samples were carried out on a FEI Titan 80-300 microscope operated at 300 keV with a Quantum EELS spectrometer fitted with a K2 direct electron detector camera from Gatan. TEM and EELS samples were prepared by dispersing the catalyst nanopowder in ethanol and sonicating for 5 minutes. Afterwards, one drop of the solution was placed onto a 200 mesh TEM copper grid coated with lacey carbon support film (Ted Pella Inc.) and dried in air prior to measurements. X-ray photoelectron spectroscopy (XPS) analyses were carried out using an Axis Ultra DLD spectrometer (Kratos Analytical,Manchester, UK) with monochromatized Al K α X-rays.

2.2.3. Electrochemical Characterization

Cell Set-Up

A three-electrode cell set-up with ~60 mL of aqueous 0.1 M potassium bicarbonate ($KHCO_3$, 99%, Alfa Aesar, USA) in ultrapure deionized water solution was used. The electrochemical cell body consisted of a small-volume quartz glass cell (Pine Research, USA). The reference electrode consisted of an $Hg/HgSO_4$ reference electrode (ALS Co., Japan). For the counter electrode a Pt wire was used (ALS Co., Japan). The working electrode consisted of 2 µL of particle catalyst ink deposited on an L-shaped glassy carbon electrode (3mm diameter, DEK Research). A white halogen cold-lamp (L-150A Series Cold Light Illuminator, 150 W Halogen Philips, dual light guide) was used as a light source. Images of the electrochemical set up with and without light can be seen in Figure A.1 in supporting information.

The catalyst ink was prepared with 6 mg of particle powder, 1 mL of deionized water (18 MΩ), 200 µL of isopropanol and 100 µL of Nafion® (~5%, Sigma Aldrich USA) mixed by sonication for approximately 5 minutes. Prior to deposition, the working electrode surface was polished with 30 µm and 5 µm alumina, rinsed with ethanol and then ultrapure deionized water and dried.

CV and CA Measurements

To evaluate the electrochemical activity, stability and plasmonic promotion cyclic voltammetry (CV) and chronoamperometry (CA) studies were conducted. All CV studies were carried out with the same conditions of range between -1.05 to -2.15 V vs $Hg/HgSO_4$ for 5 cycles with a step size of 50 mV/s. Three CVs were first conducted under N_2 purge, which was introduced by purging the electrochemical cell for 15 minutes with the N_2 gas (>99.99%). The first was conducted with the light off, then the second with the light on at maximum power and finally the third one with light off again. Once the tests were finalized CO_2 was introduced by purging the electrochemical cell for 15 minutes with CO_2 gas (>=99.99%). Then similarly three CVs were conducted in the order of light off, light on at maximum power, and finally again with light off. For stability and plasmonic evaluation, two types of CA experiments were conducted at a constant potential of -1.8 V vs $Hg/HgSO_4$. The first involved five short term CAs held for 18 minutes, which involved turning the light on and off intermittently at intervals of 3 minutes with different light powers of 141.2, 133, 113.9, 103.8, and 51.7 mW through variation of the lamp dial corresponding to the settings of 11/11, 10/11, 8/11, 6/11 and 4/11 respectively. The second involved long term CAs held for 3 hours, turning the light on and off intermittently at intervals of 30 minutes. For these tests the light was maintained at maximum power of 141.2 mW.

Plasmonic Measurements

The plasmonic promotion was evaluated using the enhancement ratio:

$$\rho = {}^{i}/_{i_0} \qquad \text{Equation 2-1}$$

where i and i_0 are the promoted under illumination and unpromoted dark current densities of the reaction. As such, for the plasmonic measurements the promoted activities were attributed to correspond to the current densities with light promotion, while the unpromoted activities correspond to the current densities without light promotion.

2.3. Results and Discussion

2.3.1. Characterization of Cu, Ag and Cu-Ag bimetallic catalysts

For morphological and size characterization, the nanoparticle catalysts were analyzed with TEM imaging (Figure 2.1), as well as EELS analysis for the $Cu_{60}Ag_{40}$, $Cu_{75}Ag_{25}$ and $Cu_{85}Ag_{15}$ bimetallic compositions (Figure 2.2).

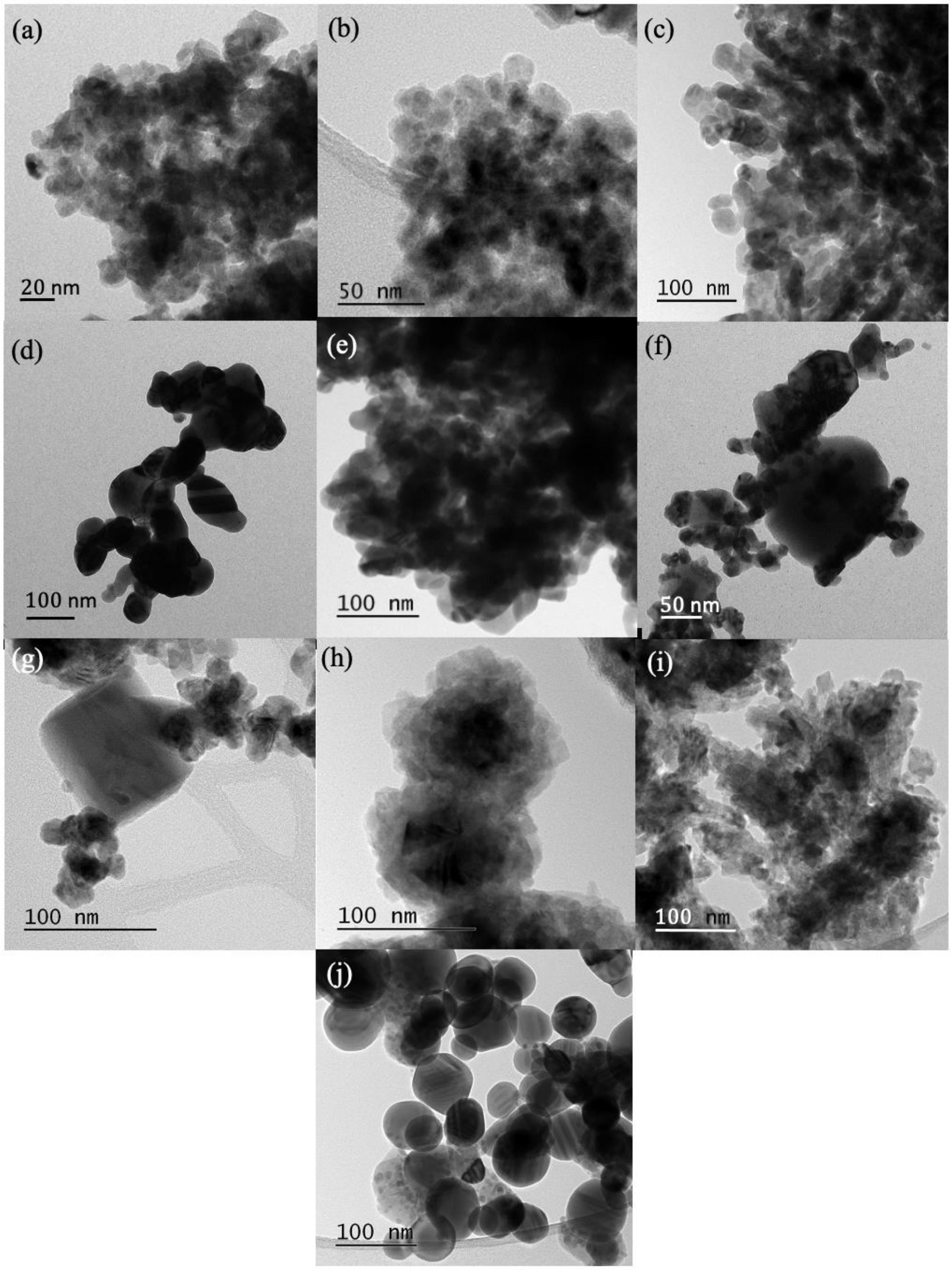

Figure 2.1: TEM characterization images of (a) Cu synthesis, (b) Cu commercial, (c) CuO commercial, (d) Ag synthesis, (e) Ag commercial, (f) $Cu_{50}Ag_{50}$ synthesis, (g) $Cu_{60}Ag_{40}$ synthesis, (h) $Cu_{75}Ag_{25}$ synthesis, (i) $Cu_{85}Ag_{15}$ synthesis, (j) CuAg commercial.

Figure 2.1a,b and c correspond to the Cu synthesis, Cu commercial and CuO commercial, respectively. Overall, all the Cu particles demonstrated occurrence of agglomeration. Notably, size differed between the particles based on the scale. The Cu synthesis exhibited the smaller apparent size of ~ 20 nm in diameter. Meanwhile, Cu commercial and CuO commercial exhibited a size of ~25 nm and ~40 nm in respective diameters, confirming both manufacturer's indication. The Ag synthesis and Ag commercial nanoparticles are presented in Figure 2.1d and e respectively. Both particles demonstrated evidence of agglomeration. In terms of size, the distribution was more uniform for the Ag commercial particles with sizes between ~25 - 50 nm. The Ag synthesis particles were larger with a predominant distribution of ~50 - 100 nm. Figure 2.1f-i corresponds to the synthesized bimetallic nanoparticles of $Cu_{50}Ag_{50}$, $Cu_{60}Ag_{40}$, $Cu_{75}Ag_{25}$ and $Cu_{85}Ag_{15}$ in respective order. Evidence of formation of larger particles of ~50 – 100 nm in size decorated by smaller particles of ~20 nm in size is observed. It is also seen that there is increasing agglomeration of the smaller particles around the larger particles with increase of Cu loading. From the EELS measurements in Figure 2.2a-c it is indicated that the larger particles consisted of Ag while those decorative smaller particles are that of Cu and Cu oxides. Notably, in Figure 2.2b for the $Cu_{75}Ag_{25}$ evidence of spherical Ag-Cu core-shell formation is seen, consisting of a core size of about ~50 nm with a shell thickness of ~25 nm. Further increase in loading for the $Cu_{85}Ag_{15}$ synthesis in Figure 2.2c, encapsulation of the Ag core by Cu particles is still observed. However, due to increase Cu agglomeration, the shell formation begins to break. Finally, Figure 2.1j corresponds to the CuAg commercial alloy. Agglomeration is not as evident compared to the other particles and size is distributed between ~50-100 nm.

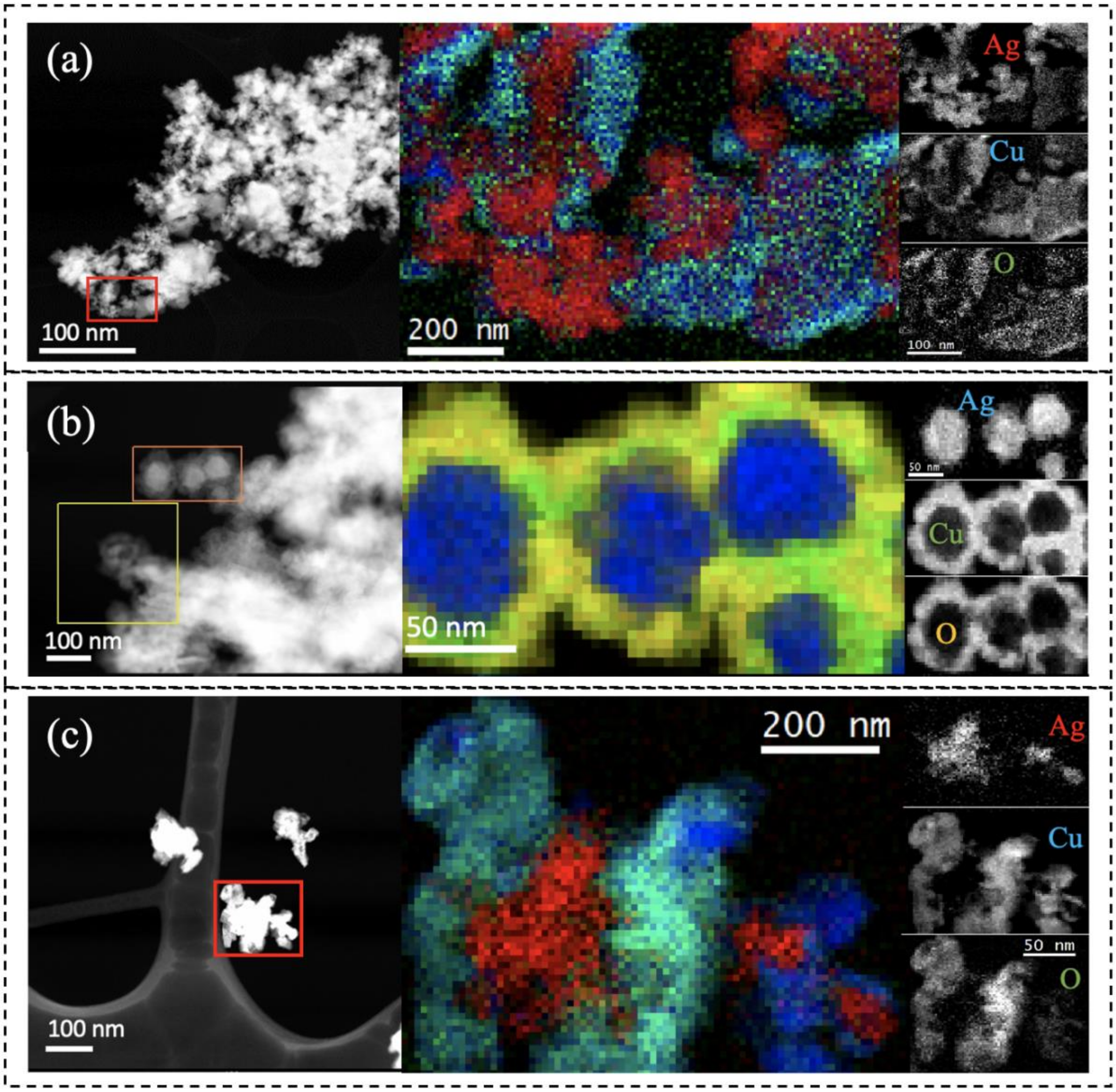

Figure 2.2: EELS images of (a) $Cu_{60}Ag_{40}$, (b) $Cu_{75}Ag_{25}$ and (c) $Cu_{85}Ag_{15}$ nanoparticles.

To analyze the composition of the particles, XRD characterization was conducted on all the nano-powders. Figure 2.3a-c show the XRD characterization peaks for the Cu particles, Ag particles, and the CuAg particles, respectively. The Cu synthesis (Figure 2.3a) showed a maximum intensity refraction peak at 43.21^{O} with two other smaller peaks at 50.38^{O} and 74^{O}, which align with the respective face centered cubic (fcc) structure (111), (200), and (220) planes of Cu (JCPDS no. 4-836)[19].

Other minor peaks were also evident at 35.44^{o}, 38.54^{o}, 48.9^{o} aligning to the CuO (-111), (111) and (-202) monoclinic structure planes (JCPDS no. 5-661)[20], as well as at 36.38^{o} and 61.42^{o} closely corresponding to Cu_2O (111) and (220) fcc planes (JCPDS no. 5-667)[20]. As such, despite efforts to suppress oxidation through the addition of the L-ascorbic acid addition step in the synthesis, oxidation was still present. This was expected, due to the known instability of the nanoparticles. Comparatively, the CuO commercial (Figure 2.3a) demonstrated two maximum intensity peaks at 35.46 ^{o} and 38.72 ^{o} with smaller peaks at 32.47^{o}, 48.78^{o}, 53.46^{o}, 58.23^{o}, 61.54^{o}, 66.25^{o}, 68^{o}, 72.4^{o} and 75.04^{o}, all attributed to the (-111), (111), (110), (-202), (020), (202), (-113), (-311), (220), (311) and (-222) monoclinic structure planes of CuO (JCPDS no. 5-661)[20]. Meanwhile, the Cu commercial showed three main peak at 43.29^{o}, 50.42^{o} and 74.08^{o} which align with the (111), (200) and (220) planes of the face centered cubic (fcc) structure of pure Cu (JCPDS no. 4-836)[19]. Cu commercial also exhibited a minor peak at 36.42^{o} aligning to the Cu_2O (111) fcc plane (JCPDS no. 5-667)[20] demonstrating small evidence of oxidation, however not as significant as that observed in the CuO commercial and Cu synthesis. The average crystallite sizes (D) estimated from the Debye-Scherrer formula were determined to be of 8.25 nm for Cu synthesis, 10.43 nm for CuO commercial, and 17.35 nm Cu commercial nanoparticles. The Ag synthesis XRD characterization (Figure 2.3b) showed a major peak at 38.09^{o} with minor peaks at 44.26^{o}, 64.42^{o} and 77.34^{o} in alignment with the fcc structure of Ag (Ref no. 01-087-0719)[21] . Similarly, the Ag commercial showed peaks at 38.09 ^{o}, 44.3^{o}, 64.47^{o} and 77.42^{o} corresponding to the fcc structure of Ag (Ref no. 01-087-0719)[21]. The found average crystallite sizes were determined to be of 28.59 nm for Ag synthesis and 16.94 nm for the Ag commercial. In Figure 2.3c, the XRD intensity peaks for the CuAg synthesized particles with different loading and CuAg commercial alloy bimetallic particles are shown. The main peaks identified in the synthesized nanoparticles aligned closely to those corresponding to Cu_2O (111), Cu (111) and Ag (111) at the 2θ points of 36.38±0.03°, 43.25±0.01° and 38.09±0.01°. Notably, with increasing Cu loading and decreasing Ag loading from the $Cu_{50}Ag_{50}$ to the $Cu_{85}Ag_{15}$ particles, a corresponding decreasing Ag (111) peak intensity and an increase in Cu (111) and Cu_2O (111) peaks intensity is observable. Other minor peaks were also observed aligning to Cu (200) and Cu (220), Cu_2O (2220), Ag (200), Ag (220), and Ag (311) planes.

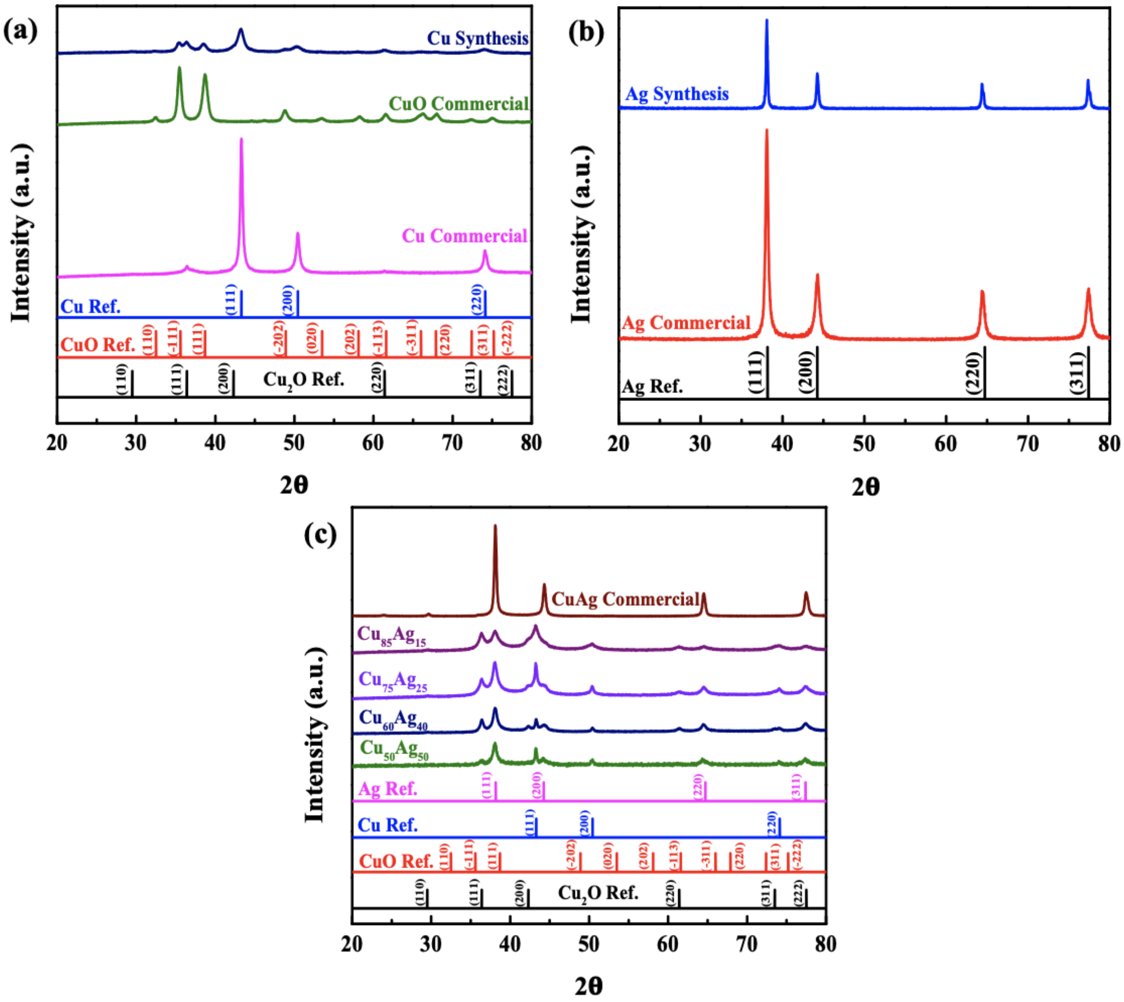

Figure 2.3: XRD patterns of (a) Cu commercial and synthesized particles, (b) Ag commercial and synthesized, and (c) CuAg bimetallic commercial and synthesized particles.

The CuAg commercial alloy demonstrated peaks seemingly aligning to the (111), (220) and (311) fcc structure planes of Ag (Ref no. 01-087-0719)[21]. However, the peak values were found to be of 38.13°, 44.32°, 64.52° and 77.5° demonstrating shifts ranging between 0.05 and 0.1° from reference values[21], thus indicating evidence of alloy composition. The average crystallite sizes (D) estimated from the Debye-Scherrer formula were determined to be of 20.5, 13.53, 11.18, 7.94 nm for the $Cu_{50}Ag_{50}$, $Cu_{60}Ag_{40}$, $Cu_{75}Ag_{25}$ and $Cu_{85}Ag_{15}$ synthesis particles, and 21.73 nm for CuAg commercial alloy

Figure 2.4 and Figure A.3 illustrate the XPS results of peak fitting that identify the speciation of the Cu, Ag, O and trace C elements along with the oxidation state at the surface of the $Cu_{75}Ag_{25}$ and Cu syntheses, and CuO commercial nanoparticles. Results of the peak fittings to the observed XPS spectra are listed in Table A.2. Peaks assigned to $Cu2p_{3/2}$ and Cu LMM in Figures 2.4 are compared to those from standards and indicate that Cu is predominately in the +2 oxidation state for CuO commercial and $Cu_{75}Ag_{25}$ particles. Meanwhile, spectra for Cu indicates a predominant +1 oxidation state. In addition to Cu, Ag is also analyzed in $Cu_{75}Ag_{25}$ particles with peaks assigned to Ag 3d, demonstrating a predominant occurrence in +1 oxidation state in the Ag. The peak deconvolution of the O 1s region of the XPS spectrum in Figure A.3 show the presence of defect sites, carbonate, and oxygenated organic species. The functional groups associated with these species are identified from the peak fitting to the C 1s region of the XPS spectrum in Figure A.3.

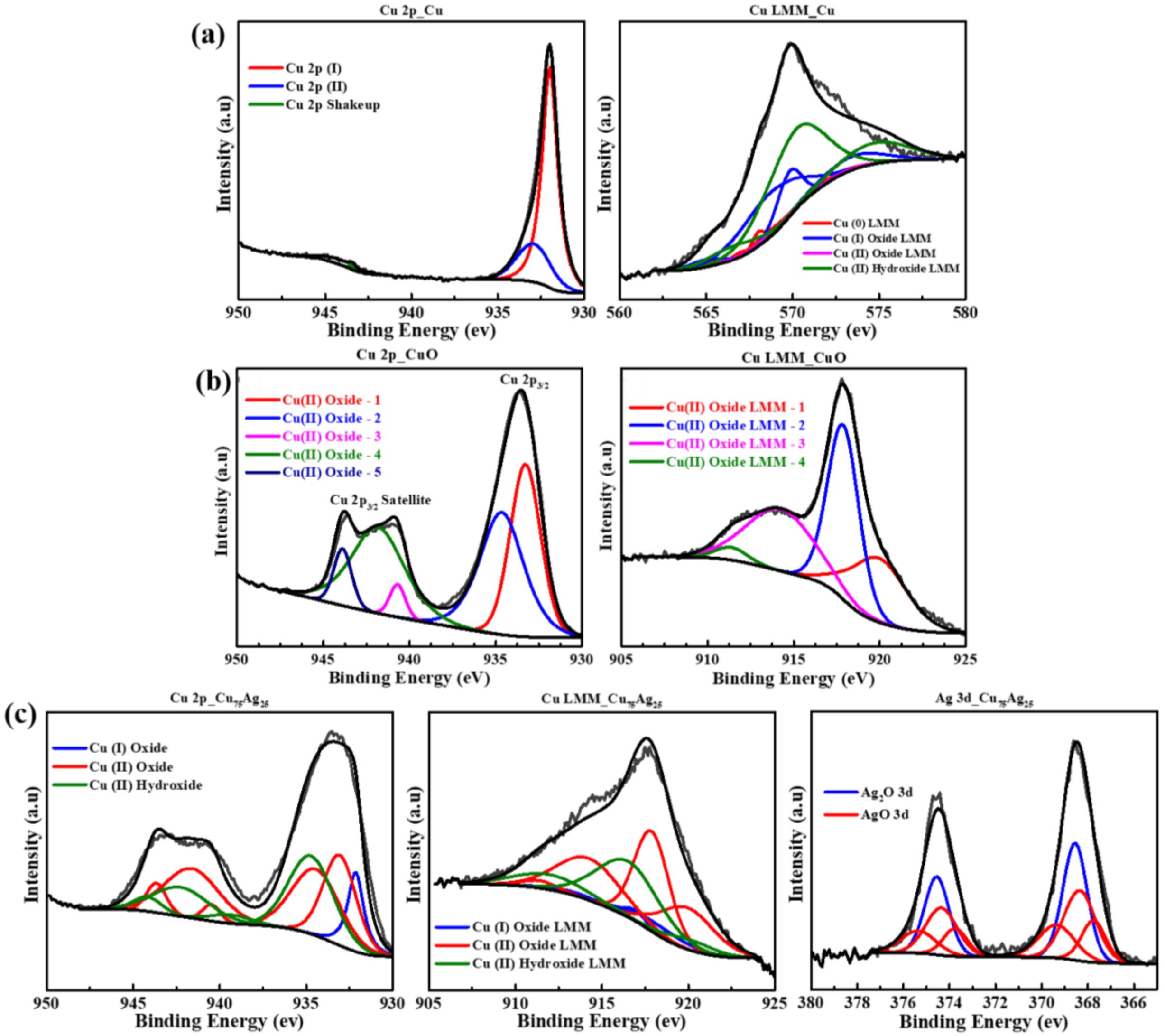

Figure 2.4: XPS spectra of (a) Cu, (b) CuO and (c) $Cu_{75}Ag_{25}$ nanoparticles used in our studies with peak fittings assigned to functional groups. Results of the peak fittings are listed in Table A.2.

2.3.2. Electrochemical Results

The electrochemical CO_2 activity was assessed through CV studies first under N_2 purge to obtain the HER activity as background, and then with CO_2 purge to determine the combined HER and CO_2ER activities. A summary of the maximum current densities of the 5th CV cycles under N_2 and CO_2 for all tested catalysts is presented in Figure 2.5. The CV plots for the synthesized catalysts are shown in Figure 2.6a-f, while those for the commercial catalysts are provided in the SI Figure A.2a-d. In Figure 2.5, beside the maximum current density bars, a calculated difference between the CO_2 and N_2 purge activities is presented as an estimate of the activity of the CO_2ER shown in red. A tabulated summary of the above values are provided in the Table A.1.

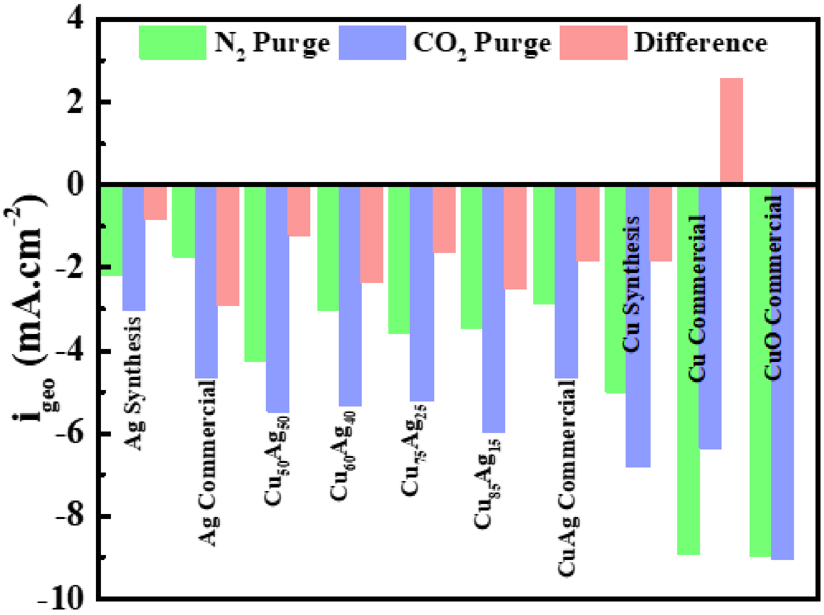

Figure 2.5: Summary of maximum current densities of the 5th CV cycles at -2.15 V vs Hg/HgSO₄ under N₂ purge (green) and CO₂ purge (blue) along with the difference between the CO₂ and N₂ purge (red) for all nanoparticle catalysts.

Overall, the synthesized particles showed evidence of CO_2ER, as the CO_2 purge current densities demonstrated more negative values to those under N_2 purge. In terms of electrocatalytic performance, it was found that the synthesized Ag underperformed compared to its commercial counterpart, which exhibited a more negative current density difference by a factor of 3.5. Notably, although the synthesis was able to be used with a small modification for the synthesis of Ag nanoparticles, it needs to be improved for electrochemical performance. The opposite trend is observed for the synthesized Cu nanoparticles. These exhibited superior performance to the commercial counterparts of Cu and CuO commercial, which showed little to no evidence of

CO_2ER occurring. Compared to CuO commercial, the Cu particles exhibited a current density difference 30 times larger. Meanwhile, Cu commercial exhibited no evidence of CO_2ER with decreasing activity from N_2 to CO_2 purge. For the Cu-Ag bimetallic syntheses, evidence of an increasing trend in the activity with increasing Cu loading from the difference in N_2 to CO_2 purge were observed, with $Cu_{75}Ag_{25}$ being an outlier. The found values for $Cu_{50}Ag_{50}$, $Cu_{60}Ag_{40}$, and $Cu_{85}Ag_{15}$ were of -1.21, -2.34, and -2.51 mA cm^{-2}. Meanwhile that of $Cu_{75}Ag_{25}$ was of -1.63 mA cm^{-2}. The increasing trend with Cu loading was expected to approach the performance of that of the Cu synthesis, which was observed to an extent. Notably, $Cu_{60}Ag_{40}$ and $Cu_{85}Ag_{15}$ demonstrated evidence of increased CO_2ER activity than that of the Cu synthesis, potentially explained by the added Cu-Ag interactions[8]. Also comparatively, the CuAg commercial alloy displayed a difference of -1.82 mA cm^{-2}, showing improved performance to $Cu_{50}Ag_{50}$ and $Cu_{75}Ag_{25}$.

More detail pertaining to the CV behaviour under N_2 purge and CO_2 purge under no light and with light exposure on the synthesized catalysts are shown in Figure 2.6. As summarized previously, the greatest differences between N_2 and CO_2 purges are observed in the $Cu_{60}Ag_{40}$ and $Cu_{85}Ag_{15}$ bimetallic structures. Small changes in current densities with light irradiation can also be observed. Evidence of increases in activity with the effect of light were observed in the Cu synthesis, $Cu_{50}Ag_{50}$, $Cu_{75}Ag_{25}$, as well as $Cu_{85}Ag_{15}$. As small changes were observed through CV measurements, further testing was conducted under CA conditions to better evaluate the influence of the light on the catalytic activity.

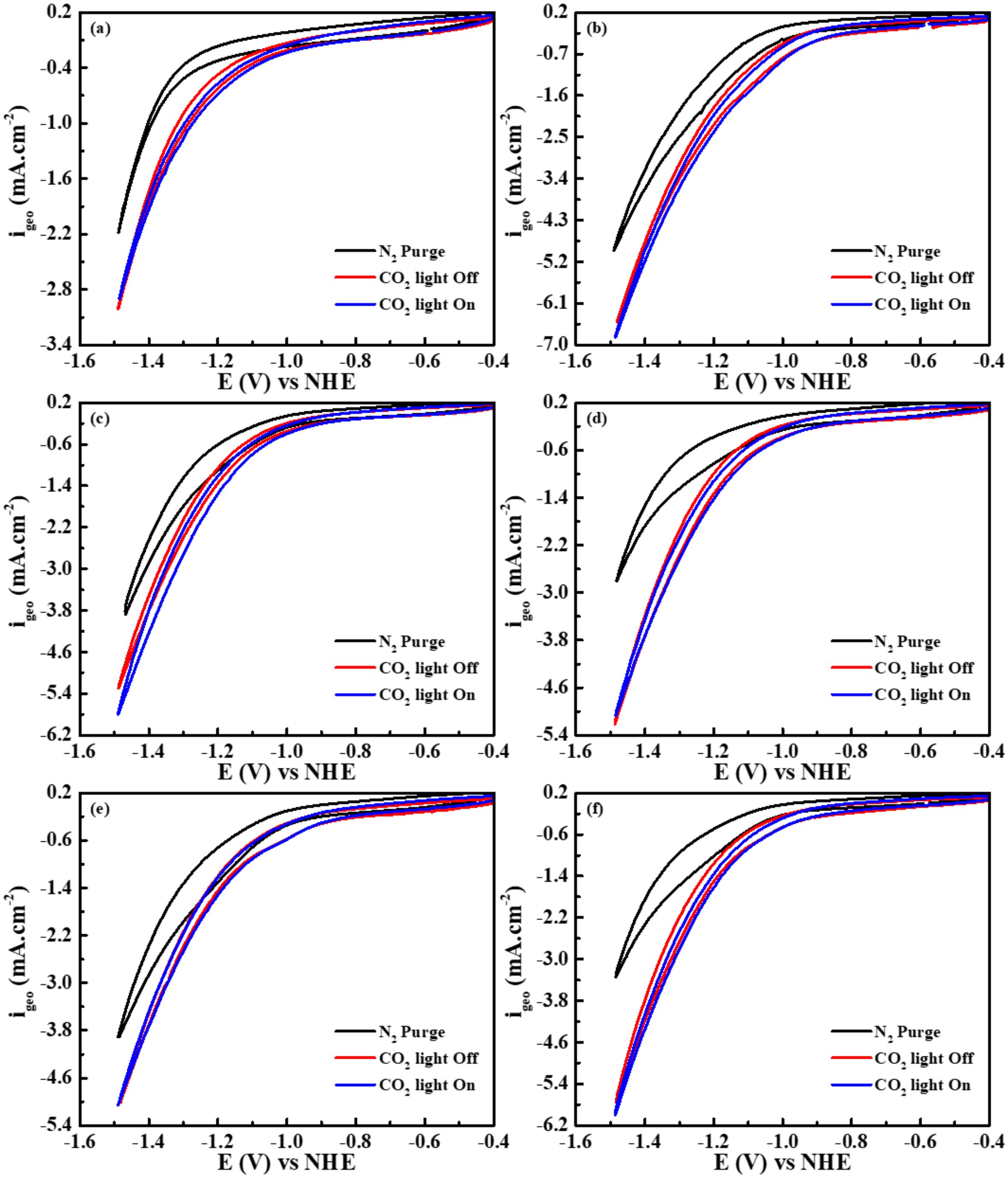

Figure 2.6: Cyclic Voltammograms of (a) Ag synthesis, (b) Cu synthesis, (c) $Cu_{50}Ag_{50}$, (d) $Cu_{60}Ag_{40}$, (e) $Cu_{75}Ag_{25}$, and (f) $Cu_{85}Ag_{15}$ under N_2 purge, CO_2 purge with and without light at 50 mV.s^{-1} scan rate (fifth stable cycle).

After CV measurements, the plasmonic effect in relation to light response under maximum power were studied through short-term chopped-light CAs. In these measurements, potential was held constant for 18 minutes and the current density response to a set intermittent light exposure was evaluated. Under CA measurements, the synthesized and commercial particles exhibited increase in the current density under illumination using a broad visible-range cold white light. Thermal effects from the light itself were determined to be negligible, as the incidence of light did not heat the probe of the lamp and the incidence probe exhibited only ~2 ^{o}C change when left on overnight. The summary of the plasmonic promotions in all the evaluated catalysts under is displayed in Figure 2.7a, along with the CA measurements of the particles displaying better comparable performances in Figure 2.7b. The CA measurement plots under maximum light power for all evaluated particles are observable in Figure A.4.

Despite Ag synthesis exhibiting decreased CO_2ER activity, the plasmonic promotion was comparable to that of the Ag commercial particles with values of 1.18 and 1.16 respectively. The Cu synthesis showed improved plasmonic response of 1.19 compared to those of Cu and CuO commercial with values of 1.17 and 1.15 respectively. Although the values are similar, due to the poor CO_2ER activity seen previous, the plasmonic promotion of Cu and CuO commercial is mainly attributed to promotion of the competing HER reaction, which is not of interest. The synthesized bimetallic particles showed a rising plasmonic trend with increased Cu loading with the exception of $Cu_{60}Ag_{40}$. The plasmonic promotion values for $Cu_{50}Ag_{50}$ was of 1.15, while $Cu_{75}Ag_{25}$ and $Cu_{85}Ag_{15}$ both had a value of 1.16. The $Cu_{60}Ag_{40}$ synthesis outperformed the other bimetallic syntheses with a value of 1.18. Predominantly, the particle with the best plasmonic response was that of the CuAg commercial alloy, displaying a promotion value of 1.26.

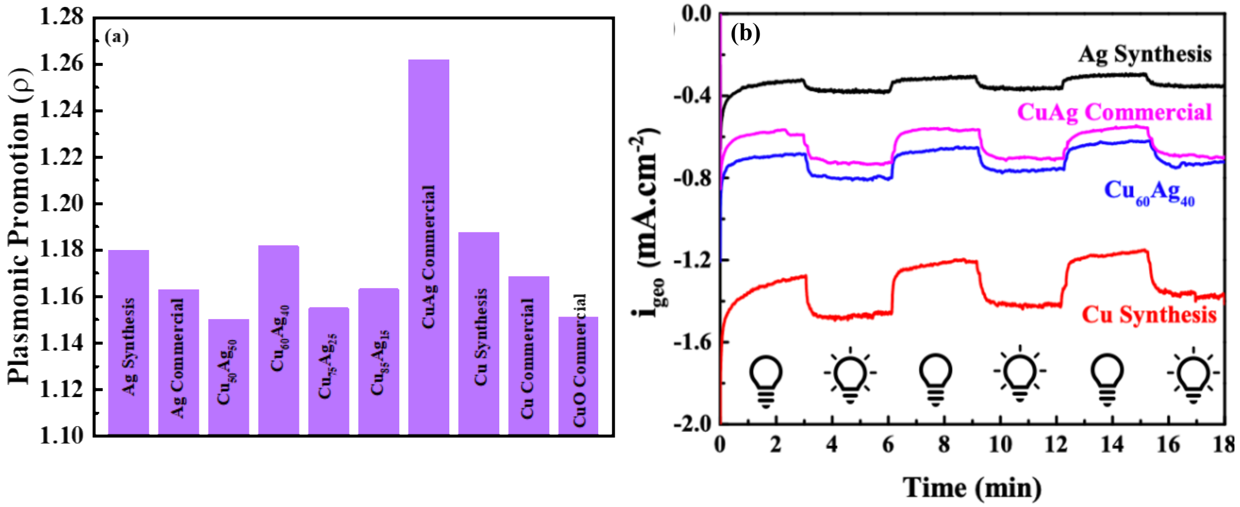

Figure 2.7: Chronoamperometry plots at -1.8 V vs $Hg/HgSO_4$ for 18 minutes under full light power where (a) summarizes the plasmonic promotion of all nanoparticle catalysts, and (b) displays the CA measurements of the particles with best plasmonic promotions.

The effects of the variation of light power on the activity was also studied. Figure 2.8 displays the summary of average current density points over 5 different powers for all the evaluated catalysts. A linear increasing current density trend is observed going from 51.7 to 141.2 mW throughout all evaluated catalysts. It was found through linear trends (shown in SI Figure A.5) that the slopes for Ag synthesis and Ag commercial were of -0.0011 $mA.cm^{-2}.mW^{-1}$ for both. Meanwhile for Cu synthesis, Cu commercial and CuO commercial the slopes were respectively of -0.0038, -0.0014 and -0.0021 $mA.cm^{-2}.mW^{-1}$. For the bimetallic particles, $Cu_{50}Ag_{50}$, $Cu_{60}Ag_{40}$, $Cu_{75}Ag_{25}$, $Cu_{85}Ag_{15}$ and the commercial CuAg particles, the slopes were in the respective order of -0.0033, -0.0024, -0.0018, -0.0014 and -0.0018 $mA.cm^{-2}.mW^{-1}$. Overall, all plots approached the average current density linear plot without light exposure as the power decreased, as seen in Figure A.5a-j. This relation displays that overall, the current density effects are a function of light power. Notably, thermal effects also display a linear trend in relation to current density. As no noticeable heat was emitted by the light probe to warm the quartz and electrolyte boundary in a matter of seconds or minutes, thermal effects could only be attributed to photo-thermal effects being induced by the light exposure of the catalytic surfaces. However, it is noted that further testing of the effect of temperature changes in the electrolyte could be tested to further corroborate this theory.

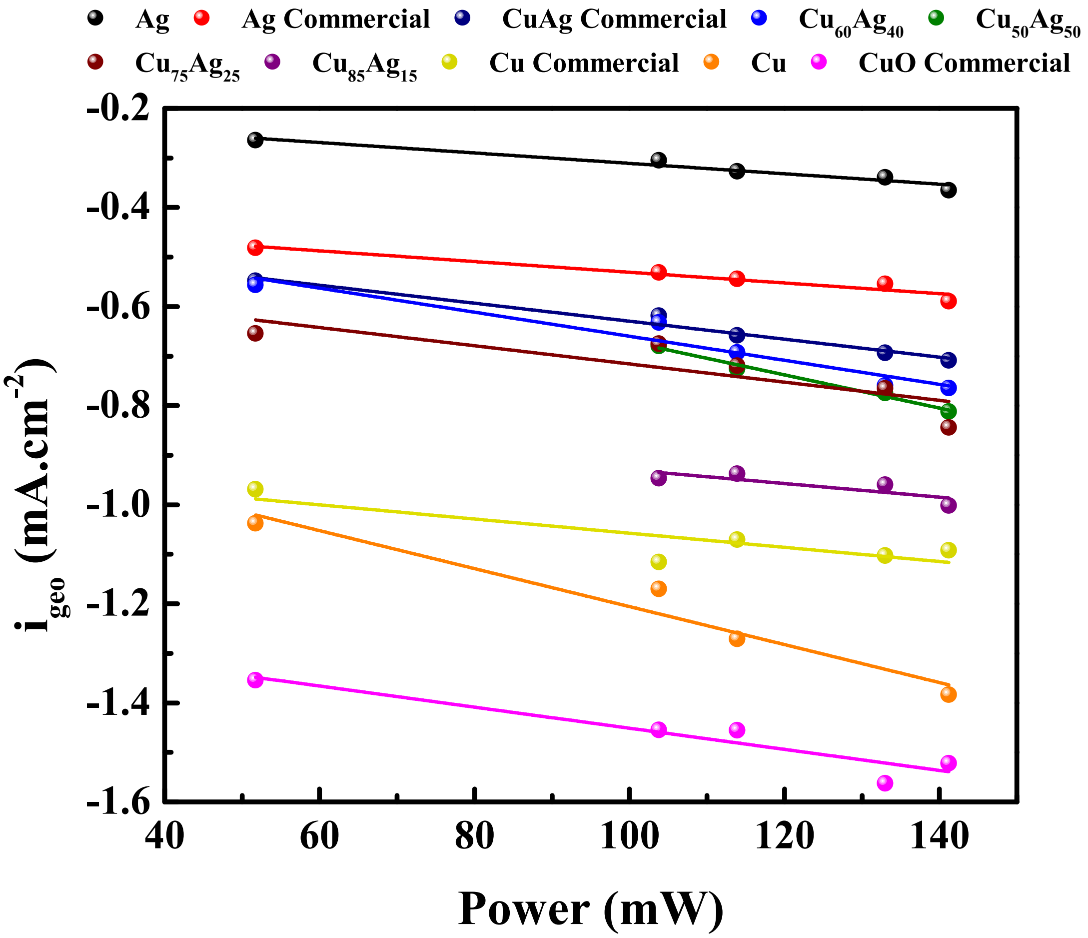

Figure 2.8: Trend summary of light power variation studies for all nanoparticle catalysts under a potential of -1.8 V vs Hg/HgSO$_4$.

The final measurements conducted involved those of the long-term CA effects of 3 hours utilizing the chopped light approach for identified synthesized catalysts of interest. These involved the synthesized Ag, Cu, as well as the $Cu_{60}Ag_{40}$ and $Cu_{75}Ag_{25}$ bimetallic particles. $Cu_{60}Ag_{40}$ was selected due to its increased plasmonic response and relatively high CO_2ER activity to the other bimetallic catalysts. Despite its relatively lower CO_2ER activity, $Cu_{75}Ag_{25}$ was selected due to its exhibited core-shell formation, as work in plasmonic catalysis has shown that core-shell particles can be used as antenna-reactor structures[22]. Wherein Ag, which has greater LSPR effect to Cu, can transfer its plasmonic response in the form of a forced plasmon to the shell, while the Cu particles act as the catalyst as it is able to interact with the outer environment.

The observable long-term effects in Figure 2.9a show that Cu displays the highest current density values, Ag the lowest, while the bimetallic particles display values intermediate to these. Ag displays the highest stability. On the other hand, Cu displays a decreasing activity trend over time, also displaying a decreasing plasmonic promotion as the steps decrease in size. The bimetallic particles stability behaviour is improved compared to Cu, while still displaying a relative decrease in activity compared to Ag. The average calculated plasmonic promotion values for these measurements are summarized in Figure 2.9b. Over a longer held potential period, the synthesized Ag maintained its plasmonic promotion at a value of 1.18. Meanwhile, the Cu synthesis displayed a decreased value of 1.06, an 11% decrease from the previous value of 1.19. For the bimetallic particles, both showed similar values with $Cu_{60}Ag_{40}$ displaying a promotion of 1.11 and $Cu_{75}Ag_{25}$ a promotion value of 1.13. Thus, showing a decrease of 5% and 3% respective to $Cu_{60}Ag_{40}$ and $Cu_{75}Ag_{25}$ from the corresponding previous values of 1.18 and 1.15.

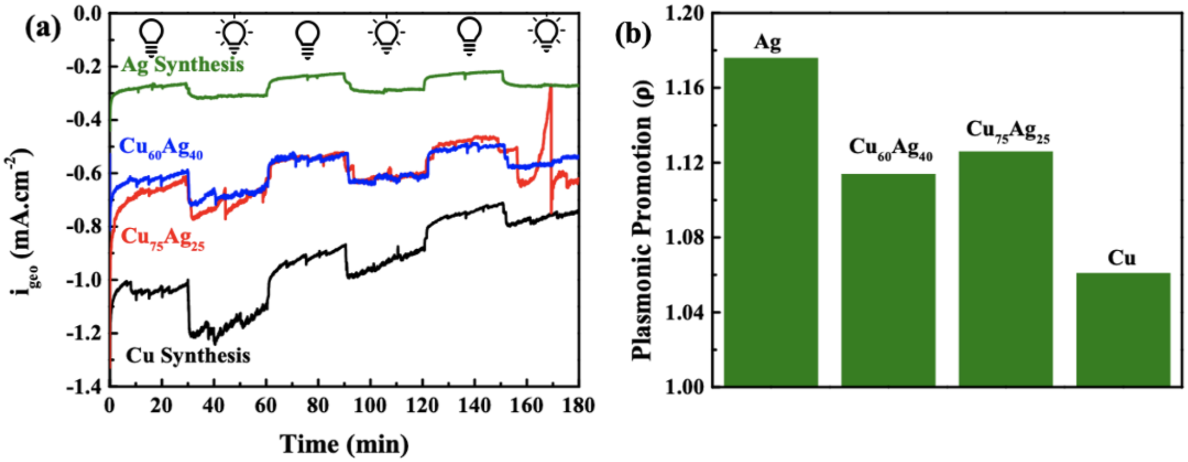

Figure 2.9: Stability results at -1.8 V vs Hg/$HgSO_4$ under full light power. (a) 3-hour CA plots under variable light on/off conditions and (b) calculated plasmonic promotions derived from 3-hour CAs for select synthesized catalysts.

In general, evidence of improvement of the CO_2ER performance was observed with the utilization of Cu-Ag bimetallic catalysts. An increase of a factor of ~3 was observed in the two best performing catalysts of $Cu_{60}Ag_{40}$ and $Cu_{85}Ag_{15}$ compared to synthesized Ag performance and an increase of a factor of 1.3 and 1.4 respectively compared to the Cu synthesis nanoparticles. Both bimetallic particles also exhibited superior performance to the CuAg alloy counterpart in terms of CO_2ER. Underperformance of $Cu_{50}Ag_{50}$ could indicate that the Cu loading was insufficient to compensate for the interactions of the Ag particles. Meanwhile, the poor performance of $Cu_{75}Ag_{25}$ did not follow the trend of increasing activity with Cu loading. This indicated that the difference in structure that of core-shell formation, could have inhibited the Cu-Ag interactions that seem to have played a role in increasing the $Cu_{60}Ag_{40}$ and $Cu_{85}Ag_{15}$ observed activities compared to Cu. Light responses were observed throughout all the catalysts irrespective of evidence of CO_2ER, indicating that HER was also promoted through light irradiation. Use of a white-halogen cold lamp provided negligible heat effects, and a broad visible-light spectrum. Light-induced increases in activity in chopped-light CAs were observed to change relatively instantaneously with light irradiation exposure. The light power was also varied to evaluate the response in the short-term 18-minute CA studies (Figure A.6 in SI). Throughout all the catalysts, a linear decreasing activity trend is observable with decreasing light power, which approaches the trend without light (Figure A.5). Therefore, the light effects were attributed to plasmonic catalytic enhancement. Maximum plasmonic promotion was exhibited in the CuAg commercial alloy. The main differences from the commercial CuAg particle to the synthesized Cu-Ag particles, is that the commercial particles are alloys and are also mainly comprised of Ag. As discussed previously, Ag is a stronger plasmonic metal than Cu. However, the commercial Ag nanoparticles did not exhibit significantly improved plasmonic effects to the Cu catalysts. Yet notably, the CuAg alloy nanoparticles do not exhibit agglomeration, which was seen in both the Ag synthesis and commercial particles. As such these differences may have led to an improved performance of the bimetallic synthesized particles, where $Cu_{60}Ag_{40}$ demonstrated the highest plasmonic response. It is plausible that the improved effect of the $Cu_{60}Ag_{40}$ synthesis over the other synthesized particles could be due to the cubic Ag structures that were observed to be formed. It has been found in previous work that cubic Ag structures exhibit multiple resonance peaks in the visible range[23], which under a white light would all be excited. Additionally, the electromagnetic field enhancement has also been shown to change with morphology, which could also be playing a role[24].

2.4. Conclusion

In summary, a light-response attributed to plasmonic effects was observed in the CO_2ER activity with the use of a broad visible-range cold white light. Increases in current density with light exposure were observed in CO_2ER active Cu, Ag and Cu-Ag bimetallic nanoparticles that were synthesized through a one-pot sodium borohydride reduction method. It was found that a maximum plasmonic promotion of 26% along with favorable CO_2ER performance was observed in the CuAg commercial alloy. The second most prominent performance was observed in the $Cu_{60}Ag_{40}$ synthesized bimetallic particle with a plasmonic promotion of 18%. The improved effects of the alloy and the $Cu_{60}Ag_{40}$ particles can potentially be related to their unique morphologies, as the alloy did not display agglomeration, while the $Cu_{60}Ag_{40}$ composite observed a unique cubic formation of the Ag. However, improved stability with no changes in plasmonic promotion over 3 hours was exhibited by the Ag synthesis. The increased stability of the Ag was likely sustained due to its properties as a noble metal. Overall, the integration of Cu-Ag bimetallic particles observed increased stability to the monometallic Cu. Additionally, indications towards synergetic effects were observed with increased current density differences between the HER and CO_2ER reduction to both monometallic Cu and Ag.

The found results highlight that further insights into Cu-Ag alloys should be further studied for the application of plasmonic CO_2ER. As agglomeration may have also played a role, exploration into synthesis approaches for dispersed particle catalysts along with their plasmonic electrochemical testing is required. In the future, product identification studies are also to be evaluated to test effects in selectivity in terms of differences between the synthesized and commercial particles, bimetallic loading, as well as due to plasmonic effects. Additionally, temperature effects of the system could be further evaluated to corroborate that plasmonic effects are mainly at play.

Acknowledgements

This research was enabled in part by support provided by the Natural Resources of Canada (NRC) under the Materials for Clean Fuel program (A1-017184).

References

[1] Y. Shimizu, WHO, “Climate change,” accessed on August 2, 2022, https://www.who.int/health-topics/climate-change#tab=tab_1.

[2] IPCC, “Climate change: a threat to human wellbeing and health of the planet. Taking action now can secure our future.,” **2022**, accessed on August 2, 2022, https://www.ipcc.ch/2022/02/28/pr-wgii-ar6/.

[3] H. Ritchie, M. Roser, R. Rosado, “CO2 and Greenhouse Gas Emissions,” *Published online at OurWorldInData.org*, **2020**, accessed on August 2, 2022, https://ourworldindata.org/co2-and-other-greenhouse-gas-emissions.

[4] I. Energy Agency, **2021**.

[5] B. Wu, J. Chen, L. Qian, *Catalysts* **2022**, *12*, 860.

[6] A. Vasileff, C. Xu, Y. Jiao, Y. Zheng, S. Z. Qiao, *Chem* **2018**, *4*, 1809.

[7] M. K. Birhanu, M. C. Tsai, A. W. Kahsay, C. T. Chen, T. S. Zeleke, K. B. Ibrahim, C. J. Huang, W. N. Su, B. J. Hwang, *Adv. Mater. Interfaces* **2018**, *5*, 1.

[8] S. Nitopi, E. Bertheussen, S. B. Scott, X. Liu, A. K. Engstfeld, S. Horch, B. Seger, I. E. L. Stephens, K. Chan, C. Hahn, J. K. Nørskov, T. F. Jaramillo, I. Chorkendorff, *Chem. Rev.* **2019**, *119*, 7610.

[9] J. Zhao, S. Xue, J. Barber, Y. Zhou, J. Meng, X. Ke, *J. Mater. Chem. A* **2020**, *8*, 4700.

[10] E. Ruiz-López, J. Gandara-Loe, F. Baena-Moreno, T. R. Reina, J. A. Odriozola, *Renew. Sustain. Energy Rev.* **2022**, *161*.

[11] N. Nandal, S. L. Jain, *Coord. Chem. Rev.* **2022**, *451*, 214271.

[12] N. Zhang, R. Long, C. Gao, Y. Xiong, *Sci. China Mater.* **2018**, *61*, 771.

[13] Y. Xin, K. Yu, L. Zhang, Y. Yang, H. Yuan, H. Li, L. Wang, J. Zeng, *Adv. Mater.* **2021**, *33*, 1.

[14] G. Kumari, X. Zhang, D. Devasia, J. Heo, P. K. Jain, *ACS Nano* **2018**, *12*, 8330.

[15] Z. Hirbodvash, O. Krupin, H. Northfield, A. Olivieri, E. A. Baranova, P. Berini, *Sci. Adv.* **2022**, *8*, 1.

[16] E. B. Creel, E. R. Corson, J. Eichhorn, R. Kostecki, J. J. Urban, B. D. McCloskey, *ACS Energy Lett.* **2019**, *4*, 1098.

[17] T. M. D. Dang, T. T. T. Le, E. Fribourg-Blanc, M. C. Dang, *Adv. Nat. Sci. Nanosci. Nanotechnol.* **2011**, *2*.

[18] E. Cossar, K. Agarwal, V. B. Nguyen, R. Safari, G. A. Botton, E. A. Baranova, *Electrocatalysis* **2021**, *12,* 605.

[19] T. Theivansanthi, M. Alagar, *Arch. Phys. Res.* **2010**, *1*, 112.

[20] R. Raghav, P. Aggarwal, S. Srivastava, *AIP Conf. Proc.* **2016**, *020078*.

[21] Kamar Shameli, M. Bin Ahmad, A. Zamanian, P. Sangpour, P. Shabanzadeh, Y. Abdollahi, M. Zargar, *Int. J. Nanomedicine* **2012**, *7,* 5603.

[22] K. Li, N. J. Hogan, M. J. Kale, N. J. Halas, P. Nordlander, P. Christopher, *Nano Lett.* **2017**, *17*, 3710.

[23] H. S. Al-Ghamdi, W. E. Mahmoud, *Mater. Lett.* **2013**, *105*, 62.

[24] V. Shvalya, G. Filipič, J. Zavašnik, I. Abdulhalim, U. Cvelbar, *Appl. Phys. Rev.* **2020**, *7*.

Chapter 3. Tuning the Polarity of Dinitrile-Based Electrolyte Solutions for CO_2 Electroreduction on Copper Catalysts

Tatiana. Morin Caamano[a], *Mohamed. S. E. Houache*[b], *Mario G. Sandoval*[c], *Martin. Couillard*[b], *Arnaud. Weck*[c], *Elena. A. Baranova*[a], *Yaser Abu-Lebdeh*[b]

[a] Department of Chemical and Biological Engineering, Center for Catalysis Research and Innovation (CCRI), University of Ottawa, Ottawa, Ontario K1N 6N5, Canada

[b] Energy, Mining and Environment Research Centre, National Research Council of Canada, Ottawa, Ontario K1A 0R6, Canada

[c] Department of Mechanical Engineering, Center for Research in Photonics, University of Ottawa, Ontario K1N 7N5, Canada

Chapter as prepared manuscript for publication.

Supplementary Information for this chapter is found in Appendix B.

Abstract

Development in carbon dioxide electrochemical reduction (CO_2ER) has mainly focused on aqueous electrolytes. However, due to low solubility of CO_2 in water, these are hindered by mass-transfer limitations. Organic electrolytes, such as methanol, acetonitrile and dimethylformamide, have been explored as an increased CO_2 solubility alternative. Yet, insights into other organic electrolytes are scarce. Dinitrile solvents have decreased polarity in comparison to acetonitrile and thus can potentially further increase CO_2 solubility and advance the reaction's performance. Herein, the novelty of dinitrile based electrolytes for the application of CO_2ER is explored.

Acetonitrile, adiponitrile and sebaconitrile were used to study the effects of a secondary nitrile group addition and dinitrile chain length on salt solubility, electrolyte conductivity and CO_2 solubility. Electrochemical effects were evaluated through cyclic voltammetry (CV) and chronoamperometry (CA) measurements with copper (Cu) and copper oxide (CuO) commercial nanoparticle catalysts. Finally, DFT calculations were employed to further explore the CO_2 interactions with the selected solvents.

Graphical Abstract

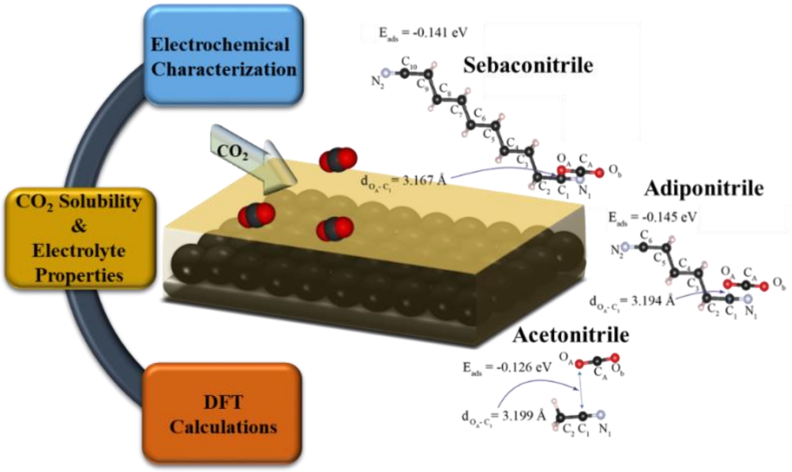

3.1. Introduction

The continual accumulation of carbon dioxide (CO_2) in the atmosphere due to anthropogenic sources has led to record levels of atmospheric global average CO_2, and thus the current climate crisis[1,2]. Due to the link of rising global temperatures to the increase of CO_2 accumulation since the beginning of the industrial age, this has led to the current climate crisis. The 2022 IPCC report has outlined that the world is on the path to reach a 1.5 °C increase in the next 20 years[3]. In order to avoid climate disasters associated with surpassing of this threshold, the development and implementation of sustainable alternative sources for fossil-derived fuels and feedstock chemicals is of crucial necessity[1].

Posing promising potential, is the CO_2 electrochemical reduction (CO_2ER) reaction by its ability to convert CO_2 to added value chemicals, such as energy-dense hydrocarbons like ethylene[1, 2]. In combination with carbon capture and renewable energy sources, the reaction can become a net carbon zero process. Copper (Cu) has particularly been identified as a catalyst of importance for the reaction, due to its unique ability to generate hydrocarbons[1,2,4]. Still, the technology continues to achieve commercial viability, as not only does Cu exhibit low selectivity, but also sufficiently high activities and stability of the catalytic performance are yet to be reached[1,2,4].

Aqueous-based electrolytes, such as bicarbonate or phosphate-buffered solutions, are commonly used for the reaction[5]. They possess advantages such as low-cost, wide-availability and low-toxicity[5,6]. However, they exhibit low CO_2 solubilities, thus resulting in performance drawbacks due to mass transfer limitations[5,6]. Organic solvent electrolytes have the advantage of possessing comparably higher CO_2 solubilities. In addition, due to limitation of available protons, these also suppress the competing hydrogen evolution reaction (HER)[5,6]. Due to the lack of hydrogen protons the CO_2ER also follows a different reaction pathway in aqueous solvents, that of the generation of the $CO_2^{-\cdot}$anion radical[5,6]. As a result, the Cu-catalyzed CO_2ER in organic electrolytes does not possess an extensive variety of reaction pathways as in the case of aqueous electrolytes, and thus has better viability to achieve improved product selectivity. However, a trade-off that is to be considered is the requirement of more negative potentials to achieve the CO_2ER anion radical pathway.

Nitrile-based organic electrolytes, such as acetonitrile (ACN), are known to possess high thermal and electrochemical stability. Solubility of CO_2 also has the potential to be further improved in nitrile-based solvents by decreasing the polarity by the addition of another carbon-nitrogen bond, present in dinitrile solvents. An additional advantage is also increased stability of the resulting dinitrile structures compared to ACN, which is volatile. Furthermore, the polarity and thus CO_2 miscibility can be further tuned in dinitrile-based solvents through variation of the chain length.

This work documents for the first time the effect of the use of organic dinitrile solvents with the evaluation of variation in chain length of dinitrile compounds on CO_2 solubility for the application of CO_2ER. The selected solvents under study were of acetonitrile, a studied mononitrile as comparison basis, as well as two dinitriles, adiponitrile (n=4) and sebaconitrile (n=8), where n indicates the number of methylene groups in the chain. A supporting electrolyte of tetrabutylammonium hexafluorophosphate ($TBAPF_6$) was used due to its wide potential window. Solubility limits of $TBAPF_6$ in the selected nitrile-based solvents were tested. Conductivity against concentration and temperature were also explored. Then, CO_2 solubility in the organic solvents was measured. Performance on CO_2ER was studied with the use of commercial copper-based catalysts through cyclic voltammetry (CV) and chronoamperometry (CA) measurements. Finally, a density function theory (DFT) analysis of the interactions between CO_2 and the nitrile solvents to understand the CO_2 solubility effects was carried out.

3.2. Experimental Section

3.2.1. Chemicals

Copper nano-powder (Cu NPs, 25 nm particle size TEM) was purchased from Sigma-Aldrich. CuO nano-powder (CuO NPs, 40 nm TEM) was purchased from US Research Nanomaterials Inc. The organic solvents consisted of acetonitrile (ACN, >99.9%, Sigma-Aldrich, USA), adiponitrile (ADN, 99%, Sigma-Aldrich, USA), and sebaconitrile (SBN 95%, Alfa Aesar, USA). The solvents were dried for 7 days using 3A, 3.2mm pellet molecular sieves (Sigma-Aldrich, USA). Tetrabutylammonium hexafluorophosphate ($TBAPF_6$, >99%, Sigma-Aldrich, USA) salts were dried in a vacuum oven at a temperature of 90 ℃ overnight. After drying, the organic electrolytes were prepared with 0.1 M $TBAPF_6$, 5 mM ferrocene (98%, Sigma, USA) in ACN, ADN or SBN. The aqueous electrolyte was a solution of aqueous 0.1 M potassium bicarbonate ($KHCO_3$, 99%, Alfa Aesar, USA) in deionized water (Milli-Q Millipore, 18.2 MΩ cm at 293 K).

3.2.2. Physiochemical Characterization

CO_2 solubility was quantitatively compared between the organic solvents using collected Fourier-transform infrared spectroscopy (FTIR) spectroscopy[7]. A Nicolet 6700 FTIR from Thermo Scientific equipped with a zinc selenide sample holder was used for ATR FTIR collection. Scanning range of the spectrum was of 4000 cm^{-1} to 650 cm^{-1}. The spectra was analyzed using Omnic™ software. From the resulting peak characteristic of CO_2 the areas were integrated using OriginPro® between the spectrum of 2200 cm^{-1} to 2400 cm^{-1}. The resulting areas were normalized over the integrated peak of anhydrous ethanol reference between the bounds of 2200 - 4000 cm^{-1}.

Then the beer lambert formula, shown by equation 3-1, was utilized to estimate the CO_2 concentration with use of the absorbance normalized area:

$$A = \varepsilon bC \qquad \text{Equation 3-1}$$

where A is the absorbance, ε is the molar absorptivity coefficient, b the length of light path, and C is the concentration. X-ray powder diffraction (XRD) was used to analyze the composition and crystalline structure of the nanoparticles. XRD samples were prepared by placing catalyst nanopowder on a Si crystal zero diffraction plate (MTI Corporation, USA). A Rigaku Ultima IV PXRD under copper K radiation (λ = 1.5418 Å) set to 40kV/44mA was utilized. The scanning 2θ range was of 20 to 80 degrees with a step of 0.1 degrees. Transmission electron microscopy (TEM) was conducted using JEM-2100F or FEI Titan-3 80–300 microscope. TEM samples were prepared by sonicating catalyst nanopowder in ethanol for 5 minutes. One drop of the solution was then placed onto a 200 mesh copper grid coated with lacey carbon support film (Ted Pella Inc.) and dried in air. Conductivity was measured using a Russel RL060C Portable Conductivity Meter (Thermo Scientific, USA). Solubility was determined by adding small amounts of $TBAPF_6$ to a small volume of each solvent and manually mixing until failure to dissolve.

3.2.3. Electrochemical Characterization

A three-electrode cell set-up with ~60 mL of electrolyte was utilized. The electrochemical cell body consisted of a small-volume quartz glass cell (Pine Research, USA). The reference electrode consisted of an Ag/Ag^+ non-aqueous pseudo-reference electrode (ALS Co., Japan), filled with 0.1 M $TBAPF_6$, 10mM $AgNO_3$ in ACN. For the counter electrode a Pt mesh was used (ALS Co., Japan). The working electrode consisted of 2 μL of particle catalyst ink deposited on an L-shaped glassy carbon electrode (3mm diameter, DEK Research). An image of the assembled electrochemical cell is presented in the Supporting Information Figure B.1. The catalyst ink was prepared with 6 mg of particle powder, 1 mL of deionized water (18 MΩ), 200 μL of isopropanol and 100 μL of Nafion® (~5%, Sigma Aldrich, USA) mixed by sonication for approximately 5 minutes. Prior to deposition, the working electrode surface was polished with 30 μm and 5 μm alumina, rinsed with ethanol and then deionized water. For the reference electrode calibration, the Ag/Ag^+ non-aqueous reference electrode was calibrated against the redox half potential of ferrocene. 5mM ferrocene was included in the electrolyte solution as internal reference, and the reference electrode was calibrated before every new catalyst deposition run. Details pertaining the calibration procedure are depicted in the Supporting Information Figure B.2. CV experiments were conducted from a range between -0.8 V to -1.82 V vs NHE with a step size of 50 mV/s. The cycles were repeated 5 times, and the last cycle was evaluated. The tests were conducted first after 20 min of N_2 purge and again after 15 min of CO_2 purge. The CA tests were conducted with a held potential of -1.7 V vs NHE for 3 hours while maintaining CO_2 purging. After the CA tests another CV trial was conducted at the mentioned conditions under CO_2 purge.

3.2.4. Computational Methods

All detailed procedures of the density functional theory (DFT) calculations are reported in the Supporting Information.

3.3. Results

3.3.1. Electrolyte Properties, Conductivity and Solubility

Select properties for all evaluated solvents are tabulated in Table 3.1. It can be observed that the dinitrile structures possess higher boiling points to water and ACN. Additionally, dinitriles demonstrate lower flammability to ACN with higher flash points. A decreasing dielectric constant trend can also be observed going from water to the nitrile structures and furthermore with the addition of a secondary nitrile group, as well as with lengthening of the dinitrile chain. This relationship is indicative that polarity can be suppressed by utilization of long-chain dinitrile groups. Meanwhile, viscosity demonstrates an increase going from ACN to the ADN dinitrile structure and further increase with lengthening of the dinitrile chain with SBN.

Table 3.1: Electrolyte properties of water and evaluated nitrile solvents[8].

Electrolyte	Structure	ε	η (cP)	T_m (℃)	T_b (℃)	T_f (℃)	T_{auto} (℃)
Water	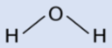	80[9]	1	0	100	-	-
Acetonitrile	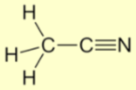	37	0.3	-48	81	2	523
Adiponitrile	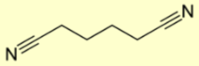	30	6.1	1	295	163	550
Sebaconitrile	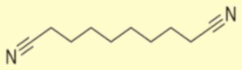	22	10.7	8	200	>113	-

ε=dielectric constant, η = dynamic viscosity T_m = melting point temperature, T_b = boiling point temperature, T_f = flash point temperature, T_{auto} = auto ignition temperature

Due to the utilization of $TBAPF_6$, a polar salt, for the electrolyte, solubility was expected to decrease along with decreasing solvent polarity. The decreasing solubility trend followed the expected decreasing polarity of the solvents, with salt solubility limit values of > 2.5 M, 1.0 M and 0.4 M for ACN, ADN, and SBN respectively. Conductivity measurements with response to salt concentration were also evaluated, plotted in Figure 3.1a. The conductivity increased with concentration before the 1M concentration for all solvents. However, at the 1M concentration point, the conductivity of ADN plateaued at its solubility limit, while that of ACN reached a peak and began to decrease afterwards. As conductivity is related to ionic mobility, and the solvents have increasingly hindered mobility of ions from increasing viscosity from ACN < ADN < SBN, the results were expected to decrease proportionally. Figure 3.1b displays the conductivity results for 0.1 M TBAPF$_6$ concentration in all solvents, as well as the corresponding solvent dielectric constants and viscosity. A proportional trend in terms of dielectric constant and conductivity is seen. In addition, an inversely proportional trend of the conductivity and the viscosity is apparent. The conductivity for the 0.1 M concentrations were of 9.43, 0.73 and 0.28 mS, for ACN, ADN and SBN respectively.

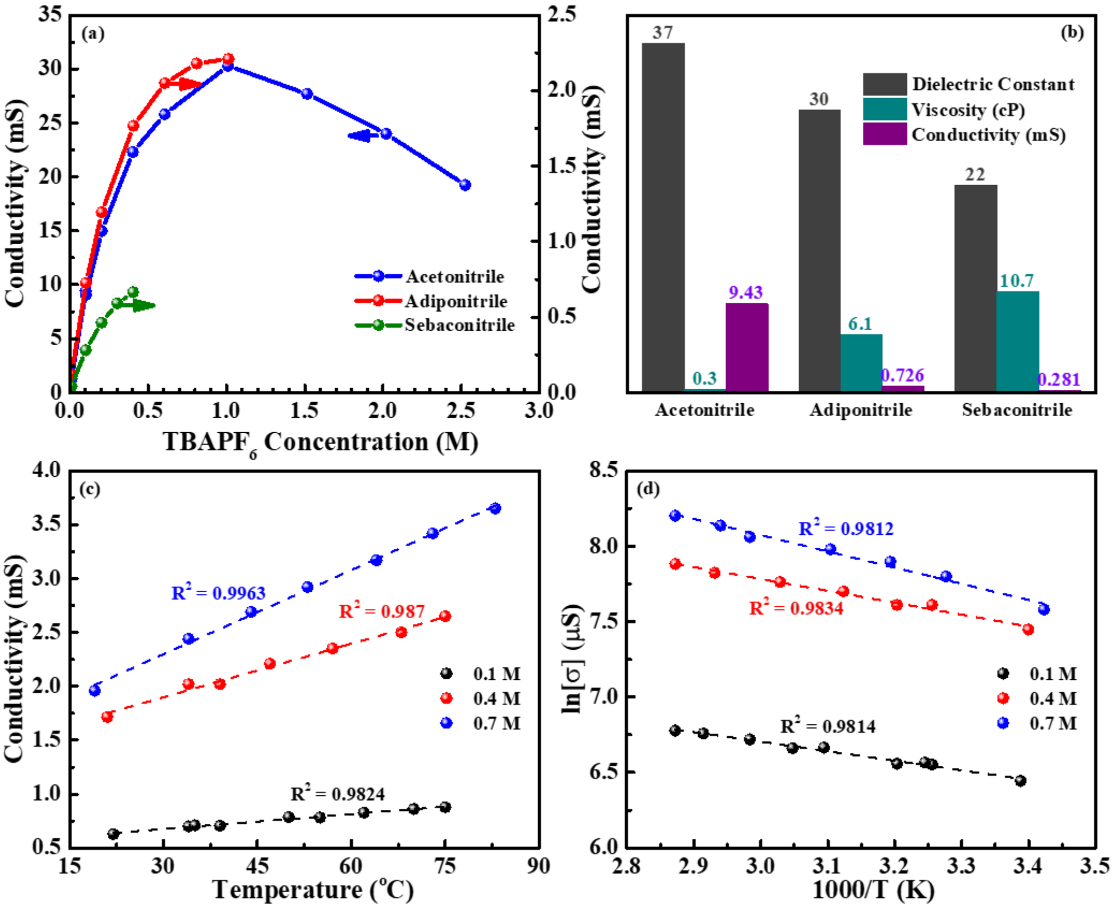

Figure 3.1: Behaviour of (a) electrolyte conductivity versus TBAPF$_6$ concentration, (b) dielectric constant and viscosity relationship with 0.1 M electrolyte conductivity for electrolyte solvents ACN, ADN, and SBN. Behaviour of (c) conductivity versus temperature and (d) linearized Arrhenius plot derived from the conductivity versus temperature data for adiponitrile at different TBAPF$_6$ concentrations

Conductivity with respect to temperature variation between 20 and 80 °C is shown in Figure 3.1c for ADN for 0.1, 0.4 and 0.7 M $TBAPF_6$ concentrations. It was observed that with increasing temperature, conductivity rises, as ionic mobility is increased. With increasing concentration, conductivity rose proportionally following the trend observed in Figure 3.1a. As such, through the combined effect, the slope trend with increasing concentration rose. Figure 3.1d shows the data translated into a linearized Arrhenius plot. The derived activation energies and pre-exponential factors were able to be determined from the linearized data. The activation energies resulted in 5.27, 6.55 and 8.93 kJ/mol for the 0.1, 0.4 and 0.7 M concentrations respectively. The determined pre-exponential factors were of 5.45, 25.52 and 80.19 mS with 0.1, 0.4 and 0.7 M concentrations respectively.

3.3.2. CO_2 Solubility in Electrolytic Solvents

The CO_2 solubility in the electrolytic solvents was evaluated through quantified FTIR spectra. The dissolved CO_2 presented a peak at ~2340 - 2350 cm^{-1}, which at the same range no peak was observed previous to the purging of CO_2 into the solvents. The effect of CO_2 peak growth over CO_2 purging time can be observed in Figure 3.2a-d for all evaluated solvents. Water displayed the smallest maximum CO_2 peak with an absorbance peak approximately of 0.1 when the background without purging is subtracted. Meanwhile, ACN displayed a maximum absorbance peak of ~0.2, with also a visibly broader peak. Then, the dinitriles, SBN and ADN, displayed maximum absorbances of ~0.38 And 0.5 respectively. The result of the normalized integrated areas (Supporting Information, Figure B.3 and Figure B.4 along with Tables B.1-3) were proportional to the observed absorbance trends with values of 0.002, 0.005, 0.010 and 0.009 cm^{-1} for water, ACN, ADN and SBN, respectively. The determined CO_2 solubility concentration values were of 40[5], 270[5], 582 and 503 mM.

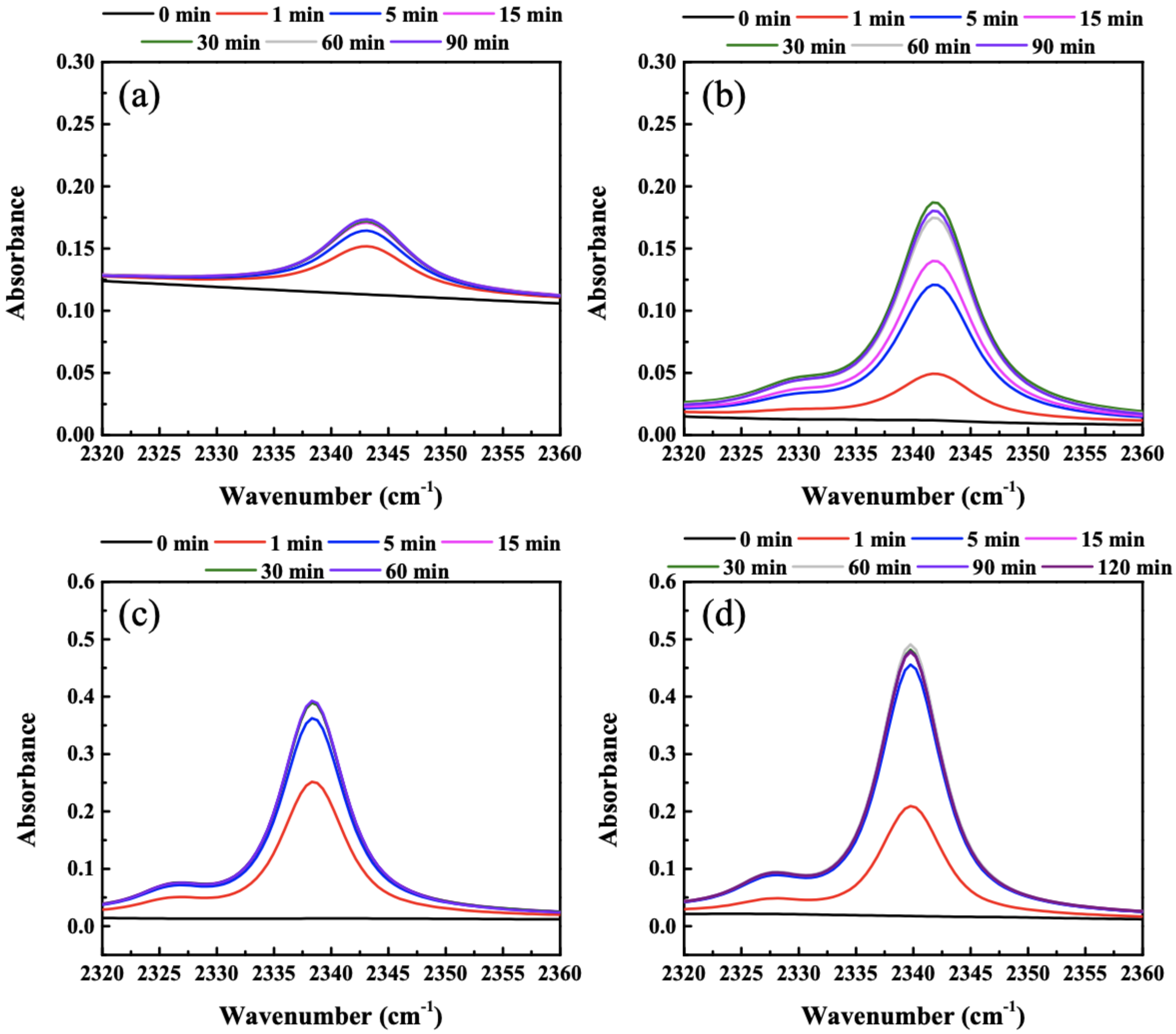

Figure 3.2: FTIR CO_2 peak spectrum evolution over CO_2 purge times for (a) water, (b) acetonitrile, (c) sebaconitrile, and (d) adiponitrile.

3.3.3. Electrochemical Results

Depicted in Figure B.5 are the activities in relation to the potentials under N_2 purge for CuO commercial (CuO NPs) and Cu commercial (Cu NPs). The detailed information of TEM and XRD characterizations for the catalysts are shown in the Supporting Information (Figure B.6 and Figure B.7). Under N_2 purge conditions the measured currents are mainly attributed to the competing hydrogen evolution reaction (HER). In Figure B.5a and b a comparison between aqueous and the nitrile electrolytes of interest are compared. The maximum current densities decrease from -2.8 and -3.5 mA cm^{-2} in aqueous electrolyte using CuO and Cu nanoparticles respectively, to values at or below -0.4 mA cm^{-2} in organic electrolytes. Notably, a direct quantified comparison cannot be made as the potentials are shifted, as CO_2 reduction occurs at a greater potential for organic electrolytes due to the unavailability of H^+ ions[5,6]. However, it can still be observed that a suppression of the HER is occurring from aqueous to organic solvent electrolytes. In Figure B.5c and d the current density differences under N_2 purge in ACN, ADN and SBN electrolytes are observed in more detail for both Cu and CuO NPs respectively. The maximum current densities displayed for the CuO catalyst were of -0.4, -0.33 and -0.05 mA cm^{-2} for ACN, ADN and SBN respectively. For the Cu catalyst the values were of -0.2, -0.31 and -0.08 mA cm^{-2} in corresponding order of ACN, ADN and SBN. Comparatively, a significant deviation is not observed in the activities of ADN and SBN between the two catalysts with only a change between 0.02 and 0.03 mA cm^{-2}. Meanwhile, ACN displayed a decrease in activity of 0.2 mA cm^{-2} going from CuO to Cu catalyst.

Figure 3.3a, b and c display the current densities as a function of potential for both HER and CO_2ER in ACN, ADN, and SBN respectively for both the CuO and Cu commercial nanoparticle catalysts. Figure 3.3d demonstrates a summary of the maximum current densities of the aforementioned CV plots. The difference between the HER and the CO_2ER current densities provide an estimate of the activity of the CO_2ER. The greatest difference between these was observed in the maximum points of the ACN, for both catalysts. In ACN, the current densities increased from -0.2 to -1.4 mA cm^{-2}, and from -0.4 to -1.6 mA cm^{-2} in Cu and CuO respectively. In ADN the observed increase was from -0.31 to -0.53 mA cm^{-2} and -0.33 to -0.54 mA cm^{-2} in Cu and CuO respectively. Finally, in SBN the increases in current densities occurred from -0.05 to -0.16 mA cm^{-2} and -0.08 to -0.14 mA cm^{-2} corresponding to Cu and CuO. As observed in Figure

3.3d, a proportional decreasing trend in the CO_2 activities can be observed from ACN to ADN and then to SBN. This result seemingly follows an inversely proportional relationship to the viscosity values of the nitrile solvents.

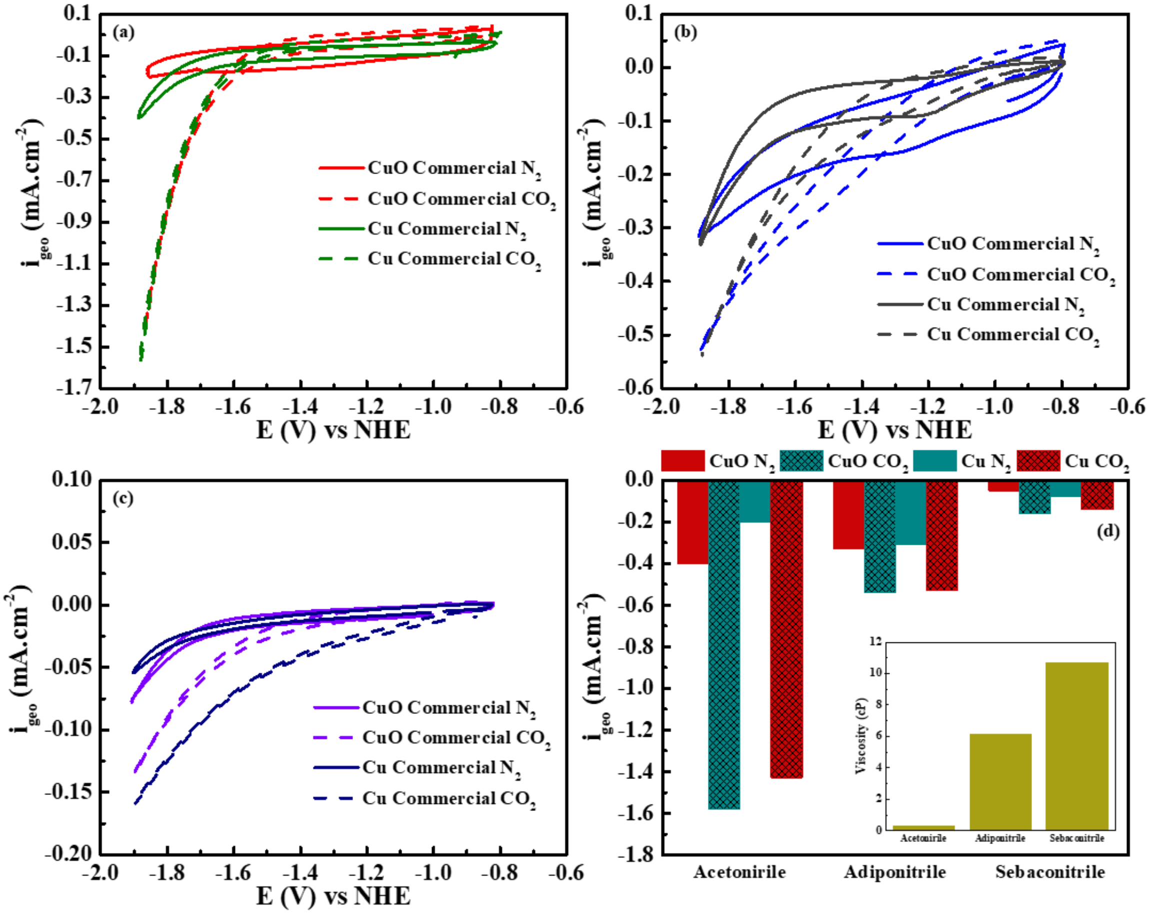

Figure 3.3: Cyclic Voltammograms of CuO and Cu NP catalysts for 0.1 M $TBAPF_6$ in (a) acetonitrile, (b) adiponitrile and (c) sebaconitrile at 50 $mV.s^{-1}$ scan rate (fifth stable cycle). (d) A summary of the maximum current densities of the CVs at -1.82 V vs NHE along with the dynamic viscosity values.

Figure 3.4a and b display the current densities over 3 hours with a held potential at 1.7 vs NHE. It was found that the average current densities were of -0.31 -0.28 and -0.09 mA cm^{-2} for ACN, ADN and SBN respectively utilizing CuO commercial catalyst. Meanwhile, the values for Cu commercial catalyst were found to be of -1.18, -0.16 and -0.04 mA cm^{-2} for ACN, ADN and

SBN respectively. Overall, a current density value trend in the order of ACN > ADN > SBN is again observed for both catalysts. Comparing behavior over time, the SBN trends with both catalysts are fairly stable over the 3 h time period, with CuO having a more negative average current density value. In ADN, relative stability is seen with the Cu catalyst performance. However, with the use of CuO in ADN, the activity is observed to be trending towards higher negative values over time. The increase occurs from -0.15 to -0.35 mA cm^{-2}, observing an increase in the activity by a factor of 2.3 over the three hour period with relative stabilization occurring at the end. Finally, in ACN, the initial trend in the first 60 minutes is unstable for both catalysts. In CuO, a relative stability is observed in the first 50 minutes with a -0.42 mA cm^{-2} current density. However, at the 50 minute mark, a decrease in activity is observed to reach another stability point at -0.24 mA cm^{-2}, decreasing by a factor of 0.57. In Cu, overall better performance is observed with the lowest current density values. The trend is unstable for the first 60 minutes, after which the current density trend is increasing, ending with a value of -1.34 mA cm^{-2} at the 3h mark.

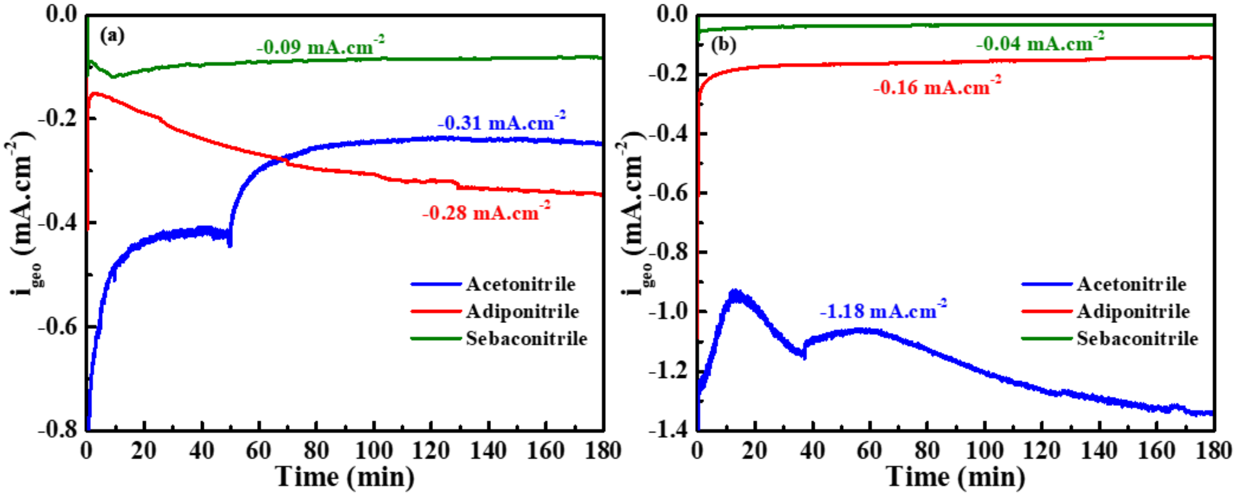

Figure 3.4: Chronoamperometry plots of (a) CuO commercial nanoparticles and (b) Cu commercial nanoparticles at -1.7 vs NHE potential for 3 hours in acetonitrile, adiponitrile and sebaconitrile electrolytes. The average values of the CAs are displayed in the boxes next to the plots.

3.4. Discussion

The basis of this study refers to the hypothesis of increased solubility of CO_2 in organic nitrile solvents with decreasing polarity, expecting a proportional increase in electrochemical performance of CO_2ER as a result. As the dielectric constant is a measure of polarity of a molecule, Table 3.1 shows evidence that the polarity of the solvents is reduced with the addition of a secondary nitrile group going from the mononitrile ACN to ADN and SBN dinitrile structures. This can potentially be explained by the symmetrical addition of an identical polarity end group to both ends of the molecular structure. In addition, with the increase of the dinitrile chain length from ADN to SBN, a further decrease in polarity is observed. As such, the additions of non-polar methylene groups between the two nitrile end groups also seem to further decrease the overall polarity of the structure. Therefore, polarity decreases in the order of ACN > ADN > SBN. In addition, the polar salt solubility decreased from ACN to ADN to SBN, further indicating the expected polarity behaviour.

Conductivity is also an important electrolyte property for the CO_2ER performance, as it affects the ability to transport electrons in the cell. Previous results have shown that the electrolyte can play a role in stabilizing intermediates and the adsorption of CO_2 on the catalytic surface[10]. In Figure 3.1a, the conductivities prior to 1 M $TBAPF_6$ concentration are greater for ACN, decreasing significantly with ADN, and then with a slight decrease with SBN compared to ADN. Notably past the 1 M $TBAPF_6$ concentration, the ACN conductivity was observed to decrease. A potential explanation for this behavior may be due to increased viscosity of the solution with the addition of the salt past the 1 M point. As more available ions are present with each addition, conductivity naturally increases, however if the mobility of the ions is hindered, such as with viscosity, a decrease can begin to occur. This trend also seems indicative of the results observed with regards to conductivity with the other solvents. In Figure 3.1b, an inversely proportional relationship can be seen with regards to viscosity and conductivity at a 0.1 M $TBAPF_6$ concentration. With the addition of the secondary nitrile group going from ACN to ADN, not only does polarity decrease but viscosity significantly increases by 8.85 cP. Meanwhile conductivity decreased by 8.7 mS. A similar trend is seen comparing ADN and SBN, where the viscosity exhibited an increase of 2.64 cP and the conductivity decreased by 0.45 mS.

As viscosity is temperature dependent, the viscosity can be reduced and thus conductivity can be improved through increasing temperature. Temperature variation conductivity studies under different concentrations were ran for ADN. Adiponitrile was selected of interest due to its increased CO_2 solubility, lower cost, and increased availability to the other solvents. In Figure 3.1c evidence of rising conductivity with higher temperatures is observed by rising slope. However, through estimation with the trendline of 0.1 M $TBAPF_6$ concentration, a temperature of approximately 1933 ^{O}C would be required to achieve the 9.43 mS conductivity exhibited by ACN at the same concentration, which is not feasible. Similarly for the concentrations of 0.4 and 0.7 M $TBAPF_6$, the required temperatures would be of 1259 ^{O}C and 975 ^{O}C respectively.

Solubility of CO_2 was expected to increase with decreasing polarity of the electrolyte solvents, as CO_2 is a non-polar molecule. The dielectric constant values in Table 3.1 indicate decreasing polarity in the order of H_2O > ACN > ADN > SBN. The results derived from the saturation peaks in Figure 3.2 determined a CO_2 solubility concentration of 40[5], 270[5], 582 and 503 mM for H_2O, ACN, ADN, and SBN, respectively. The results for all the solvents apart from SBN followed the expected trend. As such, the results indicate that the addition of a secondary nitrile group, increases the CO_2 solubility. Meanwhile, the increase of the chain length of the dinitrile chains, going from ADN to SBN, slightly hinders the CO_2 solubility. A potential theory for the decrease could be attributed to intermolecular interactions. Based on the molecules, the number of nitrile groups per 1 mL of solvent were calculated as 1.15×10^{22}, 1.08×10^{22} and 0.67×10^{22} respective to ACN, ADN and SBN. As such, based on CO_2 solubility decreasing with smaller number of available nitrile groups, this could be indicative of CO_2 possessing an affinity towards these groups rather than methylene groups, which are increasing in availability with chain length. Other possible theories include increased interactions between the molecular chains of the dinitrile groups themselves. This could be based on the chain interactions, as these are increasing going from ADN to SBN, and as a result, hindering availability for CO_2 interactions.

To shed light on these possible scenarios, a preliminary and simplified study of the CO_2 molecule interaction within the nitrile-based molecules was performed at atomistic level as modeled by DFT. All possible CO_2 adsorption sites and molecule configurations were considered for each ACN, ADN and SBN case (see DFT results in the Supporting Information). Our results showed that the CO_2 adsorption is a thermodynamically favorable process, being the most stable on the site of the nitrile groups (see Table B.4 in SI). Figure 3.5 shows only the most stable adsorption configuration and its atomic charge distribution for each case. The most significant geometrical difference in between the dinitrile cases is in the $d_{C_A\text{-}N_1}$ and $d_{O_A\text{-}C_1}$ distances with decreases of about 2.7 % and 0.8 % from the interaction with ADN to SBN, respectively. This could be an indicative that increasing the number of methyl group decreases the CO_2-nitrile interaction distance. Regarding the CO_2 solubility results, a similar trend was displayed by the adsorption energy (E_{ads}) where the most stable E_{ads} values were -0.126 eV, -0.145 eV and -0.141 eV for each ACN, ADN and SBN cases, respectively (a more negative value indicates more stability). For each ACN, ADN and SBN case, all the E_{ads} results showed that the CO_2 preferred to interact with the nitrile groups rather than methyl groups (see Table B.4 in SI). This trend was in line with the idea that the CO_2 solubility results could be, in part, due of the number of nitrile groups per 1 mL of solvent, as aforementioned. It can be seen from charge distribution in Figure 3.5d-f that ACN is the most polar molecule of the three cases. There is no distinguishable difference between the charge distribution of the nitrile groups for the ADN and SBN molecules, which would suggest that there is no appreciable difference in their polarity.

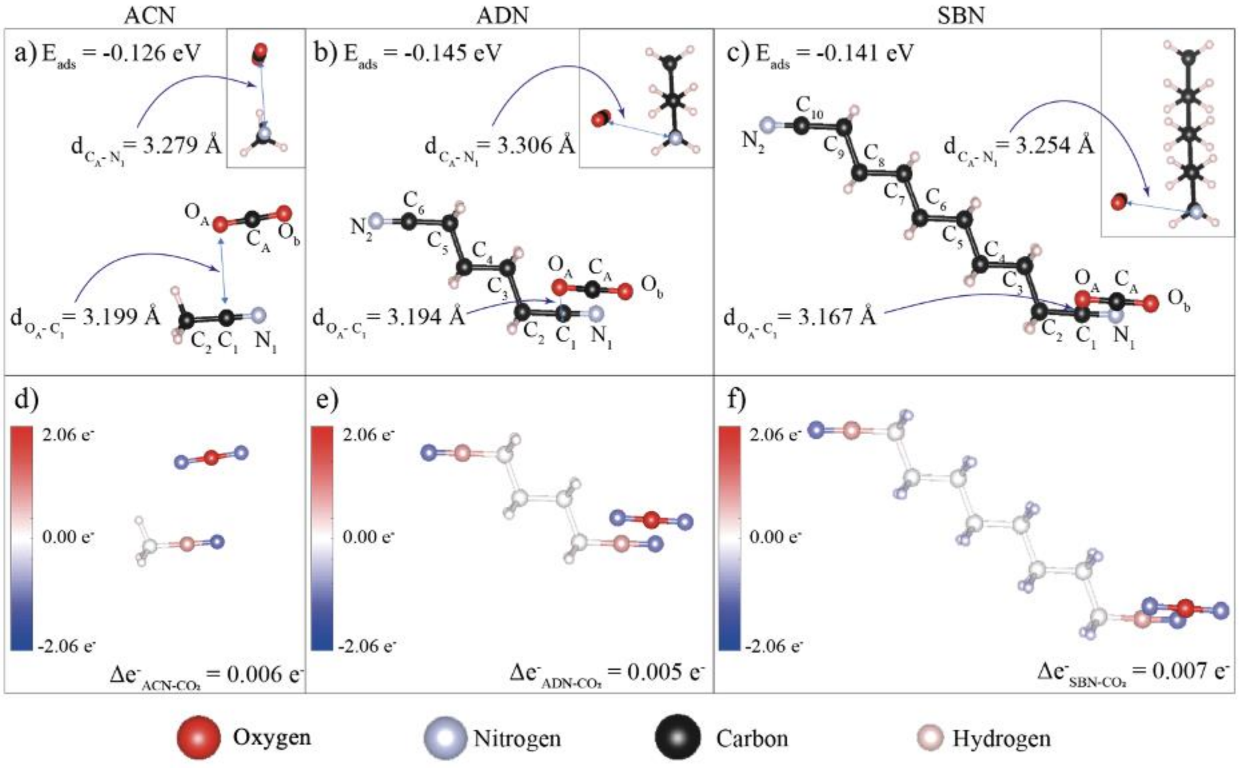

Figure 3.5: ACN, ADN and SBN are depicted from left to right columns, where the top file shows the most favorable adsorption case for a) ACN, b) ADN and c) SBN, respectively, and the bottom file shows the atomic charge transference for d) ACN, e) ADN and f) SBN, respectively. Δe^{-} is the total charge transferred from the nitrile-based molecules to the CO_2 molecule, indicating that the carbon dioxide became slightly more negative.

In good agreement with the E_{ads} results the density of states (DOS) curves for the CO_2 molecule after adsorption showed a shift to lower energies, which is consistent with a stabilization of the system. These results reveal that the adsorption is a favorable process. Also, a small interaction between the molecules appeared in all cases (green arrows on Figure B.8 in SI). In addition to these results, a negligible amount of charge transference from the ACN, ADN and SBN molecules to the CO_2 (a lower amount than 0.01 eV in all cases), could be an indicative of covalent interaction.

In the case of ADN and SBN, a second CO_2 was adsorbed at the remaining nitrile group (see Figure B.9 in SI), showing an E_{ads} value that is exactly two times of the case with only one CO_2. This result showed there is no intramolecular CO_2-CO_2 interaction present, which suggest that only the interaction between the molecules of mono- and di-nitrile solvents could be responsible of this observed trend and have to be taken into account in future studies. The bond order calculations showed a good correlation with the charge transference, electronic structure, and geometrical considerations. These results are consistent with a physisorption process (Table B.5 in SI).

After the preliminary electrolyte findings, the CO_2ER results were then evaluated. Prior to the tests under CO_2 purge, the electrochemical results under N_2 purge were first evaluated, as shown in Figure B.5. These results are attributed mainly to the competing HER reaction activity, as there is no CO_2 introduced. Aqueous results can be relatively compared to the results in the nitrile organic electrolytes in Figure B.5a and b. Notably, the tested potential ranges are greater for the organic electrolyte solutions than the aqueous electrolyte due to the increased potential requirement for the reduction to the CO_2 anion radical rather than the reduction of CO_2 in the available pathways in aqueous media[6]. As such, a direct quantitative comparison is not made. However, the results seem indicative that the HER is suppressed in the organic electrolytes, this is based on a significant decrease of the current. Thus, based on this result, a noticeable HER suppression seems to be indicated based on a lack of H^+ ion availability in the aprotic solvents.

The electrochemical performance under N_2 and CO_2 purge conditions for ACN, ADN and SBN can be observed in Figure 3.3a-d. It was expected that with increasing CO_2 solubility that the electrochemical activity would also increase. However, the results demonstrate a trend going from more to less negative current densities in the order of ACN > AND > SBN with both catalysts used. This trend aligns with the observed behavior in conductivity related to increasing viscosity of the solvents. Therefore, although CO_2 solubility is observed to be increasing from the mononitrile to the dinitrile structures, the electron mobility is hindered going from ACN > ADN > SBN and this effect overshadows any improvements that were expected from increased CO_2 solubility. A test to ensure the purging time of 15 minutes was sufficient to saturate the cell was conducted, where CO_2 purging was extended from 15 minutes to 3 hours (Figure B.10). The results showed that minimal activity change was observed, and thus lack of dissolved CO_2 was not evident.

In addition to CV tests, 3 hour CAs were also conducted to observe the effect on the catalytic performance stability over time (Figure 3.4). CVs conducted before and after the CA studies are also shown in (Figure B.11). Overall, the trend of decreasing activity from ACN > ADN > SBN was again of main observation in both catalysts, supporting again the role of the viscosity effects hindering conductivity and thus performance despite increased CO_2 solubility. The best activity in the Cu catalyst were seen in ACN, with increasing activity over time after the 40 minute mark. For the CuO catalyst the behavior changed, with ACN remaining relatively stable over time with a change at the 50 minute mark after which it stabilized again at a less negative current density. Meanwhile, for CuO, ADN demonstrated increasing activity over time ending with a more negative potential than that of ACN at the 3 hour mark. Although results in SBN remain relatively stable, evidence of increasing activity with CuO catalyst is also observed when comparing the CV results before and post CA measurements (Figure B.11a,c and e). These results point towards the CuO catalyst interactions with the dinitrile solvents showing improving performance over time and decreasing with Cu, which is opposite to the catalyst results in ACN. As such, changes in intermediate stabilization seem to be occurring between Cu and CuO going from mononitrile to dinitrile solvents. Further insights into this theory would need to be evaluated using further modelling of the catalyst surface intermediates and electrolyte interactions. Increases in activity over time may be attributed to re-structuring of the catalyst due to the electrolyte environment, improving interactions on the catalyst surface. However, image characterization techniques to observe the catalytic evolution over time would be required to confirm this in the future. Additionally, product formation may change over time as well, thus product analysis will also be required in the future to understand in more detail the electrolytic effects on the product distribution.

3.5. Conclusion

The results of the $TBAPF_6$ polar salt solubility in the solvents follows proportionally the polarity trend from ACN > ADN > SBN as observed from the dielectric constant values. Meanwhile, decreasing conductivity follows an inverse proportional relationship to the solvent viscosity of ACN < ADN < SBN. The CO_2 solubility results demonstrated an increase in solubility from ACN to ADN, but a decrease with chain length of the dinitrile with SBN. This was indicative that the addition of a nitrile end group improved CO_2 solubility along with the reduced polarity effect. Meanwhile, the increasing chain length effect on CO_2 solubility, indicates the possibility of intermolecular interactions between CO_2 and nitrile groups.

From the electrochemical results, evidence of HER suppression was observed in the organic electrolytes. However, contrary to CO_2 solubility results the CO_2ER activity decreased from ACN to ADN and further with SBN. This trend is inversely proportional to the increasing viscosity from ACN to ADN and to SBN. CA activity results also follow the decreasing trend from ACN > ADN > SBN. Notably, increasing activity was observed with the use of CuO in ADN and SBN over time, with ADN showing more negative current densities compared to ACN. More studies will need to ensue in terms of catalyst intermediate with electrolyte interactions, product distribution, as well as visual characterization over time to further understand the effects on product formation and potential surface restructuring of the catalysts. The preliminary DFT computations, in good agreement with the experimental results, show that the CO_2 adsorption is a thermodynamically favorable process where the preferable interactions occur at the nitrile groups. Also, the adsorption energies trend is similar to the solubility experimental trend. All these results are consistent with electronic structure, charge transfer, bond distance and BO.

Acknowledgements

This research was enabled in part by support provided by the Natural Resources of Canada (NRC) under the Materials for Clean Fuel program (A1-017184) and the Digital Research Alliance of Canada (alliancecan.ca). We also acknowledge Prof. Paula V. Jasen and Prof. Alfredo Juan for their help with DFT calculations discussion.

References

[1] M. K. Birhanu, M. C. Tsai, A. W. Kahsay, C. T. Chen, T. S. Zeleke, K. B. Ibrahim, C. J. Huang, W. N. Su, B. J. Hwang, *Adv. Mater. Interfaces* **2018**, *5*, 1.

[2] A. Vasileff, C. Xu, Y. Jiao, Y. Zheng, S. Z. Qiao, *Chem* **2018**, *4*, 1809.

[3] H.-O. Pörtner, D. C. Roberts, M. Tignor, E. S. Poloczanska, K. Mintenbeck, A. Alegría, M. Craig, S. Langsdorf, S. Löschke, V. Möller, A. Okem, B. Rama, IPCC, 2022: Climate Change 2022: Impacts, Adaptation, and Vulnerability. Contribution of Working Group II to the Sixth Assessment Report of the Intergovernmental Panel on Climate Change.

[4] S. Nitopi, E. Bertheussen, S. B. Scott, X. Liu, A. K. Engstfeld, S. Horch, B. Seger, I. E. L. Stephens, K. Chan, C. Hahn, J. K. Nørskov, T. F. Jaramillo, I. Chorkendorff, *Chem. Rev.* **2019**, *119*, 7610.

[5] M. Moura de Salles Pupo, R. Kortlever, *ChemPhysChem* **2019**, *20*, 2926.

[6] M. König, J. Vaes, E. Klemm, D. Pant, *iScience* **2019**, *19*, 135.

[7] H. Yu, M. N. Obrovac, *J. Electrochem. Soc.* **2019**, *166*, A2467.

[8] H. Duncan, N. Salem, Y. Abu-Lebdeh, *J. Electrochem. Soc.* **2013**, *160*, A838.

[9] H. D. Young, R. A. Freedman, A. L. Ford, *Sears and Zemansky's University Physics: with Modern Physics*, 13th edition, Addison-Wesley.

[10] R. M. Arán-Ais, D. Gao, B. Roldan Cuenya, *Acc. Chem. Res.* **2018**, *51*, 2906.

[11] T. Theivansanthi, M. Alagar, *Arch. Phys. Res.* **2010**, *1*, 112.

[12] R. Raghav, P. Aggarwal, S. Srivastava, *AIP Conf. Proc.* **2016**, *020078*.

[13] V. V. Pavlishchuk, A. W. Addison, *Inorganica Chim. Acta* **2000**, *298,* 97.

Chapter 4. Conclusions and Recommendations

4.1. Summary and Conclusions

The development of effective plasmonic enhanced electrocatalysts was achieved in this work through the use of synthesized Cu-based nanoparticles formed through a straightforward, easily scalable chemical reduction process. Additionally, the plasmonic enhancement was observed with the use of a broad-range white light. These findings bring the field closer to the practical implementation of direct catalytic photo-electrochemistry. Additionally, a better understanding of the effect on dinitrile-based electrolytes on CO_2ER was realized through the testing of acetonitrile, adiponitrile, and sebaconitrile solvent electrolyte properties and electrochemical performance.

In Chapter 2, the demonstration of direct plasmonic CO_2ER was observed on Cu, Ag and Cu-Ag bimetallic particles. It was found that different configurations, such as decorated Cu on Ag and Ag-Cu core-shell systems, could be formed with modification of the Cu-Ag loading through a co-reduction wet chemical synthesis. The resulting particles were tested and compared to commercial counterparts. All synthesized particles were confirmed to be favorable catalysts for CO_2ER. In terms of plasmonic promotion, the $Cu_{60}Ag_{40}$ synthesized particles outperformed the other synthesized bimetallic catalysts with an 18% increase in activity when illuminated. However, the CuAg commercial alloy possessed the overall maximum promotion, with a 26% increase. The observed light responses were attributed to plasmonic effects, as the lamp probe observed negligible heating with only ~2^{o}C difference when left on overnight. The improved promotions of the catalysts were attributed to their unique morphologies and increased Ag compositions. Evidence of improved stability with the incorporation of Ag in the Cu-Ag bimetallic systems was also observed in the duration of 3 hour experiments. Additionally, the poor stability of Cu was found to not only affect the electrocatalytic current density, but also decreased the plasmonic promotion over time.

In Chapter 3, the novel role of dinitrile organic solvent electrolytes on CO_2ER performance was evaluated. The use of $TBAPF_6$ salts in ACN, ADN and SBN were studied and tested as electrolyte solutions. The solubility of the polar salts was found to decrease in the order of ACN > ADN > SBN, which was proportional to their decreasing polarities. However, the conductivities of the solutions with the same salt concentrations also decreased from ACN > ADN > SBN. This relationship was found to be inversely proportional with the viscosities of the solvents, which increased from ACN < ADN < SBN. It was expected that CO_2 solubilities would increase based on interactions with the nitrile and methyl groups of the solvents. Evidence of the role of nitrile-CO_2 interactions were observed with increased CO_2 solubility in the dinitrile solvents compared to ACN. However, increasing of the chain length from ADN to SBN observed a negative effect on the CO_2 solubility indicating that increase in the methyl groups and overall decrease in nitrile group availability played a role. These results were confirmed through DFT calculations, displaying favorable CO_2 adsorption to the nitrile structures in the molecules. In terms of CO_2ER it was expected that the activity would increase with improved CO_2 solubility. However, the results displayed that this was not the case, as the increase in viscosity of the dinitrile solvents appeared to hinder the conductivity and overtook any benefit from increased CO_2 concentrations.

4.2. Recommendations

Although the presented work achieved performance promotion through light illumination and studied the effects of use of dinitrile based solvents for CO_2ER, the results were only analyzed in the form of resulting activity of the reaction. Additional work is also required to better understand the role of direct LSPRs on the performance of the reaction, as well as further effects from dinitrile electrolyte solutions. The following recommendations to further build on this work are provided:

1. The evaluation of ECSA for Cu, Ag and Cu-Ag bimetallic systems was briefly explored in this work for Chapter 2 (see additional details in Appendix C). A method involving Pb under-potential deposition (UPD) was utilized, based on the work of Baturina *et al.*[1] for Cu nanoparticles supported on carbon. It was also found that the UPD approach has been utilized for ECSA measurements on Ag[2,3]. As such, the method was able to be expanded for bimetallic systems. Notably, the Pb monolayer stripping peak for Cu and Ag occurs at similar ranges and thus the method is unable to distinguish the individual active surface areas of each metal on the bimetallic systems. It would be beneficial to develop an approach to measure the individual ECSA of each metal on these systems to evaluate the metallic loading roles on the electrochemical performance. Additionally, confirmation that the UPD approach is able to effectively be used on Cu-Ag systems could be conducted by comparing to other ECSA estimation methods, such as double-layer capacitance.
2. The development of a CO_2 flow cell would be beneficial to scale-up the system for further study. It was identified that working at a small scale, with an electrode area of 0.07 cm^2, provides a challenge for the detection of the reduction products. Scaling to a small-scale flow cell of 25 cm^2, should provide sufficient production of gases and liquid products to be able to be detected and analyzed for product selectivity. The flow cell could also integrate the use of a gas diffusion layer (GDL) for the cathode, as it has been shown to be a method to significantly overcome the mass transport limitations associated with low CO_2 solubilities in aqueous electrolytes[4]. Additionally, the flow cell could further explore alternative catalysts at the anode in order to utilize the energy to advance two desired

reactions as opposed to one. In this way, increasing the energy efficiency of the overall system. Of consideration could be the glycerol electro-oxidation reaction, which can selectively form formate at the anode with the use of Ni-based metals[5]. Through combination with a CO_2ER system, it has been shown that the overall cell energy requirement can be lowered[5]. Additionally, the use of more economic anodic materials to Pt would also reduce the overall cost of the system[5].

3. As mentioned in the previous point, the role of selectivity was not evaluated due to the size of the electrode area. However, the effects on product selectivity based on Cu-Ag metallic variations in the bimetallic particles, the induced plasmonic effect and use of dinitrile-based electrolytes would be of benefit to better understand their influences on the reaction, particularly for the role in C_{2+} product formation. The analysis of products can be conducted through high-performance liquid chromatography (HPLC) and gas chromatography (GC) technologies. Additionally, *in situ* polarization modulation infrared reflection absorption spectroscopy (PM-IRRAS) could be utilized in order to detect the formation of adsorbed intermediates and products on the surface of the electrode[6]. This approach would provide insights into the mechanisms of product formation, which would be beneficial in the case of plasmonic enhanced CO_2ER as it is stipulated that plasmonic effects can unlock new mechanisms. This would also benefit the understanding of the reduction mechanisms at play in the dinitrile solvents.
4. Despite seeing relative success with the synthesized CuAg nanoparticles for plasmonic CO_2ER, improvements to the synthesis method can be conducted. Using sodium borohydride reduction syntheses, changes in the added concentrations of PEG and $NaBH_4$ have been found to play a role in size distribution of Cu particles[7,8]. Additionally, the role

of the pH has also been found to influence the size[7]. The synthesis method was used for Ag with relative success without the addition of the ascorbic acid and NaOH step. However, relatively large particles, which had lower CO_2ER activity to the Ag commercial counterparts was exhibited. It would be beneficial to further explore the role of the different synthesis additions on Cu, Ag and Cu-Ag bimetallic systems. In this way better control of the Ag size distribution could be achieved. Additionally reduced agglomeration of the overall particles would be beneficial to observe if changes occur in terms of plasmonic CO_2ER performance. Finally, reduced oxidation of the Cu could potentially be achieved, which could also benefit its plasmonic response.

5. Alternatively, to Cu-Ag systems other metals and metallic Cu-based combinations could be studied for the role of plasmonic CO_2ER. As previously mentioned, Au is another highly plasmonic material, as such integration of Cu-Au or Cu-Ag-Au systems could be explored to observe their role in terms of plasmonic response. Another identified material of interest that is of low cost is aluminum (Al), as it also exhibits strong LSPR in the visible spectrum. In addition to its plasmonic properties, it has been identified that Cu-Al systems for CO_2ER can achieve high selectivity towards C_{2+} products, particularly ethylene[9]. Cu-Al catalysts have been scarce for the study of CO_2ER and possess favorable promise towards plasmonic-enhanced CO_2ER.
6. In Chapter 2, the light enhanced performances of CO_2ER were attributed to plasmonic effects based on negligible heat effects from the lamp probe. Notably, further testing to confirm and understand the role of the plasmonic effects are required. Temperature studies can be conducted by varying the electrolyte temperature in order to observe how the plasmonic enhancements compares to temperature increases of the reaction

environment[10]. Additionally, further insights into the LSPR peak occurrences based on the light wavelength of the Cu, Ag, and Cu-based particles can be detected via UV-VIS Spectroscopy. In this way, by providing a visual of the occurrence of the LSPR peak(s) and shape, a better understanding of the plasmonic response of the particles can be obtained.

References

[1] O. A. Baturina, Q. Lu, M. A. Padilla, L. Xin, W. Li, A. Serov, K. Artyushkova, P. Atanassov, F. Xu, A. Epshteyn, T. Brintlinger, M. Schuette, G. E. Collins, *ACS Catal.* **2014**, *4*, 3682.

[2] C.-H. Chen, H.-L. Yang, H.-R. Chen, C.-L. Lee, *J. Electrochem. Soc.* **2012**, *159*, D507.

[3] V. Bansal, V. Li, A. P. O'Mullane, S. K. Bhargava, *CrystEngComm* **2010**, *12*, 4280.

[4] O. G. Sánchez, Y. Y. Birdja, M. Bulut, J. Vaes, T. Breugelmans, D. Pant, *Curr. Opin. Green Sustain. Chem.* **2019**, *16*, 47.

[5] M. S. E. Houache, R. Safari, U. O. Nwabara, T. Rafaïdeen, G. A. Botton, P. J. A. Kenis, S. Baranton, C. Coutanceau, E. A. Baranova, *ACS Appl. Energy Mater.* **2020**, *3*, 8725.

[6] M. S. E. Houache, K. Hughes, A. Ahmed, R. Safari, H. Liu, G. A. Botton, E. A. Baranova, *ACS Sustain. Chem. Eng.* **2019**, *7*, 14425.

[7] T. M. D. Dang, T. T. T. Le, E. Fribourg-Blanc, M. C. Dang, *Adv. Nat. Sci. Nanosci. Nanotechnol.* **2011**, *2*.

[8] Q. M. Liu, D. B. Zhou, Y. Yamamoto, R. Ichino, M. Okido, *Trans. Nonferrous Met. Soc. China (English Ed.)* **2012**, *22*, 117.

[9] M. Zhong, K. Tran, Y. Min, C. Wang, Z. Wang, C. T. Dinh, P. De Luna, Z. Yu, A. S. Rasouli, P. Brodersen, S. Sun, O. Voznyy, C. S. Tan, M. Askerka, F. Che, M. Liu, A. Seifitokaldani, Y. Pang, S. C. Lo, A. Ip, Z. Ulissi, E. H. Sargent, *Nature* **2020**, *581*, 178.

[10] Z. Hirbodvash, O. Krupin, H. Northfield, A. Olivieri, E. A. Baranova, P. Berini, *Sci. Adv.* **2022**, *8*, 1.

Appendix A. Supplementary Information for Chapter 2

A.1. Electrochemical Cell

Figure A.1a and b present the electrochemical set up as described in the experimental section. The alignment and proximity of the light with the catalyst surface can be observed in Figure A.1b.

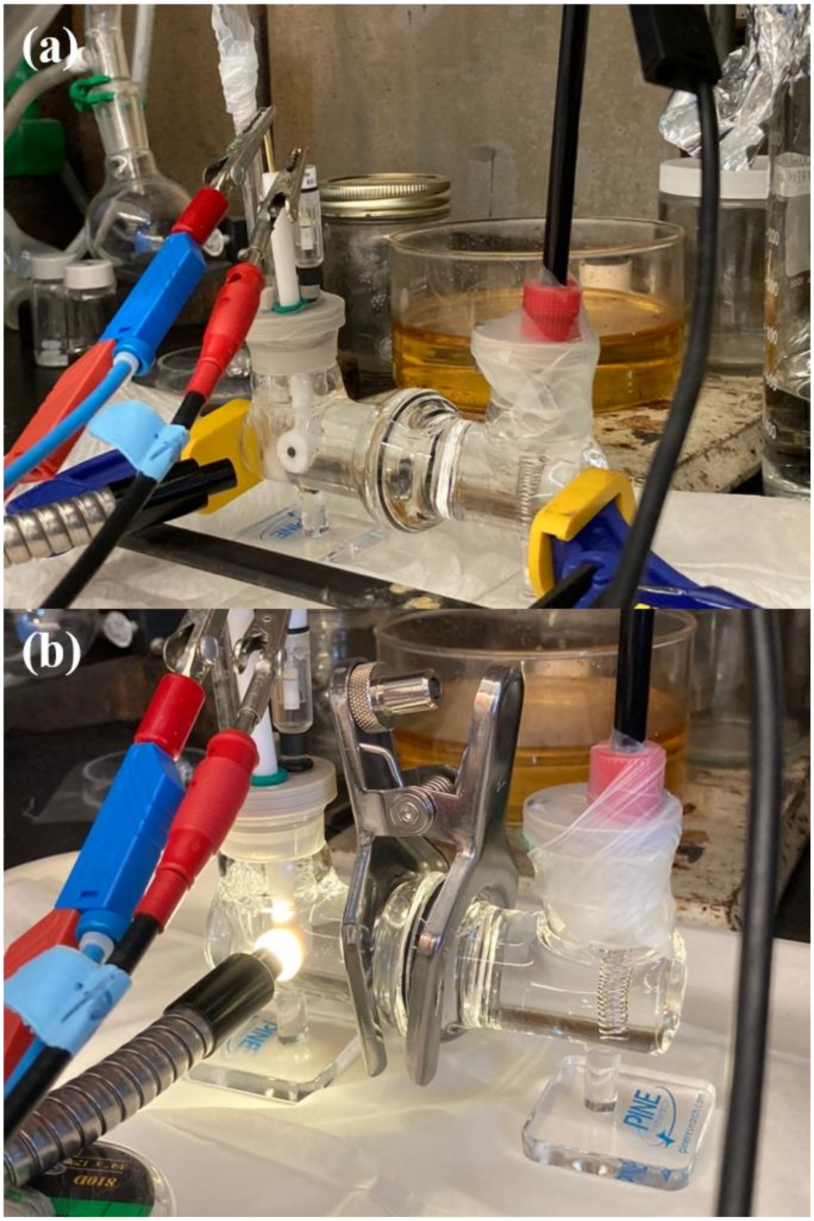

Figure A.1: Images of electrochemical cell set up (a) without light and (b) with light.

A.2. CV Measurements Additional Plots

The CV measurements for the commercial catalysts are presented in Figure A.2a-d. In each plot three measurements are observed. The measurements under N_2 purge is attributed to activity effects of the HER. The other two are under CO_2 purge conditions, where first a light off was conducted (CO_2 light off), followed by a measurement with the light on. It can be observed that maximum current density differences between HER and CO_2 purge are observed in the Ag commercial and CuAg commercial alloy. Small evidence of light promotion in the activity is seen in the Ag commercial. Meanwhile, some decrease of the onset potential is observed in the CuAg commercial alloy. Both the Cu commercial and CuO commercial do not show evidence of CO_2ER, however small observations of light promotion are displayed.

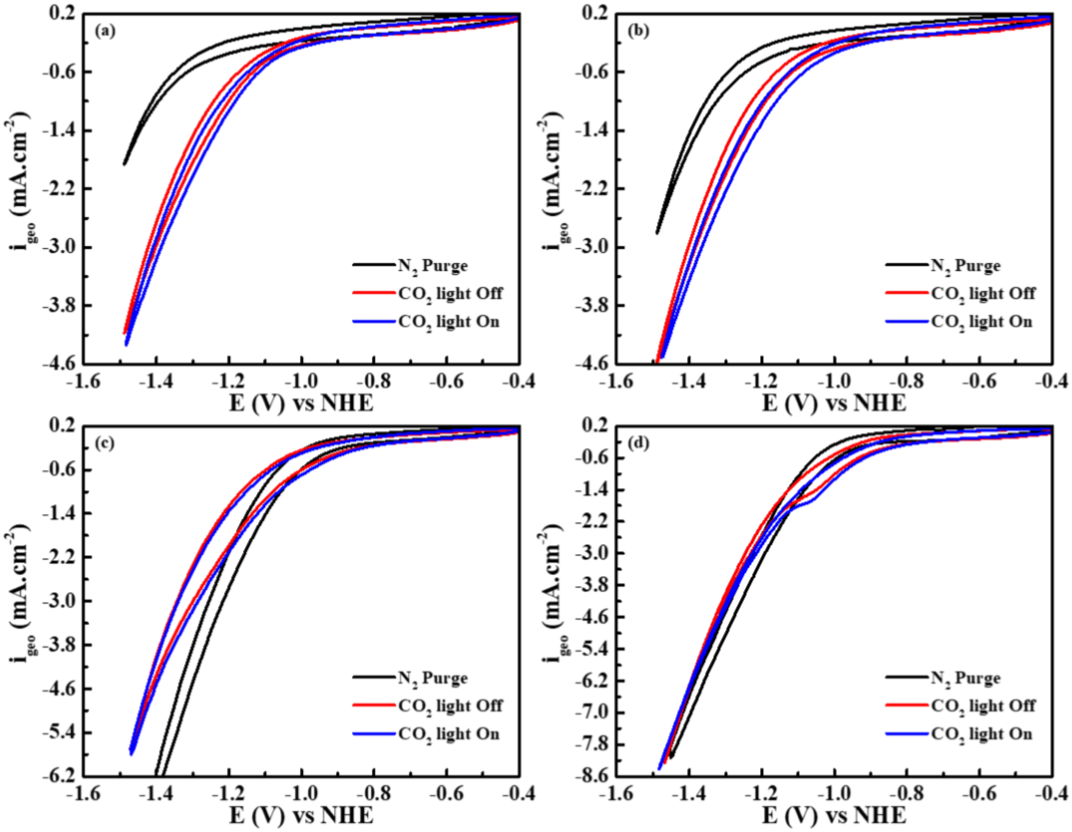

Figure A.2: CV plots of (a) Ag commercial, (b) CuAg commercial alloy, (c) Cu commercial, and (d) CuO commercial under N_2 purge and CO_2 purge at 50 mV.s^{-1} scan rate (fifth stable cycle).

A summarized table of the maximum current density values if provided in Table A.1. Along with the calculated differences in the current density between the initial light-off CO_2 and N_2 purge conditions.

Table A.1: Maximum current density values at -2.15 V vs $Hg/HgSO_4$ of all evaluated particles under N_2 and CO_2 purges, as well as the calculated difference in current density between the CO_2 and N_2 purges.

	i_{geo}, mA cm^{-2}		
Nanoparticle Catalyst	**N_2 Purge**	**CO_2 Purge Light Off**	**Difference**
Ag Synthesis	-2.20	-3.04	-0.84
Ag Commercial	-1.73	-4.65	-2.92
$Cu_{50}Ag_{50}$	-4.27	-5.48	-1.21
$Cu_{60}Ag_{40}$	-3.00	-5.35	-2.34
$Cu_{75}Ag_{25}$	-3.60	-5.23	-1.63
$Cu_{85}Ag_{15}$	-3.46	-5.97	-2.51
CuAg Commercial	-2.85	-4.67	-1.82
Cu Synthesis	-5.00	-6.82	-1.83
Cu Commercial	-8.93	-6.35	2.57
CuO Commercial	-8.98	-9.04	-0.06

A.3. XPS Additional Data

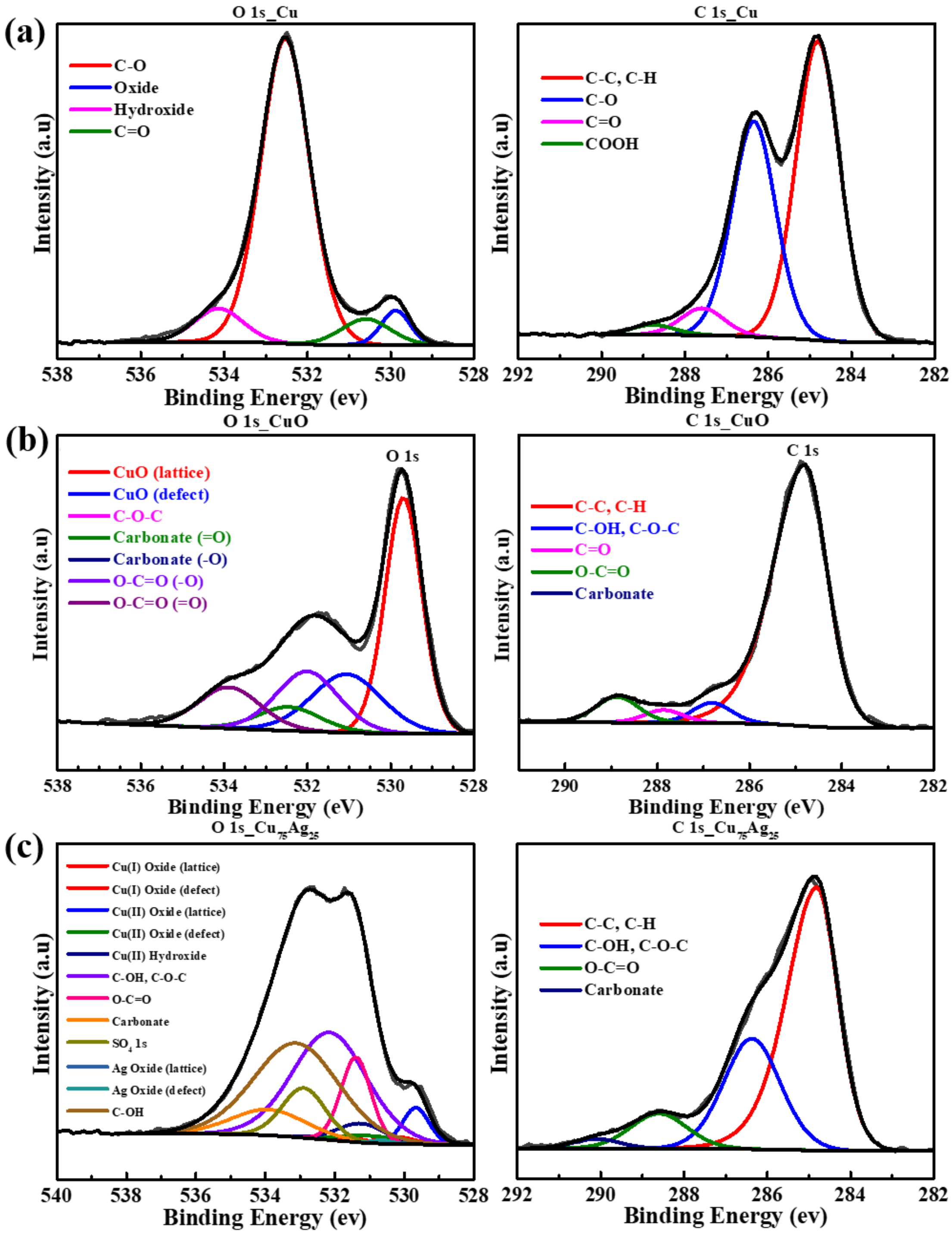

Figure A.3: *XPS spectra of (a) Cu, (b) CuO and (c) $Cu_{75}Ag_{25}$ nanoparticles used in our studies with peak fittings assigned to functional groups. Results of the peak fittings are listed in Table A.2.*

Table A.2: Results of peak fittings to XPS spectra shown in Figure 4 and S3 for Cu, CuO and Cu$_{75}$Ag$_{25}$ nanoparticles.

Cu Commercial							
Peaks in Figure 4a (Cu2p$_{3/2}$)				**Peaks in Figure 4a (Cu LMM)**			
Name	**Position**	**FWHM**	**%Area**	**Name**	**Position**	**FWHM**	**%Area**
Cu(I)	931.99	1.07	72.69	Cu(0)-I	565.34	1.29	0.79
Cu(II)	932.93	2.3	23.31	Cu(0)-II	566.99	1.1	0.61
Cu shakeup	943.41	0.35	0.32	Cu(0)-III	568.05	0.85	1.39
Cu shakeup	944.12	2.67	3.68	Cu(0)-IV	568.6	2.33	1.76
				Cu(0)-V	570.49	1.11	0.36
				Cu(0)-VI	572.43	2.77	1.09
				Cu(0)-VII	575.75	1.43	0.06
				Cu(I) Oxide-I	564.94	2.19	1.87
				Cu(I) Oxide-II	568.73	4.12	20.60
				Cu(I) Oxide-III	569.82	1.68	8.61
				Cu(I) Oxide-IV	573.49	4.09	6.37
				Cu(II) Oxide-I	566.76	3.79	0.62
				Cu(II) Oxide-II	568.82	2.35	0.96
				Cu(II) Oxide-III	572.46	4.05	0.74
				Cu(II) Oxide-IV	575.31	2.33	0.07
				Cu(II) Hydroxide-I	566.59	3.43	5.41

				Cu(II) Hydroxide-II	570.18	4.13	37.32
				Cu(II) Hydroxide-III	574.77	4.78	11.36
Peaks in Fig. S3a (O 1s)				**Peaks in Fig. S3a (C 1s)**			
Name	**Position**	**FWHM**	**%Area**	**Name**	**Position**	**FWHM**	**%Area**
C-O	532.53	1.38	79.31	C-C, C-H	284.81	1.24	54.26
Oxide	529.88	0.8	5.25	C-O	286.35	1.24	39.04
Hydroxide	534.13	1.38	8.67	C=O	287.59	1.24	4.88
C=O	530.59	1.38	6.77	COOH	288.78	1.24	1.81
CuO Commercial							
Peaks in Figure 4b (Cu2p$_{3/2}$)				**Peaks in Figure 4b (Cu LMM)**			
Name	**Position**	**FWHM**	**%Area**	**Name**	**Position**	**FWHM**	**%Area**
Cu(II) Oxide-1	933.28	2.08	30.64	Cu(II) Oxide-1	919.93	3.79	26.01
Cu(II) Oxide-2	934.65	3.00	32.65	Cu(II) Oxide-2	917.87	2.14	40.01
Cu(II) Oxide-3	940.69	1.06	2.97	Cu(II) Oxide-3	914.23	4.67	30.98
Cu(II) Oxide-4	941.83	3.6	27.78	Cu(II) Oxide-4	911.38	2.21	3.00
Cu(II) Oxide-5	943.88	1.22	5.96				
Peaks in Fig. S3b (O 1s)				**Peaks in Fig. S3b (C 1s)**			
Name	**Position**	**FWHM**	**%Area**	**Name**	**Position**	**FWHM**	**%Area**
CuO (lattice)	529.69	1.04	41.33	C-C, C-H	284.80	1.15	87.42
CuO (defect)	531.06	1.98	19.44	C-OH, C-O-C	286.82	1.00	4.79
C-O-C	532.70	1.76	0.00	C=O	287.86	1.00	0.86
Carbonate (=O)	532.45	1.76	7.02	O-C=O	288.87	1.09	6.64

Carbonate (-O)	533.92	1.76	0.09	Carbonate	290.74	1.29	0.30
O-C=O (-O)	532.01	1.76	17.69				
O-C=O (=O)	533.88	1.76	12.15				
$Cu_{75}Ag_{25}$							
Peaks in Figure 4c ($Cu2p_{3/2}$)				**Peaks in Figure 4c (Cu LMM)**			
Name	**Position**	**FWHM**	**%Area**	**Name**	**Position**	**FWHM**	**%Area**
Cu(0)	932.63	1.10	0.00	Cu(0)	921.36	1.29	0.00
Cu(I) Oxide	932.13	1.09	8.37	Cu(I) Oxide	921.75	2.19	7.53
Cu(II) Oxide	933.06	2.25	55.10	Cu(II) Oxide	919.93	3.67	56.13
Cu(II) Hydroxide	934.72	3.04	33.27	Cu(II) Hydroxide	920.10	3.31	32.95
Cu-S	932.65	1.3	3.96	Cu(II) sulfate	918.58	4.09	3.4
Peaks in Figure 4c (Ag 3d)				**Peaks in Fig. S3c (O 1s)**			
Name	**Position**	**FWHM**	**%Area**	**Name**	**Position**	**FWHM**	**%Area**
Ag	368.25	1.12	0.00	CuO I (lattice)	530.20	1.24	0.99
Ag_2O	368.55	1.24	38.75	CuO I (defect)	531.57	1.28	0.56
AgO	367.75	1.23	61.25	CuO II (lattice)	529.67	0.89	3.79
				CuO II (defect)	530.98	1.98	1.68
				CuO II Hydroxide	531.24	1.60	3.53
				C-O-C	532.15	2.52	31.48
				O-C=O	531.39	1.01	9.99
				Carbonate	533.91	2.52	7.55
				SO_4 1s	532.89	1.47	8.55

AgO (lattice)	529.75	0.63	0.13
AgO (defect)	530.65	0.63	0.26
C-OH	533.11	2.88	31.48

Peaks in Fig. S3c (C 1s)

Name	**Position**	**FWHM**	**%Area**
C-C, C-H	284.80	1.20	64.34
C-OH, C-O-C	286.37	1.60	27.82
O-C=O	288.60	1.60	8.83
Carbonate	290.10	1.31	2.02

A.4. CA Measurements Additional Plots

The CA measurements for all evaluated catalysts are presented in Figure A.4, wherein the current densities as a function of potential are displayed. It can be observed that the highest current densities are observed in the Cu particles, while those with the lowest current densities are observed in the Ag particles. In the intermediate boundary between these two, rest the current densities of the bimetallic nanoparticles, with their activities increasing with greater Cu loading. Notably, CuO presents relative instability compared to the other particles under this time frame, with decreasing current density over time.

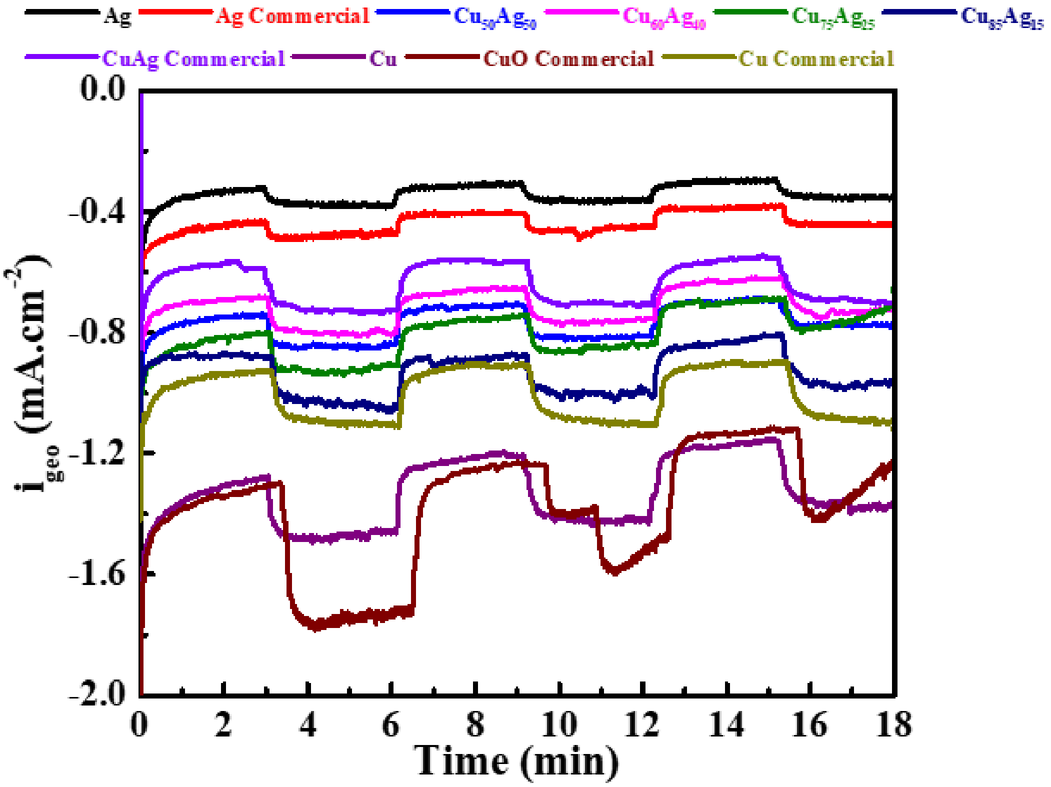

Figure A.4: Chopped light CA plots under maximum light power with constant potential of -1.8 V vs Hg/HgSO$_4$ over 18 minutes for Ag commercial, Cu$_{50}$Ag$_{50}$ synthesis, Cu$_{75}$Ag$_{25}$ synthesis, Cu$_{85}$Ag$_{15}$ synthesis, CuO commercial, and Cu commercial.

Figure A.5a-j present the individual trendlines of the relationship between the average current densities of the CAs shown in Figure A.6 under light off and on conditions over different light powers for all the evaluated particles.

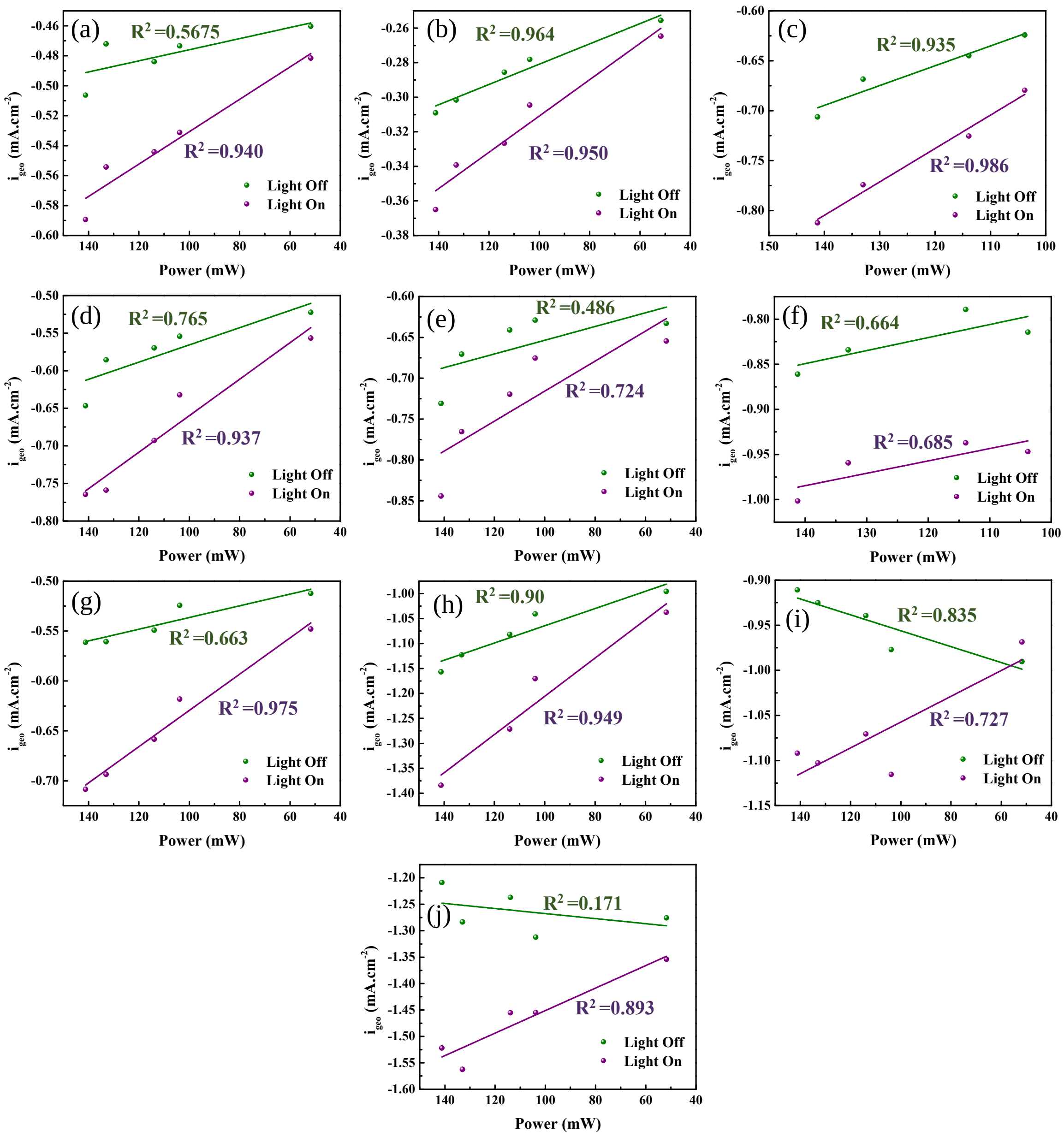

Figure A.5: Average current densities of chopped light CAs at a potential of -1.8 V vs Hg/HgSO$_4$ as a function of power under light off (green) and light on (purple) along with trendlines for (a) Ag commercial, (b) Ag synthesis, (c) Cu$_{50}$Ag$_{50}$ synthesis, (d) Cu$_{60}$Ag$_{40}$ synthesis, (e) Cu$_{75}$Ag$_{25}$ synthesis, (f) Cu$_{85}$Ag$_{15}$ synthesis, (g) CuAg commercial alloy, (h) Cu synthesis, (i) CuO commercial, and (j) Cu commercial.

The chopped light CAs to evaluate the response of current density to light over constant potential under various light powers are shown in Figure A.6 for all evaluated particle catalysts. A flattening of the steps can be observed going from maximum to lower powers. A decrease in current densities with decreasing power can also be observed in some particles, due to the catalytic stability of the particles decreasing over time. The experiments were conducted with maximum power first and lowering the power in correspondingly decreasing orders thereafter.

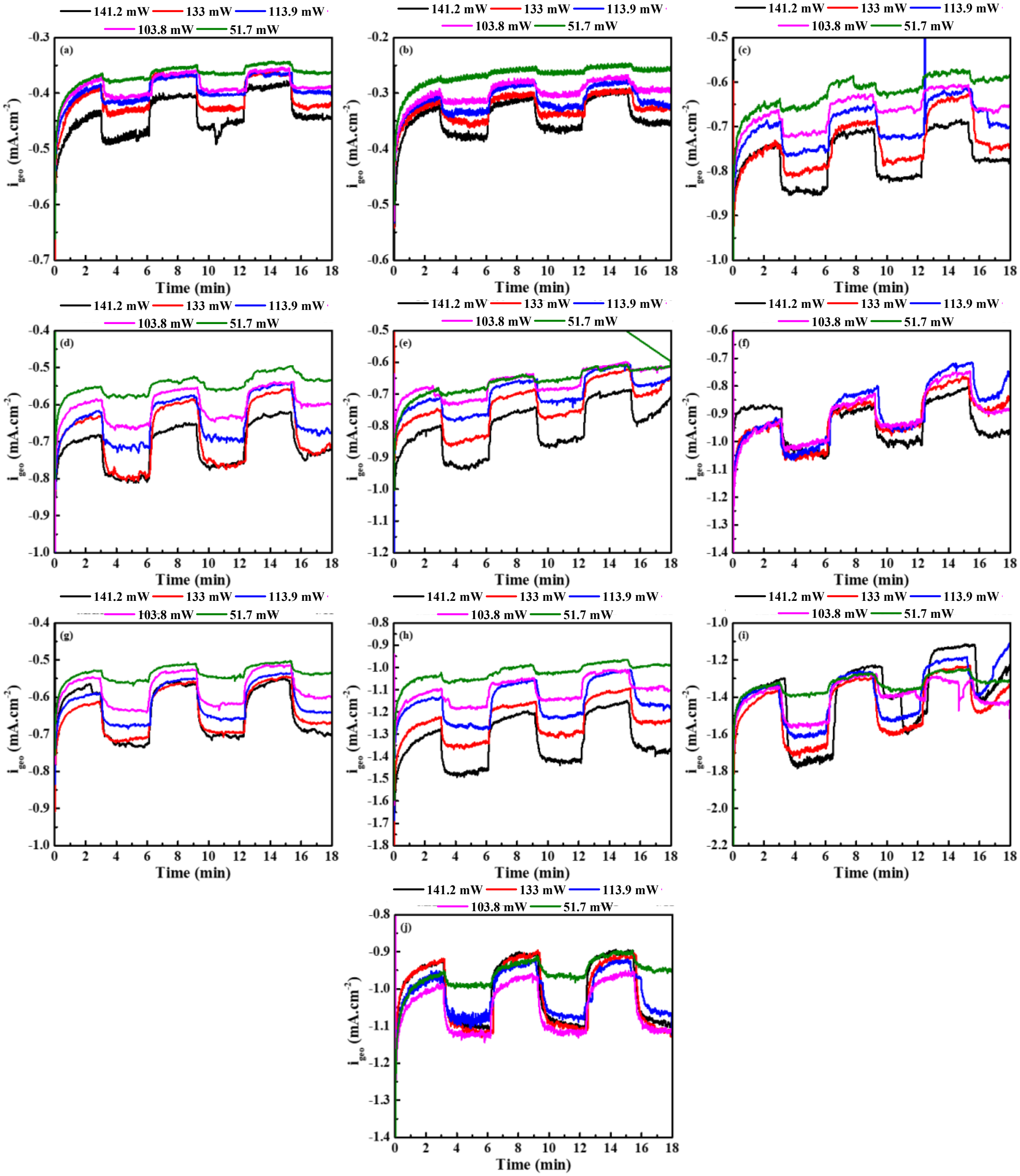

Figure A.6: Chopped light CA plots under different light power conditions with constant potential of -1.8 V vs $Hg/HgSO_4$ over 18 minutes for (a) Ag commercial, (b) Ag synthesis, (c) $Cu_{50}Ag_{50}$ synthesis, (d) $Cu_{60}Ag_{40}$ synthesis, (e) $Cu_{75}Ag_{25}$ synthesis, (f) $Cu_{85}Ag_{15}$ synthesis, (g) CuAg commercial alloy, (h) Cu synthesis, (i) CuO commercial, and (j) Cu commercial.

Appendix B. Supplementary Information for Chapter 3

B.1. Additional Computational Details

The Density Functional Theory (DFT) calculations were implemented by the Vienna Ab-initio Simulation Package (VASP)[1-3]. The general gradient approximation (GGA) parametrized by the Perdew-Burke-Ernzerhof functional (PBE) was used as an exchange-correlation term[4]. The projector augmented wave (PAW) pseudopotential method was used to account for the electron-ion-core interaction[5]. For the plane-wave basis set, a cut-off energy of 520 eV was implemented. The molecules were optimized until the energy convergence was smaller than 10-5 meV and the forces acting on each atom were smaller than 10-3 eV/Å. Spin polarized calculations were considered, with the initial magnetic moment for each atom starting at zero. The van der Waals long-range order interactions phenomena, especially for the carbon-based molecules, were included in the computation as implemented by the DFT-D3 correction method of Grimme *et al.*[6]. A gamma-centered 1x1x1 k-points mesh in the irreducible part of the Brillouin zone was used for reciprocal space integration for all calculated systems, following the Monkhorst-Pack scheme[7]. The ideal gas approximation was used for all molecules. Periodic boundary conditions were implemented in order to maintain a minimum distance of at least 13 Å of vacuum in between periodic images in all directions of each system, even when interacts with a CO_2 molecule, to preclude interaction between interacting molecules and their images. To break the symmetry of the plane wave functions, unit cell parameters of 18.0x17.5x17.0 Å and 23.0x19.0x17.0 Å were considered for the acetonitrile and adiponitrile molecules cases, respectively, which was sufficient to prevent interactions between it and its periodic images as aforementioned. The interaction energy (E_{ads}) is calculated following the equation:

$$E_{ads} = E_{(M+CO_2)} - E_M - E_{CO_2}$$

where M refers to the host acetonitrile or adiponitrile molecules. $E_{(M+CO2)}$,E_M and E_{CO2} are the total energy of the M molecule interacting with the CO_2 molecule, the energy of the isolated M molecule and the energy of the isolated CO_2 molecule, respectively. The final configurations of modeled possible adsorption sites and their corresponding Eads for all considered systems are presented in Table B.4. Where for the ACN molecule, after CO_2 adsorption, four favorable positions surrounding de nitrile group (N-1 to -4) and four surrounding the methyl group (m-1 to -4), for the ADN molecule seven favorable position surrounding de nitrile group (N-1 to -7) and three surrounding the methylene group (m-1 to -3), and for the SBN molecule seven favorable position surrounding de nitrile group (N-1 to -7) and three surrounding the methylene group (m-1 to -2).

B.2. Electrochemical Cell Image

An image of the electrochemical cell is presented in Figure B.1 below. Depicted on the left-hand side of the cell are the glassy carbon gas bubbler, glassy carbon working electrode, and not as apparent, the reference electrode, which was positioned behind the working electrode. On the right-hand side, resides the counter electrode, which consists of a Pt mesh electrode.

Figure B.1: Image of assembled electrochemical cell.

B.3. Reference Electrode Calibration

Figure B.2 displays the resulting ferrocene peak for glassy carbon in the acetonitrile electrolyte as reference for the electrode calibration process. The anodic and cathodic peak potentials occur at approximately 0.013 V and 0.130 V against the Ag/Ag$^+$ reference electrode respectively. Calculating the half wave potential ($E_{1/2}$) using $(E_{pa} + E_{pc})/2$, where E_{pa} and E_{pc} are the peak anodic and cathodic potentials respectively, the obtained value was of 0.071 V vs Ag/Ag$^+$. The half wave potential then serves as a reference in order to be able to convert the measured potential against other types of reference electrodes. As such, utilizing the known $E_{1/2}$ of the Fc/Fc+ couple in acetonitrile is of 0.4 V vs NHE[8], it can be seen that a shift of -0.329 V occurred. As such, to convert vs Ag/Ag$^+$ to NHE, the potential is to be shifted by +0.329 V for the conversion.

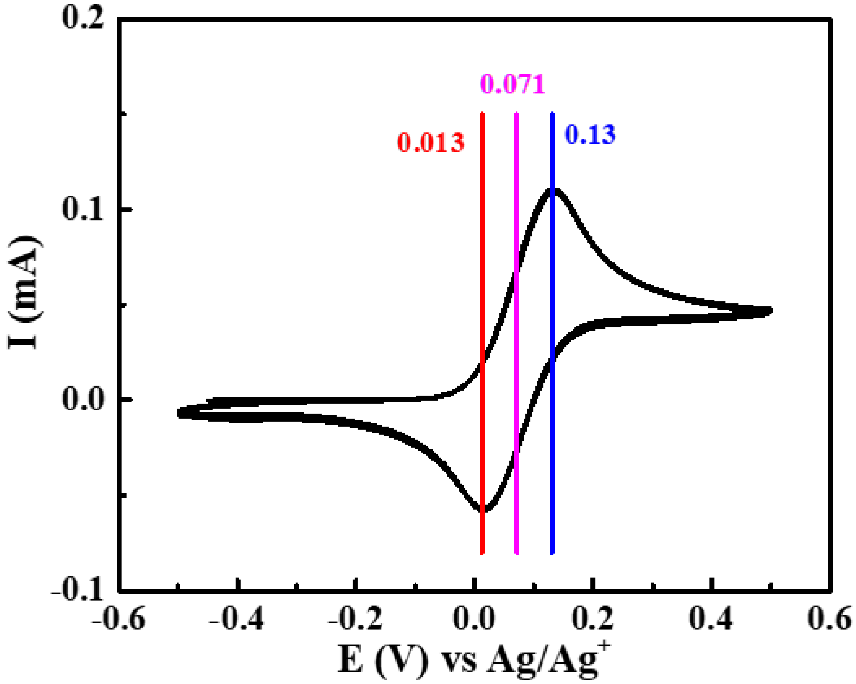

Figure B.2: Ferrocene peaks for glassy carbon in 5mM ferrocene, 0.1M TBAPF$_6$ in acetonitrile.

B.4. FTIR Additional Data

Integration of the FT-IR peaks was conducted using OriginPro$^{@}$ software. The resulting integrated peaks from CO_2 saturation are shown in Figure B.3. Meanwhile, the integrated peaks for the anhydrous ethanol reference are shown in Figure B.4. Tabulated in Table B.1 and Table B.2 are the areas and the average areas with the standard deviation for the CO_2 peaks and ethanol peaks respectively. Table B.3 displays the normalized area of the CO_2 peak over the ethanol reference peak areas, the CO_2 solubility from literature and calculated values, as well as the molar absorptivity. The molar absorptivity value was calculated from the known solubility values of water and acetonitrile. However, for adiponitrile and sebaconitrile the molar absorptivity was estimated to be close to that of acetonitrile. This was then used as a reference to estimate the CO_2 solubility for the two dinitrile solvents.

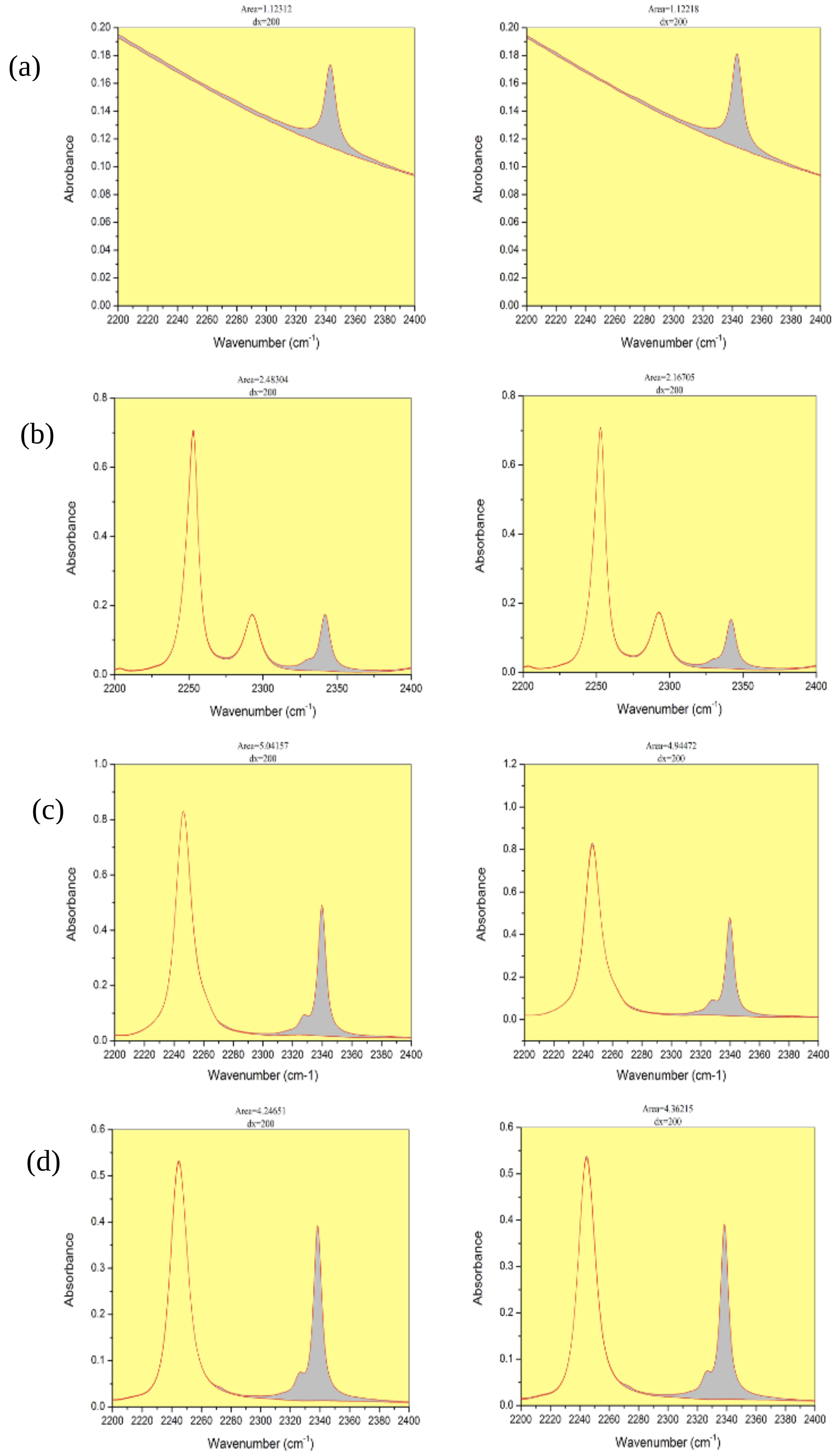

Figure B.3: Integrated FT-IR CO_2 saturation peaks for (a) water, (b) acetonitrile, (c) adiponitrile and (d) sebaconitrile solvents.

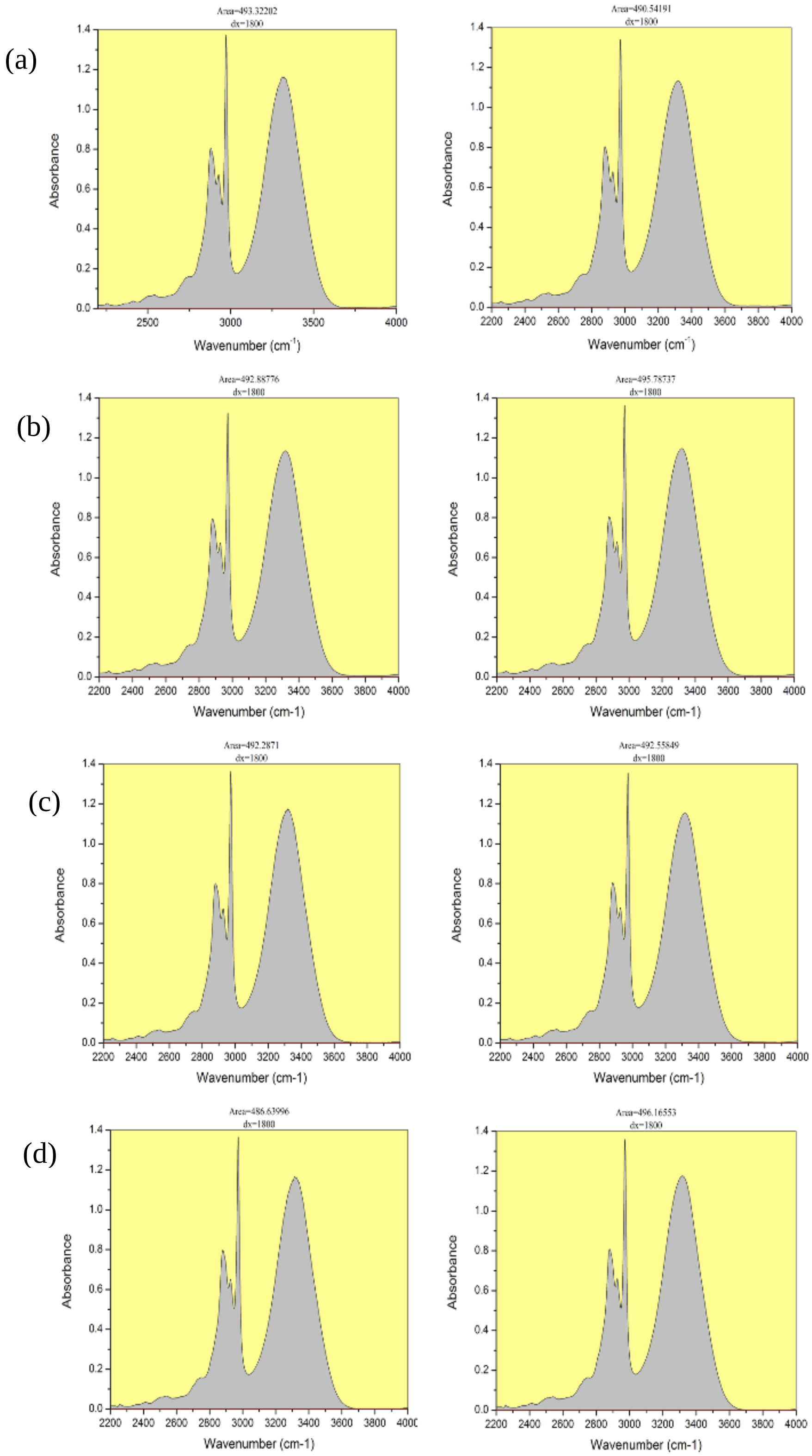

Figure B.4: Integrated FT-IR anhydrous ethanol reference post-sampling (a) water, (b) acetonitrile, (c) adiponitrile and (d) sebaconitrile solvents.

Table B.1: Resulting integrated and average areas from CO_2 peaks of FT-IR CO_2 saturated peaks.

	CO_2 Peak Area 1 (cm^{-1})	CO_2 Peak Area 2 (cm^{-1})	Average CO_2 Peak Area (μ, cm^{-1})	Standard Deviation (σ)
Water	1.12	1.12	1.12	0.001
Acetonitrile	2.48	2.17	2.33	0.223
Adiponitrile	5.04	4.94	4.99	0.068
Sebaconitrile	4.25	4.36	4.30	0.082

Table B.2: Resulting integrated and average areas from anhydrous ethanol reference peaks of post-sampling FT-IR CO_2 saturated peaks.

	Ethanol Peak Area 1 (cm^{-1})	Ethanol Peak Area 2 (cm^{-1})	Average Ethanol Peak Area (μ, cm^{-1})	Standard Deviation (σ)
Water	493.3	490.5	491.9	1.97
Acetonitrile	492.9	495.8	494.3	2.05
Adiponitrile	492.3	492.6	492.4	0.19
Sebaconitrile	486.6	496.2	491.4	6.74

Table B.3: Resulting Normalized CO_2 absorbance areas over ethanol reference areas, literature and estimated CO_2 solubility values, as well as calculated and estimated molar absorptivity values.

	Average CO_2 Peak Area (μ, cm^{-1})	Average Ethanol Peak Area (μ, cm^{-1})	Normalized CO_2 Absorbance Area (-)	CO_2 Solubility (mM)	Molar absorptivity (ε, L mol^{-1} cm^{-1})	
Water	1.12	491.9	0.002	40[9]	5.65E-06	Calc.
Acetonitrile	2.33	494.3	0.005	270[9]	1.72E-06	Calc.
Adiponitrile	4.99	492.4	0.010	582	1.72E-06	Est.
Sebaconitrile	4.30	491.4	0.009	503	1.72E-06	Est.

Calc. = molar absorptivity was calculated using Beer Lambert Formula, Est. = estimated molar absorptivity based on acetonitrile calculated value

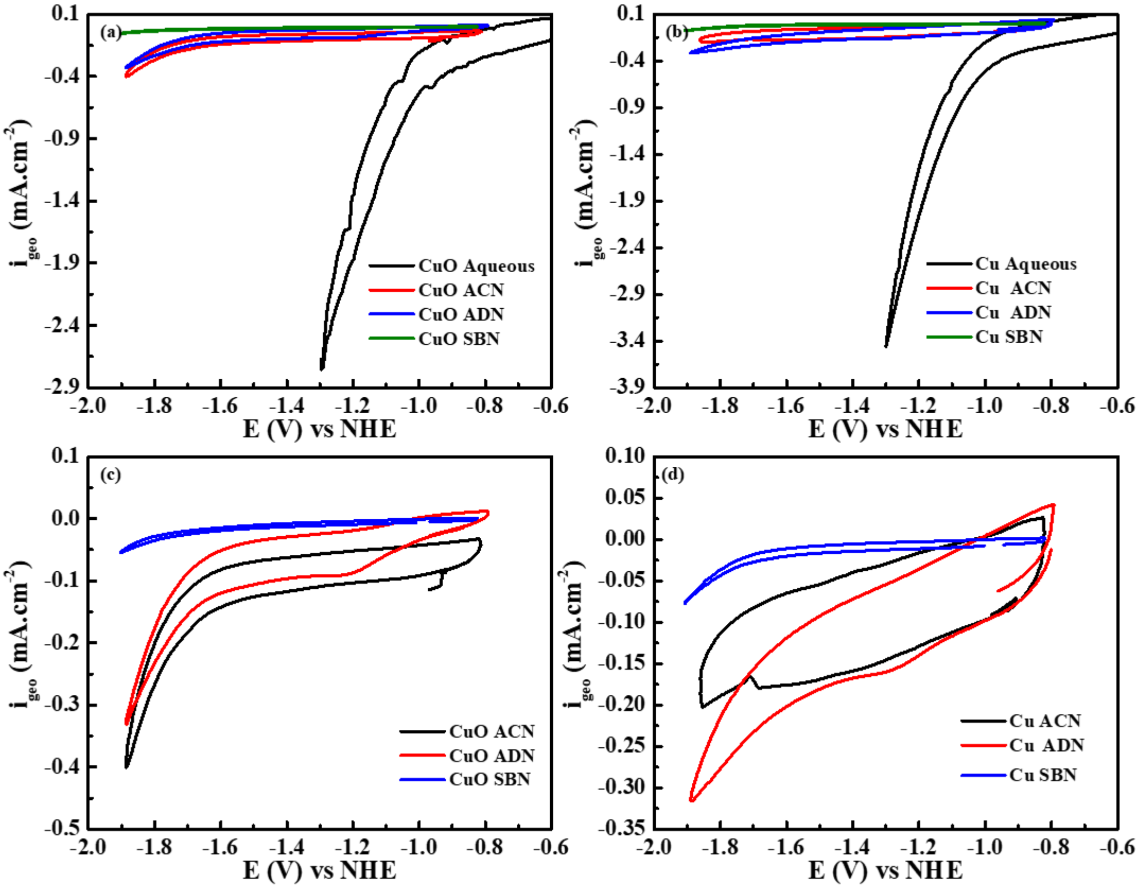

Figure B.5: Cyclic Voltammograms under N_2 purge of (a) CuO commercial and (b) Cu commercial in 0.1 M $KHCO_3$ aqueous, and 0.1 M $TBAPF_6$ acetonitrile, adiponitrile and sebaconitrile electrolytes along with enhanced (c) CuO commercial and (d) Cu commercial in 0.1 M $TBAPF_6$ organic electrolytes at 50 mV.s^{-1} scan rate (fifth stable cycle).

B.5. Commercial Nanoparticle Characterizations

TEM images for the commercial copper particles are displayed in Figure B.6. The commercial copper (Figure B.6a), which was indicated to be 25 nm in TEM displayed this range in size. The CuO (Figure B.6b), were expected to be of 40 nm in size based on manufacturer's indication. Based on the TEM images, the size are more uniform around the 40 nm range.

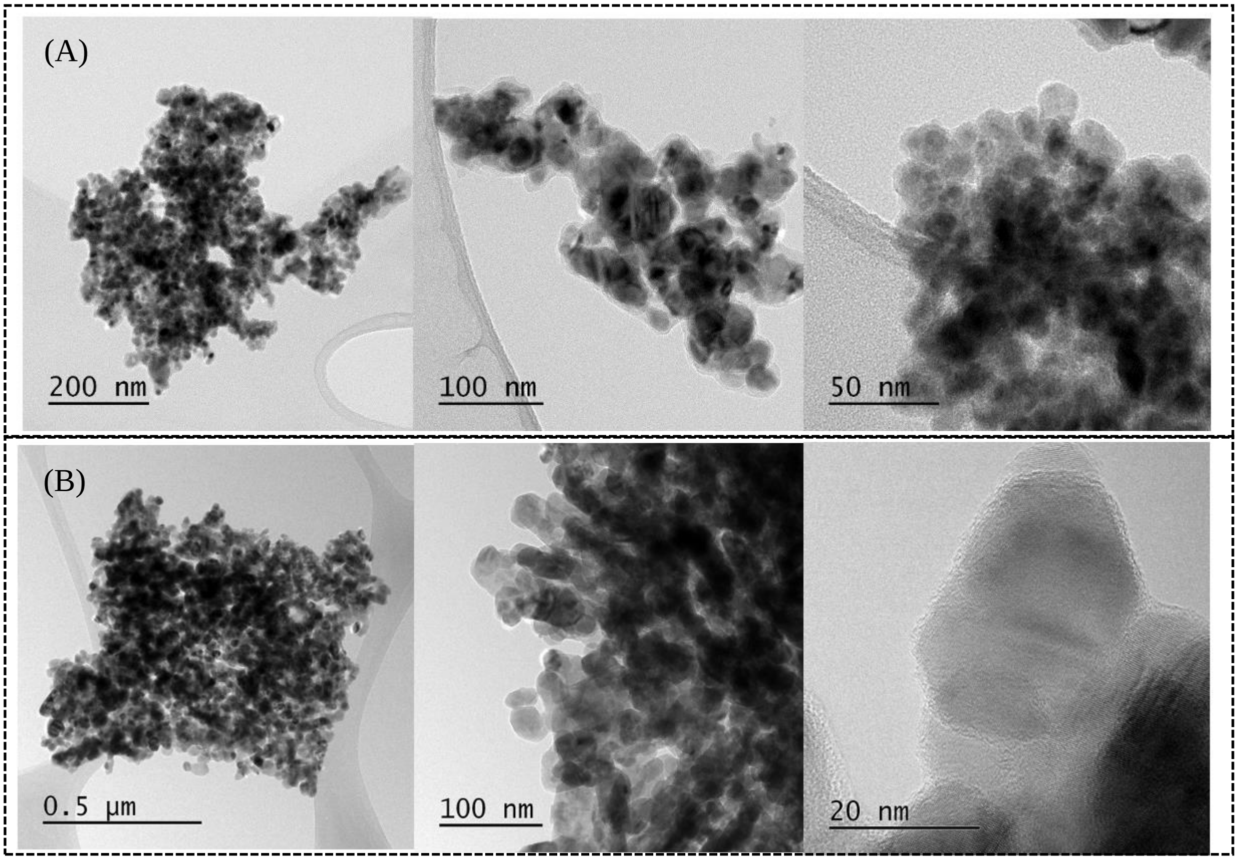

Figure B.6: TEM images for (a) Cu and (b) CuO NPs catalysts.

XRD characterized peaks for the Cu commercial particles are displayed in Figure B.7. The Cu commercial mainly shows significant diffraction peaks at 43.29°, 50.42° and 74.08° which align with the (111), (200) and (220) planes of the face centered cubic (fcc) structure of pure Cu (JCPDS no. 4-836)[10].Two smaller peaks were distinguished at 36.42° and 61.4°, which can be attributed to the (111) and (220) fcc structure planes of Cu_2O (JCPDS no. 5-667)[11] due to slight oxidation. Meanwhile the CuO commercial particles exhibit a monoclinic structure. The main 2θ peaks occurred at 35.46 ° and 38.72 ° attributed to the (-111) and (111) CuO structure planes (JCPDS no. 5-661)[11]. Smaller peaks were also exhibited at 32.47°, 48.78°, 53.46°, 58.23°, 61.54°, 66.25°, 68°, 72.4° and 75.04°. These peaks could be attributed to the (110), (-202), (020), (202), (-113), (-311), (220), (311) and (-222) planes of CuO (JCPDS no. 5-661)[11]. As such, it was confirmed that the main phases for each of the particle catalysts aligned well with their expected Cu and Cu oxide phases. The CuO nanoparticles exhibited no evidence of impurities, while the Cu particles displayed only slight evidence of Cu_2O oxidation beginning to form. The average crystallite sizes (D) estimated from the Debye-Scherrer formula were determined to be of 17.35 and 10.43 for the Cu and CuO commercial nanoparticles, respectively.

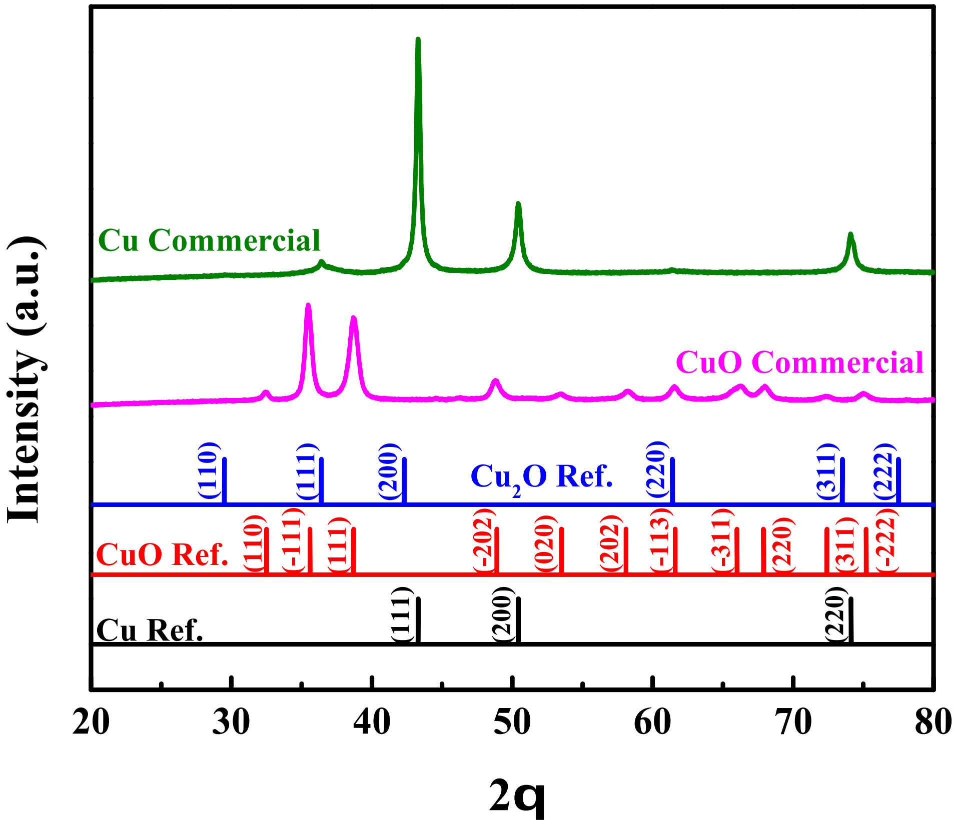

Figure B.7: XRD Plots for Cu and CuO Commercial NPs.

B.6. Computational method: DFT

Table B.4: The final configurations of the CO_2 adsorption over ACN, ADN and SBN molecules are listed. The adsorbate molecule specie, the adsorption site nomenclature and its lateral and frontal view, and the adsorption energy (E_{ads}) are shown from left to right columns, respectively.

Molecule	Adsorption site		E_{ads} (eV)
ACN	N-1	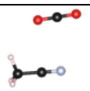 	-0.126
	N-1	 	-0.119
	N-2	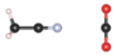 	-0.119
	N-3	 	-0.119
	m-1	 	-0.041
	m-2	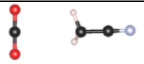 	-0.041
	m-3	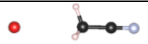 	-0.041
	m-4	 	-0.041
ADN	N-1	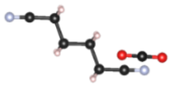 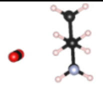	-0.145
	N-2	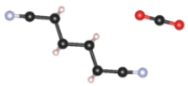 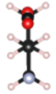	-0.142
	N-3	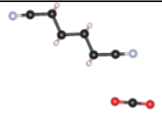 	-0.121
	N-4	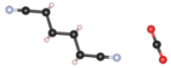 	-0.117
	N-5	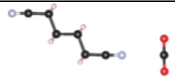 	-0.115
	N-6	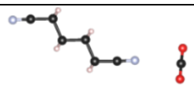 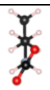	-0.114

	N-7	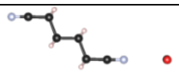 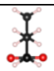	-0.114
	M-1	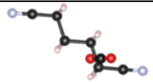 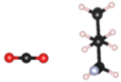	-0.116
	M-2	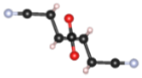 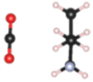	-0.105
	M-3	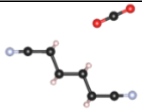 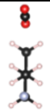	-0.096
SBN	N-1	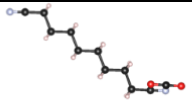 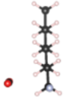	-0.141
	N-2	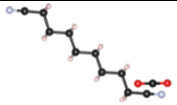 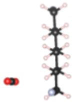	-0.139
	N-3	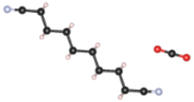 	-0.137
	N-4	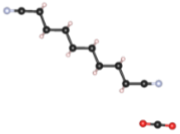 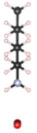	-0.121
	N-5	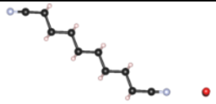 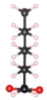	-0.119
	N-6	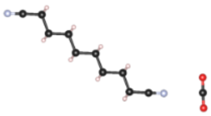 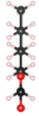	-0.119
	N-7	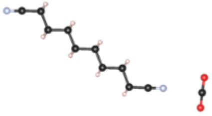 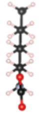	-0.118
	M-1	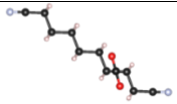 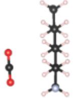	-0.112

	M-2	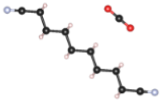 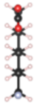	-0.097

Regarding electronic structure the Figure B.8 showed the projected DOS curves for all considered systems before (dashed red line) and after (blue full line) CO_2 adsorption at the most stable site. Only the spin up contribution is plotted because all systems shown symmetric spin up and spin down contribution to the DOS curves. The CO_2-nitrile group interaction is present between the Fermi level and 6 eV, being the most important peaks around 6 eV (see Figure B.8a-c). Also, in all case the CO_2 molecule shown a shifted to the lower energies.

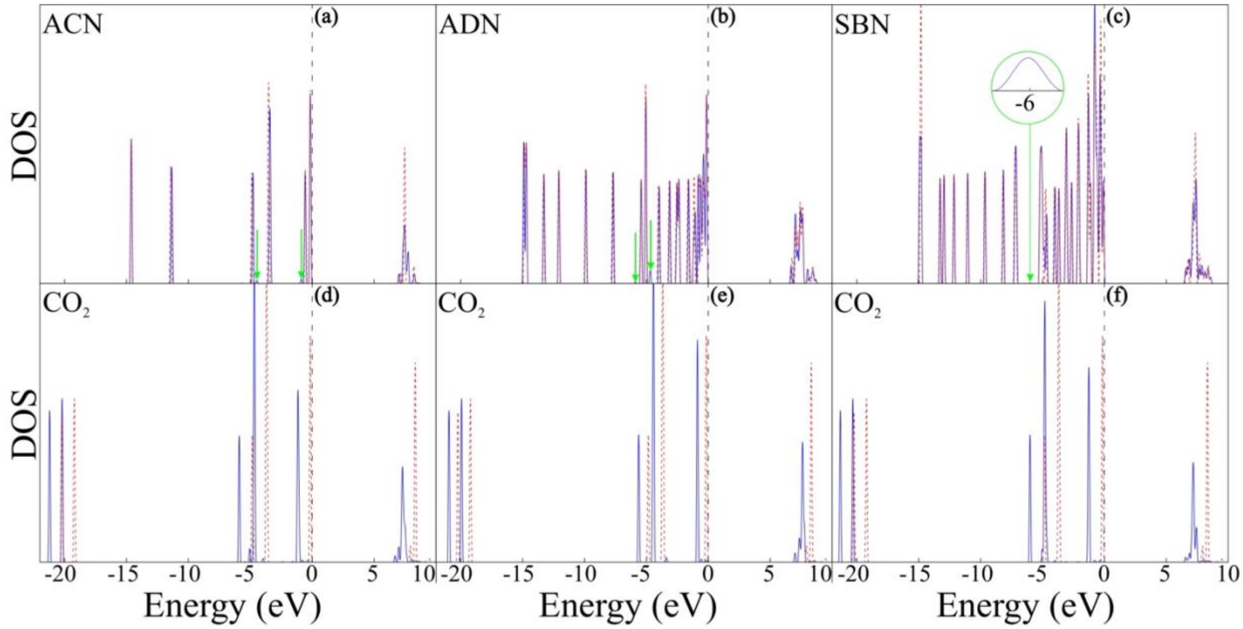

Figure B.8: Projected DOS curves for ACN (a and d); ADN (b and e) and SBN (c and f) before (dashed red line) and after (blue full line) CO_2 adsorption at the most stable site. The green arrow indicates the CO_2-nitrile group interaction peaks. For a better view in the SBN case the interaction is showed magnified in the insert.

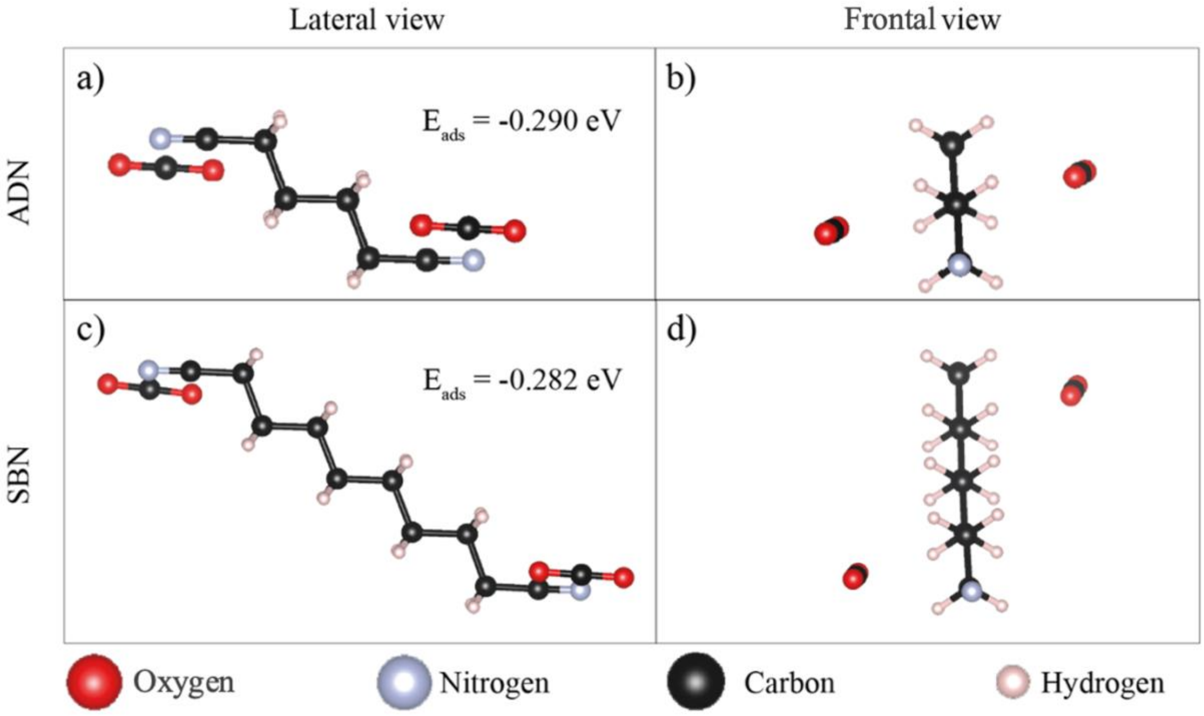

Figure B.9: Lateral (left side) and frontal (right side) views of the final configuration of two CO_2 adsorbed at the opposite N-1 nitrile group sites for ADN and SBN (upper and lower subfigures).

Bader analysis as implemented by Tang *et al.*[12,13] was used to calculate electronic charges on atoms, and the DDEC6 methodology was used to compute the net atomic charges (NACs) and bond order (BO) as described by Manz *et al.*[14-16]. These calculations shown a weak interaction between the CO_2 and the nitrile-based molecules (see Table B.5).

Table B.5: Bond order (BO) for the CO_2-nitrile-based molecules after adsorption at the most stable adsorption site. The atomic labels correspond to those in Figure 3.5 in the main text.

Bond Type	ACN	ADN	SBN
C_1-O_A	0.019	0.017	0.019
N_1-O_A	0.011	0.008	0.009
N_1-C_A	0.021	0.019	0.022
N_1-O_B	0.010	0.010	0.011

B.7. 15min vs 3h CO2 Purge

To ensure that the decrease in activity from acetonitrile to adiponitrile was not a result of a required longer purging time in the electrochemical cell, a 3h CO_2 purge test in adiponitrile was also conducted. Seen in Figure B.10 are both results for the 15 min purge and 3 h purge of CO_2 in adiponitrile for a Cu catalyst. It can be observed that a difference of approximately 0.1 mA cm^{-2} can be observed. As such evidence for a lack of purging was not observed.

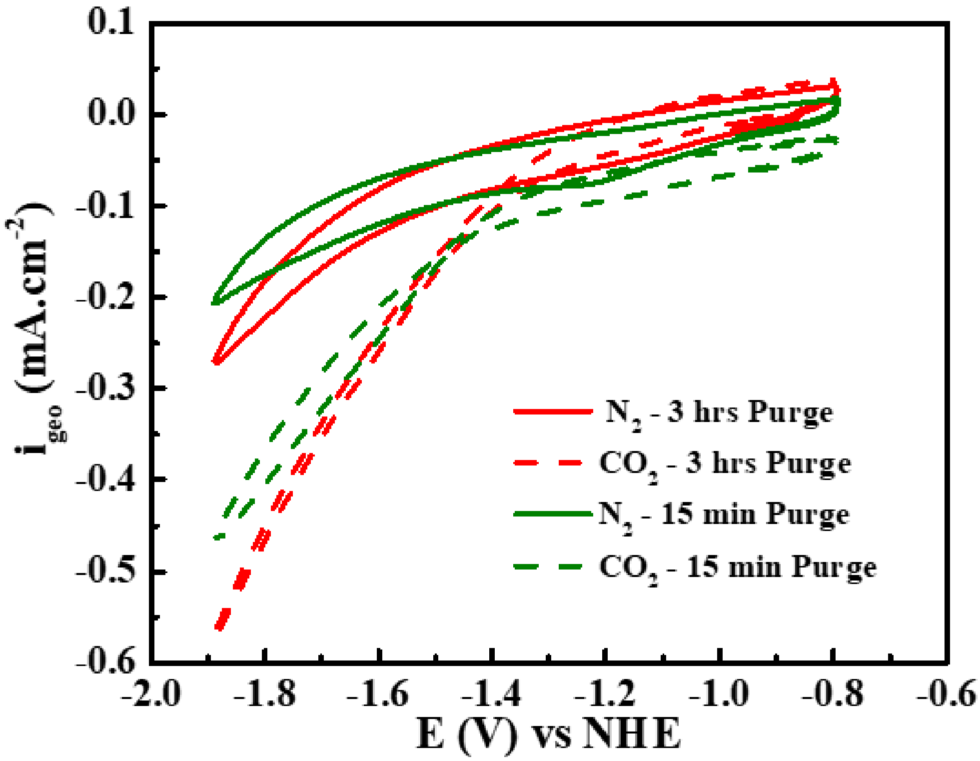

Figure B.10: Cyclic Voltammogram of Cu in 0.1 M TBAPF$_6$ in adiponitrile with 3h CO_2 purge and 15min CO_2 purge at 50 mV.s^{-1} scan rate (fifth stable cycle).

B.8. CA Analysis CV Experiments

Prior to CA measurements, CV under N_2 purge and CO_2 purge were conducted, and post-CA a CO_2 purge CV was also measured. Figure B.11 shows the results of these tests for the acetonitrile, adiponitrile and sebaconitrile electrolytes for both tested catalysts. In line with CA results under acetonitrile, the activity decreased after the CA with CuO commercial catalyst, and increased with the Cu commercial catalyst. In adiponitrile, results were again mirrored with increasing activity for CuO commercial and decreasing with Cu commercial. In sebaconitrile, although CA trends seemed relatively stable, a slight increase was seen in CuO commercial and a decrease with use of Cu commercial.

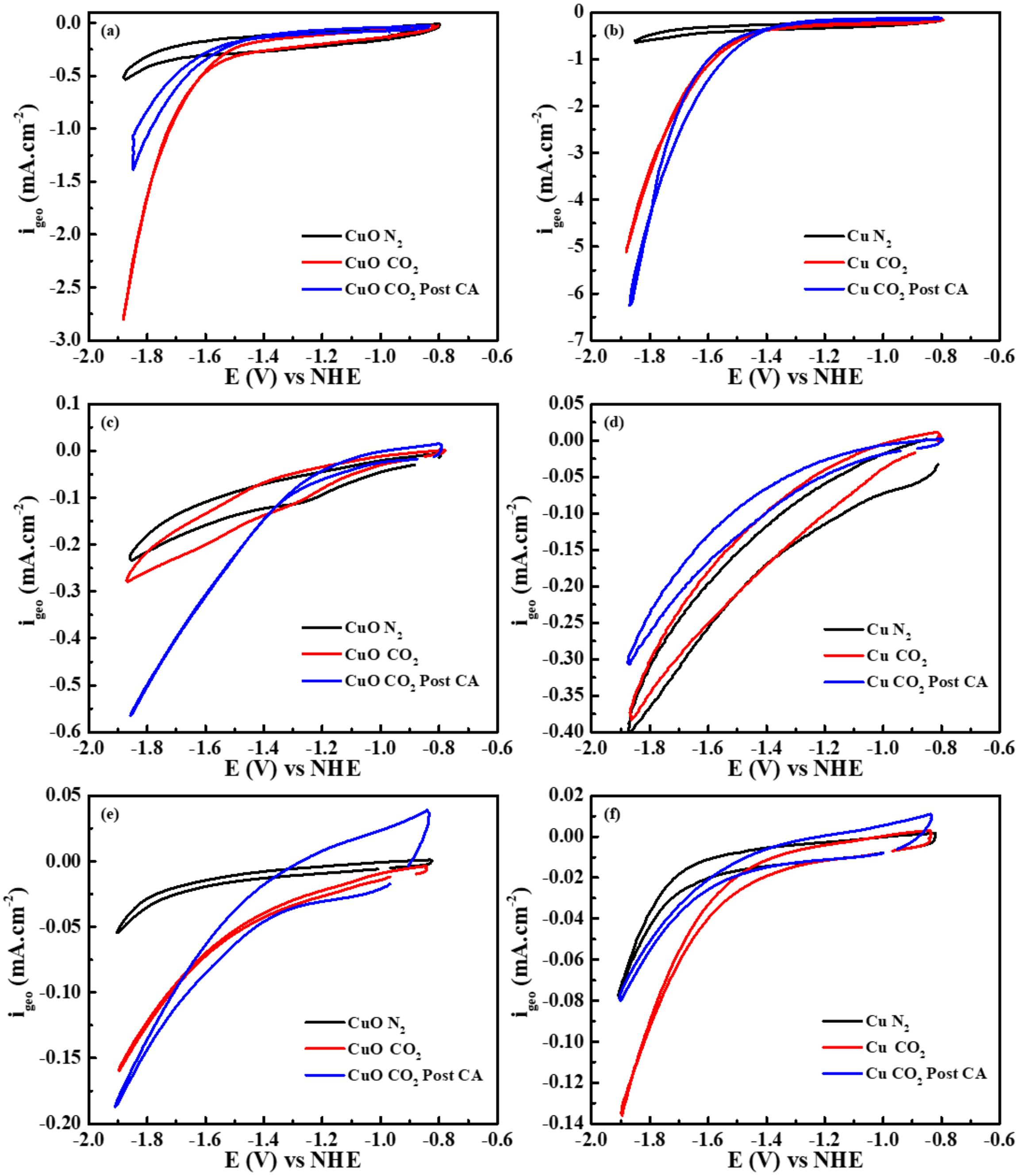

Figure B.11: Cyclic voltammetry taken before and after CA experiments for (a,b) acetonitrile (c,d) adiponitrile and (e,f) sebaconitrile on both commercial CuO and Cu catalyst at 50 mV.s^{-1} scan rate (fifth stable cycle).

References

[1] G. Kresse, J. Hafner, *Phys. Rev. B* **1993**, *47*, 558.

[2] G. Kresse, J. Furthmüller, *Comput. Mater. Sci.* **1996**, *6*, 15.

[3] G. Kresse, D. Joubert, *Phys. Rev. B - Condens. Matter Mater. Phys.* **1999**, *59*, 1758.

[4] J. P. Perdew, K. Burke, M. Ernzerhof, *Phys. Rev. Lett.* **1996**, *77*, 3865.

[5] P. E. Blöchl, *Phys. Rev. B* **1994**, *50*, 17953.

[6] S. Grimme, J. Antony, S. Ehrlich, H. Krieg, *J. Chem. Phys.* **2010**, *132*.

[7] H. J. Monkhorst, J. D. Pack, *Phys. Rev. B* **1976**, *13*, 5188.

[8] V. V. Pavlishchuk, A. W. Addison, *Inorganica Chim. Acta* **2000**, *298*, 97.

[9] M. Moura de Salles Pupo, R. Kortlever, *ChemPhysChem* **2019**, *20*, 2926.

[10] T. Theivansanthi, M. Alagar, *Arch. Phys. Res.* **2010**, *1*, 112.

[11] R. Raghav, P. Aggarwal, S. Srivastava, *AIP Conf. Proc.* **2016**, *020078*.

[12] W. Tang, E. Sanville, G. Henkelman, *J. Phys. Condens. Matter* **2009**, *21*.

[13] R. F. W. Bader, *Atoms in Molecules - A Quantum Theory*, Oxford University Press, **1990**.

[14] T. A. Manz, *RSC Adv.* **2017**, *7*, 45552.

[15] N. G. Limas, T. A. Manz, *RSC Adv.* **2016**, *6*, 45727.

[16] T. A. Manz, N. G. Limas, *RSC Adv.* **2016**, *6*, 47771.

Appendix C. Preliminary ECSA Measurements

Electrochemical surface area (ECSA) measurements of Cu and CuAg bimetallic particles were conducted using a lead (Pb) underpotential deposition (UPD) method[1–4]. First, the catalyst ink on glassy carbon was tested in a cyclic voltammogram (CV) from -0.12 to -0.42 V vs Ag/AgCl at a step size of 10 mV/s in a N_2 purged solution of 0.1 M $HClO_4$ (48-50%, ACS, Alfa Aesar, USA), to obtain the background measurement. Then, a stock solution of 0.1 M $HClO_4$ with $Pb(ClO_4)_2$ (98%, Sigma Aldrich, USA) to introduce a total of 1mM $Pb(ClO_4)_2$ into the total solution was added and the CV under the same conditions was run. The current versus time curve with the background curve subtracted was integrated to obtain the charge consumption from the oxidation of Pb adatoms. The experiment was repeated at a minimum of three times, and the average was used. The Cu ECSA calculations assumed a monolayer of Pb adatoms coverage on the Cu and two electrode Pb oxidation using a conversion factor of 310 μC cm^{-2}[5]. Meanwhile, for the electrochemical coverage of Pb on Ag conversion factor value used was of 400 μC cm^{-2}[2]. The ECSA was then calculated by the equation:

$$\mathrm{A} = {}^{\mathrm{Q_A}}/_{\mathrm{Q_S}} \qquad \text{Equation C-1}$$

where A is the ECSA, Q_A is the obtained charge consumption from the integration and Q_s is the theoretical coverage charge. For the bimetallic particles, the Q_s was estimated as[4]:

$$\mathrm{Q_s} = \mathrm{y_{Cu}Q_{s,Cu}} + \mathrm{y_{Ag}Q_{s,Ag}} \qquad \text{Equation C-2}$$

where y_{Cu} and y_{Ag} are the atomic weight percentage coverage by each metal in the bimetallic particles, and $Q_{s,Ag}$ and $Q_{s,Cu}$ is the theoretical coverage charge for the corresponding metal.

ECSA measurements were conducted for the commercial particles and Cu, Ag and $Cu_{75}Ag_{25}$ syntheses. To represent the way the measurements were observed, Figure C.1a and b are presented for the ECSA measurements for the $Cu_{75}Ag_{25}$ particles. Figure C.1a displays the full cycles, while Figure C.1b displays the integration area of the Pb stripping peak. Notably, only the overall active area of the bimetallic is able to be obtained via the integration, as the peaks are unable to be deconvoluted due to their occurrence over the similar range.

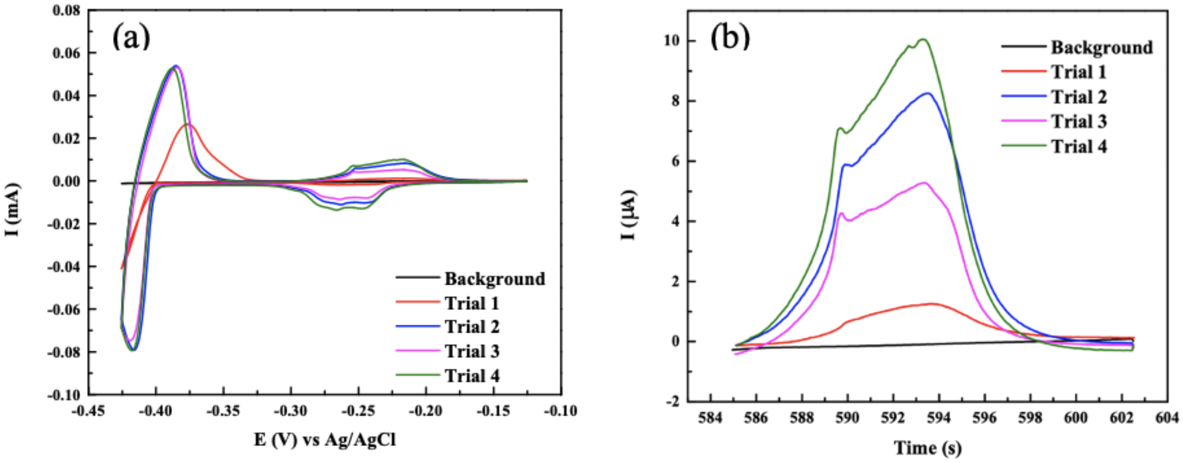

Figure C.1: ECSA results for the $Cu_{75}Ag_{25}$ catalyst displaying (a) CV measurements for the background and 4 trials, as well as (b) the integrated areas of the Pb stripping peaks.

The resulting estimated ECSA values from the average of the integrations for all evaluated catalysts are presented in Table C.1. It was found that the relative active surface areas tended to be smaller for the synthesis particles.

Table C.1: Average ECSAs of the evaluated catalysts along with standard deviations.

Catalyst	ECSA (cm^2)	σ
Cu Synthesis	0.0488	0.023
Cu Commercial	1.6378	0.130
CuO Commercial	0.2830	0.018
Ag Synthesis	0.0097	0.005
Ag Commercial	0.0473	0.045
$Cu_{75}Ag_{25}$ Synthesis	0.1131	0.066
CuAg Commercial Alloy	0.2647	0.139

The results of the electrochemical measurements normalized current densities against ECSA are displayed in Figure C.2a and b for the CV and long-term CAs respectively. The plasmonic responses were unaffected, as the current densities are divided by themselves. However, in the CV results, the Ag activities for both the synthesis and commercial particles increased significantly, as their ECSA was smaller to the other particles. Thus, they show enhanced current densities as their moderate activities are attributed to a smaller surface area. On the other hand, the commercial Cu, CuO and CuAg alloy particles demonstrated a significant reduction in activity performance, as they exhibited relatively larger ECSA. Notably significant evidence of CO_2ER was not observed in the commercial Cu and CuO catalysts. The CA results were similarly affected, comparing the 3h light off/light on results on the synthesized particles, Ag possessed significantly higher current densities to the Cu and $Cu_{75}Ag_{25}$ particles. The results are indicative that Ag may be a superior catalyst for the CO_2ER based on ECSA. However, further corroboration of alternative ECSA measurement approaches are required to support the obtained preliminary results with this methodology.

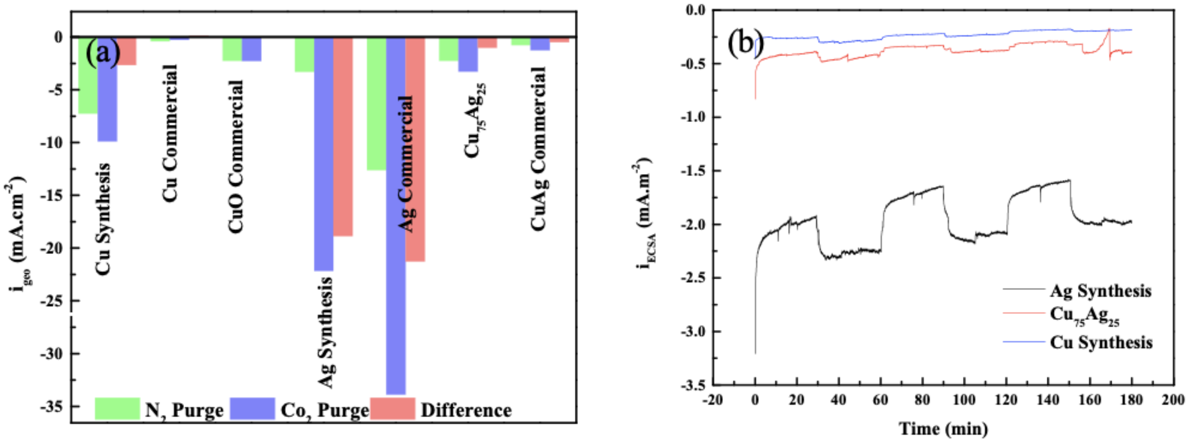

Figure C.2: ECSA normalized (a) maximum current densities at -2.15 vs Hg/HgSO$_4$ summary plot from CVs and (b) 3 hour chopped light CA under constant potential of -1.8 V vs Hg/HgSO$_4$ of the synthesized catalysts.

References

[1] S. D. Giri, A. Sarkar, *Adv. Powder Technol.* **2018**, *29*, 3520.

[2] C.-H. Chen, H.-L. Yang, H.-R. Chen, C.-L. Lee, *J. Electrochem. Soc.* **2012**, *159*, D507.

[3] O. A. Baturina, Q. Lu, M. A. Padilla, L. Xin, W. Li, A. Serov, K. Artyushkova, P. Atanassov, F. Xu, A. Epshteyn, T. Brintlinger, M. Schuette, G. E. Collins, *ACS Catal.* **2014**, *4*, 3682.

[4] N. Mayet, K. Servat, K. B. Kokoh, T. W. Napporn, *Surfaces* **2019**, *2*, 257.

[5] H. Siegenthaler, K. Jüttner, *J. Electroanal. Chem.* **1984**, *163*, 327.